AD-A106 371 AIR FORCE INST OF TECH WRIGHT-PATTERSON AFB OH F/G 4/1
COMPARISON OF THE DYNAMIC PROCESSES DURING MAJOR AND MINOR STRA--ETC(U)
JUN 81 J H DAVENPORT
UNCLASSIFIED AFIT-CI-81-29T NL

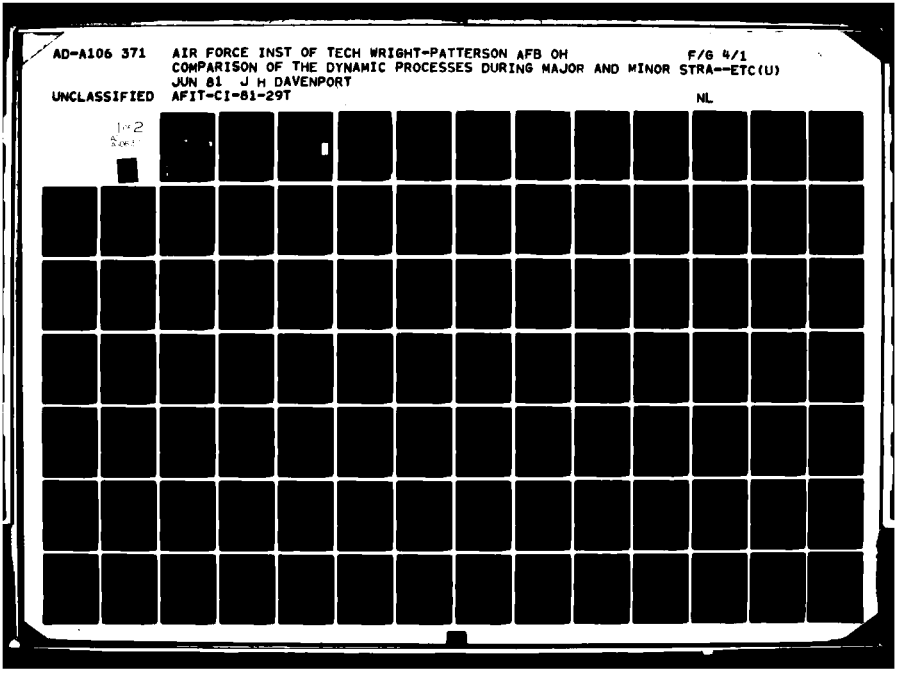

UNCLASS

SECURITY CLASSIFICATION OF THIS PAGE (When Data Entered)

REPORT DOCUMENTATION PAGE

READ INSTRUCTIONS BEFORE COMPLETING FORM

AFIT 291

4 TITLE (and Subtitle) Comparison of the Dynamic Processes During Major and Minor Stratospheric Warmings in A Numerical Model

5 TYPE OF REPORT & PERIOD COVERED
THESIS/DISSERTATION

6 PERFORMING ORG. REPORT NUMBER

7 AUTHOR(s)
James Howard Davenport

8 CONTRACT OR GRANT NUMBER(s)

9 PERFORMING ORGANIZATION NAME AND ADDRESS
AFIT STUDENT AT [illegible]

10 PROGRAM ELEMENT, PROJECT, TASK AREA & WORK UNIT NUMBERS

11 CONTROLLING OFFICE NAME AND ADDRESS
AFIT/NR
WPAFB OH 45433

12 REPORT DATE
[illegible]

13 NUMBER OF PAGES

14 MONITORING AGENCY NAME & ADDRESS (if different from Controlling Office)

15 SECURITY CLASS. (of this report)
UNCLASS

15a DECLASSIFICATION/DOWNGRADING SCHEDULE

16 DISTRIBUTION STATEMENT (of this Report)
APPROVED FOR PUBLIC RELEASE, DISTRIBUTION UNLIMITED

17 DISTRIBUTION STATEMENT (of the abstract entered in Block 20, if different from Report)

18 SUPPLEMENTARY NOTES
APPROVED FOR PUBLIC RELEASE IAW AFR 190-17

[illegible]
Director of Public Affairs
Air Force Institute of Technology (ATC)
Wright-Patterson AFB, OH 45433

29 SEP 1981

19 KEY WORDS (Continue on reverse side if necessary and identify by block number)

20 ABSTRACT (Continue on reverse side if necessary and identify by block number)
ATTACHED

DD FORM 1 JAN 73 1473 EDITION OF 1 NOV 65 IS OBSOLETE UNCLASS

SECURITY CLASSIFICATION OF THIS PAGE (When Data Entered)

LEVEL

DTIC ELECTE OCT 26 1981 S D H

AD A106371

DTIC FILE COPY

AI-29T

AFIT RESEARCH ASSESSMENT

The purpose of this questionnaire is to ascertain the value and contribution of research accomplished by students or faculty of the Air Force Institute of Technology (AFIT). It would be greatly appreciated if you would complete the following questionnaire and return it to:

AFIT/NR
Wright-Patterson AFB OH 45433

RESEARCH TITLE: Comparison of the Dynamic Processes During Major and Minor Statospheric Warmings In A Numerical Model

AUTHOR: James HOward Davenport

RESEARCH ASSESSMENT QUESTIONS:

1. Did this research contribute to a current Air Force project?

a. YES b. NO

2. Do you believe this research topic is significant enough that it would have been researched (or contracted) by your organization or another agency if AFIT had not?

a. YES b. NO

3. The benefits of AFIT research can often be expressed by the equivalent value that your agency achieved by conducting the research. Can you estimate what this research would have cost if it had been accomplished under contract or if it had been done in-house in terms of manpower and dollars?

a. MAN-YEARS

4. Often it is not possible to attach equivalent dollar values to research, although the results of the research may actually be quite important. Whether or not you were able to establish an equivalent value for this research (3, above), what is your estimate of the significance of this AFIT research?

a. Highly Significant b. Significant c. Slightly Significant d. Of No Significance

5. AFIT welcomes any further comments you may have on the above questions, or any additional details concerning the current application, future potential, or other value of this research. Please use the back of this sheet if more room is required for your statements.

NAME GRADE POSITION

ORGANIZATION LOCATION

STATEMENT(S):

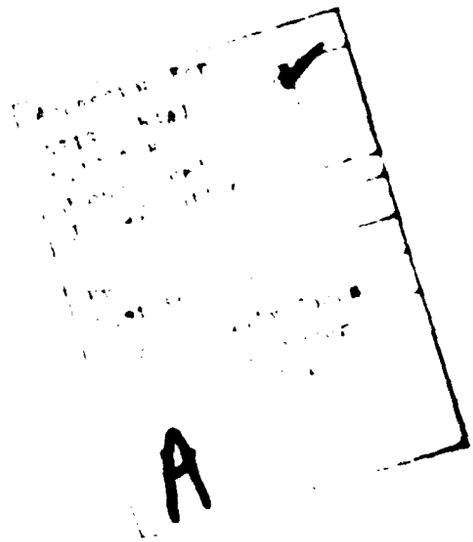

FOLD DOWN ON OUTSIDE - SEAL WITH TAPE

AFIT/ [redacted]
[redacted]

OFFICIAL BUSINESS
PENALTY FOR PRIVATE USE $300

NO POSTAGE
NECESSARY
IF MAILED
IN THE
UNITED STATES

BUSINESS REPLY MAIL
FIRST CLASS PERMIT NO 73236 WASHINGTON D C

POSTAGE WILL BE PAID BY ADDRESSEE

AFIT/ DAA
Wright-Patterson AFB OH 45433

FOLD IN

COMPARISON OF THE DYNAMIC PROCESSES DURING MAJOR AND MINOR STRATOSPHERIC WARMINGS IN A NUMERICAL MODEL

by

James Howard Davenport

An abstract of a thesis submitted to the faculty of
The University of Utah
in partial fulfillment of the requirements for the degree of

Master of Science

S. K. Kao — Chairman, Supervisory Committee

Professor of Meteorology

Department of Meteorology

The University of Utah

June 1981

ABSTRACT

In this study we have analyzed the processes involved in a major and minor warming based on data generated from a 31-layer primitive equation spectral model consisting of a 5-layer troposphere, 12-layer stratosphere and 14-layer mesosphere. The forcing of the model consisted of orographic features designed to simulate the major Northern Hemisphere continents. This gave a combination of wave number 1 and wave number 2 forcing. The analysis of the simulated major and minor warmings indicated several similarities and differences between the cases.

The initial difference between the cases is that case 1 (major warming) had a weak polar vortex, while case 2 (minor warming) had a strong polar vortex. This resulted in case 2 having much larger turbulent flux terms, but not sufficient to reverse the mean polar winds. Case 1 produces a major warming in the polar stratosphere.

Similarities of the cases included: wave number 1 waves dominant in the mesosphere and wave number 2 waves dominant in the stratosphere; development of a meridional circulation of an approximate 8 to 12 day cycle in the stratosphere and mesosphere, and a good correlation between the peaks of this meridional circulation and change in the polar night jet. The peaks of the meridional circulation coincided with magnitude peaks of convergence and/or divergence of momentum and vertical flux of geopotential.

An analysis of the latitude-height sections of meridional flux

of sensible heat and vertical flux of geopotential indicated that the relationship between vertical flux of geopotential and meridional flux of sensible heat, derived from the linearized equations, does not hold for the nonstationary developing stage of the stratospheric warming. This inconsistancy casts questions on the applicability of the concept of the critical level to the state of nonlinear interaction.

COMPARISON OF THE DYNAMIC PROCESSES DURING MAJOR AND MINOR STRATOSPHERIC WARMINGS IN A NUMERICAL MODEL

by

James Howard Davenport

A thesis submitted to the faculty of The
University of Utah in partial fulfillment of the requirements
for the degree of

Master of Science

Department of Meteorology

The University of Utah

June 1981

© 1981 James Howard Davenport

All Rights Reserved

THE UNIVERSITY OF UTAH GRADUATE SCHOOL

SUPERVISORY COMMITTEE APPROVAL

of a thesis submitted by

James Howard Davenport

I have read this thesis and have found it to be of satisfactory quality for a master's degree.

March 27, 1981
Date

S. K. Kao
Chairman, Supervisory Committee

I have read this thesis and have found it to be of satisfactory quality for a master's degree.

March 26, 1981
Date

E. G. Astling
Member, Supervisory Committee

I have read this thesis and have found it to be of satisfactory quality for a master's degree.

MAR 26 1981
Date

D. R. Dickson
Member, Supervisory Committee

7
176

THE UNIVERSITY OF UTAH GRADUATE SCHOOL

FINAL READING APPROVAL

To the Graduate Council of The University of Utah:

I have read the thesis of James Howard Davenport in its final form and have found that (1) its format, citations, and bibliographic style are consistent and acceptable; (2) its illustrative materials including figures, tables, and charts are in place; and (3) the final manuscript is satisfactory to the Supervisory Committee and is ready for submission to the Graduate School.

March 27, 1981
Date

S. K. Kao
Member, Supervisory Committee

Approved for the Major Department

S. K. Kao
Chairman Dean

Approved for the Graduate Council

James L. Clayton
Dean of The Graduate School

04
3-79

ABSTRACT

In this study we have analyzed the processes involved in a major and minor warming based on data generated from a 31-layer primitive equation spectral model consisting of a 5-layer troposphere, 12-layer stratosphere and 14-layer mesosphere. The forcing of the model consisted of orographic features designed to simulate the major Northern Hemisphere continents. This gave a combination of wave number 1 and wave number 2 forcing. The analysis of the simulated major and minor warmings indicated several similarities and differences between the cases.

The initial difference between the cases is that case 1 (major warming) had a weak polar vortex, while case 2 (minor warming) had a strong polar vortex. This resulted in case 2 having much larger turbulent flux terms, but not sufficient to reverse the mean polar winds. Case 1 produces a major warming in the polar stratosphere.

Similarities of the cases included: wave number 1 waves dominant in the mesosphere and wave number 2 waves dominant in the stratosphere; development of a meridional circulation of an approximate 8 to 12 day cycle in the stratosphere and mesosphere, and a good correlation between the peaks of this meridional circulation and change in the polar night jet. The peaks of the meridional circulation coincided with magnitude peaks of convergence and/or divergence of momentum and vertical flux of geopotential.

An analysis of the latitude-height sections of meridional flux

of sensible heat and vertical flux of geopotential indicated that the relationship between vertical flux of geopotential and meridional flux of sensible heat, derived from the linearized equations, does not hold for the nonstationary developing stage of the stratospheric warming. This inconsistancy casts questions on the applicability of the concept of the critical level to the state of nonlinear interaction.

TABLE OF CONTENTS

LIST OF FIGURES

ACKNOWLEDGEMENTS

I wish to convey my deepest appreciation to Dr. Shih-Kung Kao, chairman of my supervisory committee, for his ideas, encouragement, and guidance. His expertise in non-linear interactions and stratospheric warmings was crucial to my endeavors in this study.

I am indebted to Dr. James Koermer for the results of his research, without which this study would not have been possible. Also his willingness to aid in any way possible proved extremely valuable.

I would also like to thank Dr. E. G. Astling and Prof. D. R. Dickson for serving on my supervisory committee. I am grateful to the Air Force Institute of Technology for this educational opportunity, the National Center for Atmospheric Research, which provided the computer facilities for this work, and the National Aeronautics and Space Administration, which supported part of this work under contract No. NAS5-25373.

To my wife, Carol, I wish to express my love for her understanding and support throughout my graduate work

Finally, I give God the glory through whom this was made possible.

CHAPTER 1

INTRODUCTION

Records of winter stratospheric warmings indicate that about half of the warmings are classified as major warmings defined as the occurrence of changing zonal westerly to easterly, the other half are classified as minor warmings (McInturff, 1978). Analyses of major and minor stratospheric warmings show that during major warmings both the temperature and zonal wind reversals occur first in the upper stratosphere then extend downward to the lower stratosphere and troposphere, whereas during minor warmings no reversals of temperature and zonal wind occurs in the stratosphere, and the tropospheric westerly jet remains almost unchanged, indicating little feedback from the stratosphere to the troposphere (Koermer and Kao, 1980). In view of the distinctly different stratosphere-troposphere interactions during the stratospheric major and minor warmings, a numerical simulation of the stratospheric major and minor warmings with the use of 31-level primitive equations spectral model has recently been performed (Koermer, 1980). It is found that results obtained by integrating the numerical model agree well with those of the observed, and that nonlinear interaction plays an important role in the development of stratospheric major and minor warmings. The objectives of this study are to analyze the numerical model by comparing two cases from it. The first case involved a major stratospheric warming. The

second case involved a minor stratospheric warming. By examining these numerical simulations, we hope to gain a better understanding of the dynamic processes involved in the evolution of the stratospheric major and minor warmings. Specifically, we will analyze (1) the effect of vertical flux of geopotential generated from orographic forcing on the development of wave motion and meridional fluxes of zonal momentum and sensible heat in the stratosphere and mesosphere; (2) the development of zonal mean meridional circulation, as the consequence of the convergence of meridional fluxes of zonal momentum and sensible heat; (3) the evolution of the zonal mean maxima of zonal velocity, temperature and variances and covariances of velocity components and temperatures; and (4) the effects of waves of various wave numbers on the development of major and minor stratospheric warmings.

The focus of our comparison is primarily on the zonal mean of u, v, w, T, Φ, deviations from that zonal mean, and cross correlations of these quantities form day 10 to day 40 of each case. Throughout this paper the zonal mean eddy flux quantities will be referred to simply as zonal mean fluxes.

CHAPTER 2

THE PRIMITIVE EQUATION SPECTRAL MODEL

The model used in this study basically consists of two parts. The upper part of the model includes the stratosphere and mesosphere in which a log-pressure coordinate system is used. The lower part of the model represents the troposphere in which a modified sigma coordinate system is used in order to handle orography of the earth.

Figure 1 depicts the vertical grid structure of the coupled models. In the stratosphere and mesosphere, Δz = 3km with 26 prognostic levels, which will generally be represented with the index K. The index r is used to indicate the five prognostic levels of the troposphere where $\Delta\sigma$ = .2. Vertical velocity (w or $\dot{\sigma}$) and geopotential (Φ) are diagnostic variables and values are computed for diagnostic levels centered between the prognostic levels. Vorticity (ζ), divergence (D) and temperature (T) are the prognostic variables common to both models. Additionally, log pressure (q) is a prognostic variable in the troposphere. For boundary conditions, we assume vertical velocity is zero at the top of the upper model and the bottom of the lower model.

The large scale dynamics of an atmosphere are basically governed by the equations of horizontal motions, thermodynamics, mass continuity, and hydrostatic equilibrium. For the tropospheric part of the model, the governing equations in the sigma coordinate

system may be written as follows:

$$\frac{d\vec{V}}{dt} = - f\vec{k} \times \vec{v} - \nabla\phi - \frac{\sigma RT}{\sigma P_* + p_R} \vec{\nabla} P_* + \vec{F} \quad , \tag{1}$$

$$\frac{dT}{dt} = \frac{RT}{c_p (\sigma P_* + p_R)} \dot{p} + \frac{Q}{c_p} \tag{2}$$

$$\frac{\partial P_*}{\partial t} + \nabla \cdot (P_* v) + P_* \frac{\partial \dot{\sigma}}{\partial \sigma} = 0 \quad , \tag{3}$$

$$\frac{\partial \phi}{\partial \sigma} = - \frac{RTP_*}{\sigma P_* + p_R} \quad , \tag{4}$$

where

$$\sigma = (p - p_R)/(p_S - p_R) \quad , \tag{5}$$

p_R is a reference pressure indicating the upper boundary of the tropospheric model and lower boundary of the upper atmospheric model; p_S is the surface pressure; $P_* = p_S - p_R$; $\vec{v}$ is the horizontal velocity; f is the Coriolis parameter; $\vec{k}$ is the vertical unit vector; T is the temperature; $\vec{F}$ is the frictional force; Q is the diabatic heating; c_p is the specific heat of dry air at constant pressure; $\dot{p} = dp/dt$ is the vertical velocity in pressure coordinates; $\dot{\sigma} = d\sigma/dt$ is the vertical velocity in σ-coordinates; t represents time; and ∇ is the horizontal gradient operator.

For the upper atmosphere, the governing equations in the log-pressure coordinate system may be written as follows:

$$\frac{d\vec{v}}{dt} = - f\vec{k} \times \vec{v} - \nabla\phi + \vec{F} , \tag{6}$$

$$\frac{dT}{dt} = \frac{Q}{c_p} - \frac{N^2 wH}{R} , \tag{7}$$

$$\nabla \cdot V + \frac{\partial w}{\partial z} - \frac{w}{H} = 0 , \tag{8}$$

$$\frac{\partial \phi}{\partial z} = \frac{RT}{H} , \frac{d\phi_o}{dz} = \frac{RT_o}{H} \tag{9}$$

where

$$\frac{d}{dt} = \frac{\partial}{\partial t} + v \cdot \nabla + w \frac{\partial}{\partial z} ,$$

$$z = - H \ell n \, (p/p_s) ,$$

$$w = \frac{dz}{dt} ,$$

$$H = RT_s/g , \tag{10}$$

$$N^2 \equiv \frac{R}{H} \left(\frac{dT_o}{dz} + \frac{\kappa T_o}{H}\right)$$

$$\kappa \equiv R/c_p$$

By the Hemholtz theorem $\vec{v}$ can be expressed as the sum of non-divergent and irrotational parts as follows

$$\vec{v} = \vec{k} \times \nabla\psi + \nabla\chi , \tag{11}$$

where ψ is the stream function and χ is the velocity potential. Hence, it follows that

$$\zeta = \vec{k} \cdot \nabla \times \vec{v} = \nabla^2 \psi \,, \tag{12}$$

$$D = \nabla \cdot \vec{v} = \nabla^2 \chi \,, \tag{13}$$

where D is the horizontal divergence. In spherical coordinates, we can express (11) in component form

$$u = -\frac{1}{a}\frac{\partial \psi}{\partial \phi} + \frac{1}{a \cos \phi}\frac{\partial \chi}{\partial \lambda} \,, \tag{14}$$

$$v = \frac{1}{a \cos \phi}\frac{\partial \psi}{\partial \lambda} + \frac{1}{a}\frac{\partial \chi}{\partial \phi} \,, \tag{15}$$

where u is the zonal velocity component; v is the meridional velocity component, a is the earth's radius; ϕ is the latitude; and λ is the logitude. If we further define

$$U \equiv u \cos \phi \,, \tag{16}$$

$$V \equiv v \cos \phi \,, \tag{17}$$

it follows from (14) and (15) that

$$U = -\frac{\cos \phi}{a}\frac{\partial \psi}{\partial \phi} + \frac{1}{a}\frac{\partial \chi}{\partial \lambda} \,, \tag{18}$$

$$V = \frac{1}{a}\frac{\partial \psi}{\partial \lambda} + \frac{\cos \phi}{a}\frac{\partial \chi}{\partial \phi} \,, \tag{19}$$

We can also express the frictional force $\vec{F}$ in component form as

$$\vec{F} = F_\lambda \vec{i} + F_\phi \vec{j} \tag{20}$$

where F_λ and F_ϕ are the longitudinal and meridional components, respectively. The parameterization of these components will be detailed later in this chapter.

In order to control spectral blocking (Puri and Bourke, 1974) that results from horizontal truncation, diffusion is applied to the vorticity equation. This technique dampens deviations from equilibrium fields but not the equilibrium fields. With this specification added and using (12), (14) to (20), we can express the vorticity equation for the troposphere as follows:

$$\frac{\partial \nabla^2 \psi}{\partial t} = - \frac{1}{a^2 \cos^2 \phi} \left[\frac{\partial A}{\partial \lambda} + \cos \phi \frac{\partial B}{\partial \phi} \right] + K_h \left[\nabla^2 (\zeta - \zeta_e) + \frac{2(\zeta - \zeta_e)}{a^2} \right] \qquad (21)$$

where we define

$$A \equiv (\zeta + f)u + \dot{\sigma}(\partial v/\partial \sigma) + (RT'/a)\cos \phi (\partial q/\partial \phi) - F_\phi \cos \phi \qquad (22)$$

$$B \equiv (\zeta + f)v - \dot{\sigma}(\partial u/\partial \sigma) - (RT'/a)(\partial q/\partial \lambda) + F_\lambda \cos \phi \qquad (23)$$

where

$$q \equiv \ln(\sigma P_S + P_R) .$$

K_h is the horizontal diffusion coefficient. The e subscript represents equilibrium vorticity at the start of model integrations.

For the upper atmosphere, the parallel vorticity equation may be expressed as follows:

$$\frac{\partial \nabla^2 \psi}{\partial t} = - \frac{1}{a^2 \cos^2 \phi} \left[\frac{\partial \hat{A}}{\partial \lambda} + \cos \phi \frac{\partial \hat{B}}{\partial \phi} \right] + K_h \left[\nabla^2 (\zeta - \zeta_e) + \frac{2(\zeta - \zeta_e)}{a^2} \right] \qquad (24)$$

where

$$\hat{A} = (\zeta + f)U + w(\partial v/\partial z) - F_{\phi} \cos\phi \ , \tag{25}$$

$$\hat{B} = (\zeta + f)V - w(\partial u/\partial z) + F_{\lambda} \cos\phi \ , \tag{26}$$

for $w = dz\ dt$.

Combining (21) and (24) into a single expression, we can write

$$\partial\zeta/\partial t = Z + K_h[\nabla^2(\zeta-\zeta_e) + 2(\zeta-\zeta_e)/a^2] \tag{27}$$

where Z takes on the values of the non-diffusive terms on the right hand side of (21) for the troposphere and the right hand side of (24) for the stratosphere and mesosphere.

It can be shown by taking horizontal divergence of (1) that the divergence tendency equation takes the following form:

$$\frac{\partial(\nabla\cdot\hat{V})}{\partial t} = \nabla\cdot[-(\zeta+f)\hat{k}\times\hat{v}] - \nabla^2\left(\phi + \frac{\hat{v}\cdot\hat{v}}{2} + \frac{\bar{RT}}{q}\right)$$

$$- \nabla\cdot[RT'\nabla q + \dot{\sigma}(\partial\hat{v}/\partial\sigma) - \hat{F}] \ . \tag{28}$$

Expanding (28) in spherical coordinates, introducing horizontal diffusion, and grouping terms as with the vorticity equation, we obtain

$$\frac{\partial\nabla^2\chi}{\partial t} = \frac{1}{a^2\cos^2\phi}\left[\frac{\partial\hat{B}}{\partial\lambda} - \cos\phi\,\frac{\partial\hat{A}}{\partial\phi}\right] - \nabla^2(E + \phi + \bar{RT}q)$$

$$+ K_h[\nabla^2 D + 2(D/a^2)] \tag{29}$$

where

$$E \equiv \frac{v\cdot v}{2} = \frac{u^2 + v^2}{2\cos^2\phi} \tag{30}$$

For the upper portion of the model, we have

$$\frac{\partial \nabla \chi}{\partial t} = \frac{1}{a \cos^2 \phi} \left[\frac{\partial \hat{B}}{\partial \lambda} - \cos\phi \frac{\partial \hat{A}}{\partial \phi} \right] - \nabla^2 (E + \phi)$$

$$+ K_h [\nabla^2 D + 2(D/a^2)] \, . \qquad (31)$$

As a single combined equation, we can write the divergence tendency equation as

$$\partial D/\partial t = P - \nabla^2 (\phi + cR\bar{T}q) + k_h [\nabla^2 D + 2(D/a^2)] \, , \qquad (32)$$

where $c = 0$ for the upper portion of the model and $c = 1$ for the troposphere and where P takes on the remaining values on the right of (29) that are not explicitly shown in (32) and on the right of (31) in a similar fashion for the lower and upper portions of the model respectively.

Expanding the thermodynamic equation (2) and expressing temperature in terms of a layer mean and deviation allow us to write

$$\frac{\partial T'}{\partial t} = -\frac{1}{a\cos^2\phi}\left[\frac{\partial UT'}{\partial\lambda} + \cos\phi\,\frac{\partial VT'}{\partial\phi}\right] + DT' + \alpha(z)(T'_e - T')$$

$$+ K_h[\nabla^2(T'-T'_e)] + {}_vF_T - \dot{\sigma}(\partial T'/\partial\sigma)$$

$$- (\partial\bar{T}/\partial\sigma)\left[\frac{\sigma}{p_*}\int_0^1 (\hat{V}\cdot\hat{\nabla}p_*)d\sigma - \frac{1}{p_*}\int_0^\sigma (\hat{V}\cdot\hat{\nabla}p_*)d\sigma + \delta'(\sigma-1)\frac{{}^wR^pR}{H}\right]$$

$$- \frac{RT'}{c_p(\sigma p_* + p_R)}\left[\int_0^\sigma (p_* D + \hat{V}\cdot\hat{\nabla}p_*)d\sigma - \sigma\hat{V}\cdot\hat{\nabla}p_* + \frac{{}^wR^pR}{H}\right]$$

$$- \frac{R\bar{T}}{c_p(\sigma p_* + p_R)}\left[\int_0^\sigma (\hat{V}\cdot\hat{\nabla}p_*)d\sigma - \sigma\hat{V}\cdot\hat{\nabla}p_* + p_*\delta'\frac{{}^wR^pR}{H}\right]$$

$$- \frac{R\bar{T}}{c_p}\beta'\left[\int_0^\sigma D d\sigma + \bar{\delta}\frac{{}^wR^pR}{H}\right]$$

$$- (\partial\bar{T}/\partial\sigma)\left[\sigma\int_0^1 D d\sigma - \int_0^\sigma D d\sigma + \bar{\delta}(\sigma-1)\frac{p_R}{H}\exp(\frac{z_R}{H})\int_{z_R}^{z_{TOP}} D\exp(\frac{-z}{H})dz\right]$$

$$- \frac{R\bar{T}}{c_p}\bar{\beta}\left[\int_0^\sigma D d\sigma + \bar{\delta}\frac{p_R}{H}\exp(\frac{z_R}{H})\int_{z_R}^{z_{TOP}} D\exp(\frac{-z}{H})dz\right], \qquad (33)$$

and the thermodynamic equation for the upper atmosphere

$$\frac{\partial T'}{\partial t} = \frac{-1}{a\cos^2\phi}\left[\frac{\partial(UT')}{\partial\lambda} + \cos\phi\,\frac{\partial(VT')}{\partial\phi}\right] + DT' - w\frac{\partial T'}{\partial z}$$

$$+ K_h[\nabla^2(T'-T'_e)] - \frac{RT'w}{c_pH} + \alpha(T'_e - T') - \frac{HN^2}{R}\exp(\frac{z}{H})\int_z^{z_{TOP}} D\exp(\frac{-z}{H})dz, \qquad (34)$$

where $\alpha(z)$ is the Newtonian heating-cooling coefficient given by Holton (1976), ${}_{v}F_{T}$ denotes the vertical diffusion term, $\delta \equiv \overline{\delta} + \delta' = (1/P_*)$, $\beta \equiv \overline{\beta}(\sigma) + \overline{\beta}' = P_*/(\sigma P_* + p_R)$, the overbar indicates the horizontal domain average, c_p is the specific heat of dry air at constant pressure, and N^2 is the buoyancy frequency assumed to be constant throughout the stratosphere and mesosphere. The term $RT'w/c_pH)$ in (34) was neglected in the formulation of Lordi et al. (1980).

The surface pressure tendency is determined from the tropospheric continuity equation in the form

$$\frac{\partial q}{\partial t} = \frac{-\sigma}{\sigma P_* + p_R}\left[\int_0^1 (\vec{V}\cdot\nabla P_*)d\sigma + P_*\delta'\frac{w_R p_R}{H}\right]$$

$$- \sigma\beta'\left[\int_0^1 D d\sigma + \overline{\delta}\frac{w_R p_R}{H}\right]$$

$$- \sigma\overline{\beta}\left[\int_0^1 D d\sigma + \overline{\delta}\frac{p_R}{H}\exp\left(\frac{z_R}{H}\right)\int_{z_R}^{z_T} D\exp\left(\frac{-z}{H}\right)dz\right] . \quad (35)$$

where $q = \ln(\sigma P_* + p_R)$. In Eqs. (33) - (35), we have isolated divergence with layer mean terms, indicated by the overbar, and time varying terms, indicated by the prime, so that we will be able to use semi-implicit time differencing.

The hydrostatic equation can be written in terms of layer mean quantities and deviations from layer means. For the troposphere, we have

$$\partial\overline{\phi}/\partial q = -R\overline{T}, \quad (36)$$

$$\partial\phi'/\partial q = - RT' \ . \tag{37}$$

For the upper atmosphere in terms of deviations from the layer means, we can write

$$\partial\phi'/\partial z = RT'/H \ . \tag{38}$$

For the upper part of the model, the frictional components F_λ and F_ϕ are represented by the Rayleigh friction parameterization. In the tropospheric part of the model, vertical diffusion is also parameterized in these components along with Rayleigh friction.

Following the vertical formulations of Bourke et al. (1977), we can express the tropospheric components of $\vec{F}$ as follows:

$$F_\lambda = \left(\frac{g}{p_*}\right) \frac{\partial \tau_\lambda}{\partial \sigma} - F_r(u - u_e) \ , \tag{39}$$

$$F_\phi = \left(\frac{g}{p_*}\right) \frac{\partial \tau_\phi}{\partial \sigma} - F_r v \ , \tag{40}$$

where F_r is the Rayleigh friction coefficient, u_e is the initial equilibrium zonal wind components; and

$$\tau_\lambda = \rho^2 \left(\frac{g}{p_*}\right) K_v \frac{\partial u}{\partial \sigma} \ , \tag{41}$$

$$\tau_\phi = \rho^2 \left(\frac{g}{p_*}\right) K_v \frac{\partial v}{\partial \sigma} \ , \tag{42}$$

for density ρ and vertical diffusion coefficient K_v defined as

$$K_v = \rho \left(\frac{g}{p_*}\right) v^2 \left|\frac{\partial \vec{V}}{\partial \sigma}\right| \tag{43}$$

where ν is the mixing length which we assume has a value of 30 meters for $\sigma \geq .1$ and is zero for $\sigma < .1$.

The lower boundary specification is given by

$$\tau_{*\lambda} = - \rho_N C_d |\hat{v}_N| u_N \tag{44}$$

$$\tau_{*\phi} = - \rho_N C_d |\hat{u}_N| v_N , \tag{45}$$

where the N subscript denote the lowest prognostic level. C_d is the drag coefficient assumed to be .0025.

Except for vertical derivatives and the computation of non-linear terms, which are formed at grid points, other model computations are handled spectrally. The variables ψ, χ, ϕ', u, v, P_*, T' and q can be expanded in terms of spherical harmonics as follows:

$$\{\psi, \chi, \phi'\} = a^2 \sum_{m=-J}^{+J} \sum_{\ell=|m|}^{|m|+L} \{\psi_\ell^m, \chi_\ell^m, \phi_\ell^m\} Y_\ell^m ; \tag{46}$$

$$\{U, V\} = a \sum_{m=-J}^{+J} \sum_{\ell=|m|}^{|m|+L+1} \{U_\ell^m, V_\ell^m\} Y_\ell^m ; \tag{47}$$

$$\{P_*\} = a \sum_{m=-J}^{+J} \sum_{\ell=|m|}^{|m|+L} \{P_{*\ell}^m\} Y_\ell^m ; \tag{48}$$

$$\{T', q\} = \sum_{m=-J}^{+J} \sum_{\ell=|m|}^{|m|+L} \{T_\ell^m, q_\ell^m\} Y_\ell^m , \tag{49}$$

where

$$Y_{\ell}^{m} = P_{\ell}^{m}(\mu)e^{im\lambda} , \tag{50}$$

$$\mu = \sin \phi . \tag{51}$$

$P_{\ell}^{m}(\mu)$ is an associated Legendre polynomial normalized to unity with m, the longitudinal wavenumber, and ℓ, the latitudinal index. L determines the limit of the parallelogramic truncation. The {} terms on the right of (46) - (49) represent the respective spherical harmonic coefficients. J is the longitudinal wavenumber truncation.

After the vertical derivatives and non-linear products have been formed at grid points, the resulting terms can be transformed in terms of Fourier series as follows:

$$\{Z,\ D,\ T,\ P,\ \gamma'[\theta],\ \Gamma[T']\} = \sum_{m=-J}^{+J} \{Z_m,\ D_m,\ T_m,\ P_m,\ \theta_m,\ \kappa_m\}e^{im\lambda} \tag{52}$$

where the m subscript represents the respective Fourier coefficient. The Legendre transform defined by

$$(\ )_{\ell}^{m} = \int_{-\pi/2}^{\pi/2} (\ )_m P_{\ell}^{m}(\mu)\cos\phi \, d\phi \tag{53}$$

can be applied to the Fourier coefficients in (52) to obtain the appropriate spherical harmonic coefficients. Since in the model, the Fourier series defined by (53) are formed at Gaussian latitudes, (53) can be computed exactly for each term up to the point of truncation.

Initial fields of geopotential, temperature, stream function and

log-pressure must be specified before the start of model integrations. For these initial conditions, we specify zonal profiles that are non-divergent and essentially have a non-divergent tendency. These latter conditions are essential so that high frequency oscillations, which could adversely affect the model's behavior, are basically eliminated.

To arrive at a balanced state in the troposphere, we initially started with constant pressure level zonal temperature deviations from level means, based on January climatic tables from Oort and Rasmusson (1972). Data for polar latitudes were extrapolated from January 1974 and 1976 data from the National Meteorological Center (NMC) observational grids. The above temperature fields, which were specified at 5° latitude increments, were first linearly interpolated to Gaussian latitudes used in the model.

Averaging the diagnostic level geopotentials to obtain prognostic level values as is done in the model and using the corresponding temperature and pressure fields, we can then quadratically solve the gradient wind balance equation for our σ-coordinate system

$$u\left(f + \frac{u \tan\phi}{a}\right) = -\frac{1}{a}\frac{\partial \phi'}{\partial \phi} - \frac{\sigma R(\bar{T} + T')}{\sigma P_* + P_R}\frac{1}{a}\frac{\partial P_*}{\partial \phi} \qquad (54)$$

for the zonal velocity field u. The mean temperature profile $\bar{T}$ is assumed to be that of the standard atmosphere at 45° N.

The orographic forcing in the model is very idealistic and simplistic. The topographic pattern was placed in such a manner as to simulate the continental land mass distribution of the Northern

Hemisphere (Bourke). The longitudinal distribution of the surface height, z_*, at 45N can be expressed empirically as follows:

$$z_*(45N) = A_1 \sin(m_1\lambda) + A_2 \sin(m_2\lambda - \frac{\pi}{2}) + \bar{z}_* , \tag{55}$$

where A_1 and A_2 are the amplitudes of zonal wave numbers $m_1 = 1$ and $m_2 = 2$, respectively; $\bar{z}_*$ is the initial flat surface height and was used to determine the initial mean surface pressure $\bar{p}_s$ based on standard atmosphere profiles. The latitudinal variation can be expressed by

$$z_*(\phi) = z_*(45N) \sin^2(2\phi) . \tag{56}$$

The model which generated the data base for this thesis had a $\bar{z}_* = A_2 = 240$ m and $A_1 = 150$ m. The maximum z_* for the simplistic European/Asian land mass is 630 m ($A_1 + A_2 + \bar{z}_*$) and for the North American continent, z_* was 330 m ($A_2 - A_1 + \bar{z}_*$).

To prevent the model from being shocked by the sudden introduction of topography, it was slowly turned on according to the following algorithm:

$$\phi_*' = g(z_* - \bar{z}_*)[1 - \exp(-t/t_o)] , \tag{57}$$

for time t where $t_o = 2.5 \times 10^5$ s. With this formulation, ϕ_*' attains about 90% of its maximum value after 7 days.

We have tested the spectral model and integrated for forty days to obtain stable solution. Preliminary reports obtained from the numerical simulation with the use of this model compare favorably with the observations.

CHAPTER 3

ANALYSIS OF THE BEGINNING FORCES ON THE DEVELOPMENT OF THE STRATOSPHERIC WARMING

The 31 layer model was initialized with mean zonal winds as depicted in Fig. 2a for case 1 (C1) and Fig. 2b for case 2 (C2), and with orographic forcing as shown in Fig. 3. For nearly all quantities computed in the analysis of this model, C2 will have magnitudes two to six times as large as C1. Since the winter climatology is adjusted to give a non-divergent flow and essentially a non-divergent tendency, there are no perturbations developing until the orographic features are introduced. This means that the initial perturbations of the model will be those caused by the orography and thus $\overline{W'\Phi'}$ is the initial perturbations of the model. The induced orography (Fig. 3) is fairly simple with its maximum height at 45°N. Yet, the maximum flux of $\overline{W'\Phi'}$ after day 6 occurs near 70°N.

In referencing various levels of the atmosphere, we will use approximately 13.5 Km as the tropopause, 47 Km as the stratopause and 85 Km as the mesopause. These values are based on the vertical temperature profile for the U.S. Standard Atmosphere (1976). For C1 we selected day 18 and day 30 as representative charts of the zonal mean latitude-height distributions. Day 18 represents the general configuration of the quantities before the wind reversal (major warming) and day 30 the configuration after the warming. These days

are also the period of wave transition in the lower levels of the model. For C2 we selected day 26 and day 30. Day 26 is representative of conditions prior to and during the first warming period, while day 30 represents some of the significant changes that occur during the last stages and just after a warming period. We will also comment on day 34 of C2 since it seems to reflect a transitory condition between warming surges.

3.1 Effect of the Surface Forcing Function on the Development of Waves

By day 2, after the introduction of the forcing function, there is an accumulation of horizontal, as well as vertical velocity variances at the top of the model. However, by day 6 the variance has shifted from the top of the model to the stratosphere. After this shift of variance, it appears that most of the development occurs in the region of the stratosphere. By looking at the zonal mean vertical propagation of geopotential $\overline{W'\Phi'}$ and the velocity variances that it induces, we try to develop a better understanding of the mechanisms involved that bring about the rapid stratospheric warmings.

On day 18 of C1, there is a maximum of $\overline{W'\Phi'}$ at about 76°N and 50 Km (Fig. 4a). By day 30, we note the flux of geopotential has dropped to about one third the magnitude of day 18 and moved slightly south indicating a more quasi-stationary state. On day 26 of C2 a similar location of $\overline{W'\Phi'}$ to C1's day 19 (Fig. 4c). However, by day 30 of C2, a cell of sinking geopotential has developed in the area for formally rising geopotential on day 26 (Fig. 4d), but by day 34 the

model has returned to a near pre-warming configuration. The difference of magnitudes from day 18 to day 30 in C1 and from 26 to day 30 of C2 indicates that the vertical energy propagation has been reduced. Since our forcing function is constant, this implies that there has been a dynamic change in the environment. The contrast, however, in the difference of relative magnitudes on day 30 to day 18 of C1 and day 34 to day 26 of C2 is our first indication of a major difference in the development of the two cases. It seems that C2 and C1 are undergoing slightly different atmospheric changes. These differences of dynamic effects seem to be primarily in the area of wave to wave and wave to mean interactions. In an effort to discern these critical differences a limited spectral analysis of the two cases was accomplished. The results of this analysis is discussed in Chapter 6.

The consequences of the vertical flux of geopotential can be seen most readily in terms of variance. As noted earlier, the concentration of the variance of the velocities began at the top of the model, then shifted to the stratosphere, primarily in the polar regions, by day 6 in both C1 and C2.

It should be noted, however, that $\overline{u'^2}$ had two additional maximums, besides the one in the polar stratosphere. One of these was at mid-latitude in the stratosphere and the second at 25°N at the tropopause. This last variance of u is the dominant maximum maximum by nearly twice the stratospheric quantities. The vertical velocity, w, had an area of significant variance located at the tropopause and about 35°N. C2 is very similar to C1 during the first ten days of development except some of its maxima of variances are shifted northward about 5

degrees.

As the model progresses with time, we can see from Fig. 5 and Fig. 7 that the variances are concentrated at the stratopause. By comparing Fig. 5 and Fig. 6, it is fairly easy to see that the maximum variance of $\bar{u}$ occurs in the areas of maximum gradient of $\bar{u}$. Thus for C1 there are two maximums of variance on day 18 (Fig. 6a) with the northern maximum diminisning by day 30 as the polar night jet (PNJ) decreases in velocity and reverses. In C2, however, we note that the symmetry of variance magnitudes (Fig. 5c) on day 26 shifts to a dominant cell at the polar region by day 30 even though the PNJ has diminished. This could be due to the model cycling back into a single core jet by day 34.

Relating the variance of $\bar{u}$ to that of $\bar{v}$, the meridional velocity, there are three features which stand out. First, there tends to be only one area of maximum of $\overline{v'^2}$ as opposed to $\overline{u'^2}$ having two. The second is that $\overline{v'^2}$ is between the areas of maximum $\overline{u'^2}$ and the third item worth noting is that $\overline{u'^2}$ and $\overline{v'^2}$ have a very large maximum on day 30 in C2, whereas, in C1 $\overline{u'^2}$ peaks on day 30, but $\overline{v'^2}$ is decreasing on day 30.

3.2 Comparing the Vertical Flux of Geopotential to the Meridional Flux of Zonal Momentum and the Variance of the Zonal and Meridional Velocity

Looking back at day 18 and day 30 for C1, it appears that the maximum component of vertical flux of geopotential occurs at approximately the same height, 40 Km, as the maximum of the meridional

flux of turbulent momentum ($\overline{u'v'}$). This is not too surprising since this is also the approximate height of the variance maxima of $\bar{u}$ and $\bar{v}$. Comparing Fig. 8 to Figs. 5 and 7, we also note that the maximum of $\overline{u'v'}$ is between the maximum centers of $\overline{u'^2}$ and $\overline{v'^2}$ except on day 30 of C2 where the maximum of $\overline{u'^2}$ and $\overline{v'^2}$ are both near 90°N.

The area of maximum $\overline{u'v'}$ in C1 is centered at 55°N on day 18 and 45°N by day 30.

C2 is very similar on day 26 to day 18 of C1, but day 30 of C2 is quite different. The area of strong $\overline{u'v'}$ convergence on day 26 has been replaced with a much weaker area of convergence and an area of divergence has developed at 72°N and 43 Km. This seems to be a transient phenomenon which disappears by day 34. Many of these momentum transport changes in C1 and C2 seem to be related to phase changes of the spectral components. These changes will therefore be discussed in more detail in the chapter on spectral analysis.

3.3 Relationship of the Vertical Flux of Geopotential to the Meridional Flux of Sensible Heat

The linearized relationship [Eq. (58)] developed by Charney and Drazin (1961) and Eliasen and Palm (1961) relates vertical transport of geopotential to meridional transport of sensible heat and can be viewed as Eq. (59).

$$\overline{\dot{z}\psi} = \frac{f_o}{\Gamma} (U-C) \overline{\frac{\partial \psi}{\partial x} \frac{\partial \psi}{\partial z}} \tag{58}$$

$$\overline{w'\phi'} \propto \overline{v'T'} (U-C) \ . \tag{59}$$

This relation indicates that the larger the amplitude of $\overline{w'\Phi'}$ the larger the amplitude of $\overline{v'T'}$. However, as we compare this linearized equation to the spectral model diagrams, we find only a degree coincidence. For example, day 18 of C1 (Fig. 9a) shows that $\overline{v'T'}_{max}$ is south of $\overline{w'\Phi'}_{max}$ (Fig. 4a). This is also the case on day 26 of C2.

By the end of the warming period, the meridional transport of sensible heat and vertical transport of geopotential come close to coinciding. This indicates that the linearized relationship does not hold well for highly nonlinear (nonstationary) state, but may apply for a quasi-stationary condition. Another feature which casts questions on the applicability of the linearized equation is that within the area of positive $\overline{v'T'}$ flux on day 30 of C2 (Fig. 9d) there is an area of $-\overline{w'\Phi'}$ (Fig. 4d). The only way that this would be possible would be that C exceeds $\bar{u}$. On day 30 of C2 $\bar{u}$ has a value of approximately 55 m/sec at this location. It is unlikely that C would exceed this value.

CHAPTER 4

ANALYSIS OF THE ZONAL MEAN CIRCULATION IN THE UPPER ATMOSPHERE

Recall that even though the highest point of the orographic forcing was at 45°N, the strongest flux of $\overline{w'\phi'}$ in the stratosphere was at about 70°N on day 18 of C1 and day 26 of C2. The latitude-height chart of $\overline{w'\phi'}$ on day 3 shows that the maximum flux of $\overline{w'\phi'}$ is near 35°N in the troposphere. As this eddy flux propogates into the stratosphere, it shifts northward to about 65°N. As the vertical flux of geopotential reaches a maximum in the stratosphere, the mean zonal meridional circulation also peaks.

4.1 Mean Meridional Circulation

Examining Figs. 10a and 10b for C1, we can see the zonal mean meridional circulation as noted by Matsuno (1971). This circulation was established by day 10 of the model integration. The circulation consists of rising motion in the polar region across the stratopause, southward motion in the lower mesosphere and sinking motion into the stratosphere at mid-latitudes. This circulation coincides with the area of maximum fluxes of geopotential, sensible heat, and momentum.

An interesting feature of this circulation is that it extends from the mesosphere to the troposphere such that the northerly portion of the cell's circulation is confined primarily to the troposphere.

From day 18 to day 30 of C1 there has been a weakening of the zonal mean meridional circulation and its center has shifted south from 65°N to 55°N. With Figs. 10c and 10d the evolution of the mean meridional velocity $\bar{v}_{max}$ can be followed. Figure 10c is the maximum of v plotted every fourth day to show changing mean amplitudes with time. Figure 10d is a latitude-time section taken at 40.5 Km which depicts $\bar{v}$ fluxuations in both latitude and amplitude. The first maximum of v occurs on day 14 and the second on day 26 which holds through day 30 with a minimum on day 22. It should also be pointed out that by day 34 the circulation cell is virtually dissolved.

To complete the meridional circulation analysis shown in Figs. 10a and 10b, we will look at the evolution of the vertical velocities with time. Figure 11a shows $\bar{w}_{max}$ (solid curve) and $\bar{w}_{min}$ (dashed curve) respectively of the northern and southern branch of the zonal mean meridional circulation and Fig. 11b depicts $\bar{w}$ as a function of time similar to Figs. 10c and 10d respectively.

It is obvious that Fig. 11a has a geometric configuration similar to Fig. 10c except that Fig. 11a has the mirror effect of the positive and negative vertical velocity maxima. These fluxating maxima indicate a pulsing meridional circulation.

For C2 we find that the mean meridional circulation on day 26 is very similar to C1 (Fig. 12a), but day 30 has a second circulation consisting of a northward maximum of $\bar{v}$ at 75°N and 40 Km and sinking motion near 90°N. This cell is of very short duration and is not depicted on the $\bar{v}_{max}$ evolution charts (Figs. 12c and 12d) or the $\bar{w}$ evolution charts (Fig. 13a or 13b). The C2 evolution charts of the

mean meridional maxima show three distinct maximum values of v. The first two surges of meridional circulation occur on the same day as C1. However, instead of the meridional circulation going to near zero on day 34 as in C1, it again increases through day 40. Because of this increase in activity on day 40, the model was integrated by Koermer through day 50. This integration showed that day 40 was the last day of significant increase. A second difference between C1 and C2 is that in C1 the meridional circulation began to shift south after day 26, whereas, in C2 the meridional circulation continued moving northward through day 40 (Fig. 12d and Fig. 13b). In Fig. 13a we again note a similar mirror-type image of the vertical velocity magnitudes. C2 also shows an approximate 8-12 day cycle.

4.2 Theorems of Noninteraction

Figure 14 is a graphic display of the relationships between the zonal mean $\overline{v'T'}$ (solid curves) and $\overline{w}$ (dashed curves). The relations given by Eqs. (53) and (54) represent time averaged relations ($^{\approx}$) between the zonal mean meridional circulation and the flux of sensible heat and the transport of zonal momentum.

$$\overset{\approx}{w} = \frac{1}{\gamma_d - \overset{\approx}{\gamma}} \left[- \frac{1}{a \cos\phi} \frac{\partial}{\partial \phi} \left(\overline{\overset{\approx}{v}\overset{\approx}{T}} \cos\phi \right) + \frac{\overset{\approx}{h}}{c_p} \right] \tag{53}$$

$$\overset{\approx}{v} = \frac{1}{f} \left[\frac{1}{a \cos\phi} \frac{\partial}{\partial \phi} \left(\overline{\overset{\approx}{v}\overset{\approx}{u}} \cos\phi \right) + \frac{\partial}{\partial p} \left(\overset{\approx}{w}\overset{\approx}{u} \right) - \frac{\tan\phi}{a} \left(\overset{\approx}{v}\overset{\approx}{u} \right) - \overset{\approx}{F}_1 \right] \tag{54}$$

From Eq. (53) we would expect rising motion to be in an area of

horizontal convergence of $\overline{\tilde{v}'\tilde{T}'}$. Likewise, in an area of horizontal divergence of $\overline{\tilde{v}'\tilde{T}'}$ there should be sinking motion. Figure 14a is a representative height-latitude chart depicting this relationship. The relationship seems to hold true for both C1 and C2. Equation (54) shows the relation between $\bar{v}$ and the momentum fluxes of $\overline{\tilde{u}'\tilde{v}'}$ and $\overline{\tilde{w}'\tilde{u}'}$. In the relation to $\overline{\tilde{v}'\tilde{u}'}$, $\bar{v}$ should be negative in the area of negative gradient, as well as the maximum negative portion of $\bar{v}$ at the center of $\overline{\tilde{v}'\tilde{u}'}$. Figure 14b indicates that $\frac{1}{a \cos \phi} (\overline{\tilde{v}'\tilde{u}'} \cos \phi)$ is the dominant of the $\overline{\tilde{v}'\tilde{u}'}$ terms. The $\overline{\tilde{w}'\tilde{u}'}$ term of Eq. (61) should give meridional flow in the area of maximum vertical gradient. Figure 14c indicates that while $\overline{\tilde{w}'\tilde{u}'}$ is a possible factor it is not the dominant influence on $\bar{v}$.

It may be pointed out from the following equation (Kao, 1981).

$$\overline{\tilde{w}\tilde{T}} = \frac{CpT}{g} \left\{ - \frac{1}{a \cos \phi} \frac{\partial}{\partial \phi} (\overline{\tilde{v}\tilde{T}} \cos \phi) - \frac{\partial}{\partial z} (\overline{\tilde{w}\tilde{T}}) \right\} \qquad (62)$$

and Eq. (53) that the region of zonal mean vertical flux of temperature generally coincides with that of zonal mean vertical velocity.

CHAPTER 5

EVOLUTION OF THE ZONAL MEAN MAXIMUM OF ZONAL VELOCITY, TEMPERATURE, AND CROSS CORRELATIONS OF u,v,w, and T.

Since the difference between a major and a minor warming in the stratosphere depends on the characteristic of polar night jet (PNJ), we will concentrate on the evolution of this jet. According to the WMO definition, if the PNJ mean winds reverse from westerlies to easterlies, then it is considered a major warming. All other strong warmings are classified as minor warmings.

5.1 Evolution of Zonal Mean Winds and Temperatures

In both cases we find that the PNJ becomes a separate entity on day 14 which corresponds to the first surge of meridional circulation.

For C1 (Fig. 15a) we note that the PNJ (solid line) holds steady from day 14 through day 22, then de-accelerates rapidly with the mean winds reversing on day 26. During the period of simulation, the mesospheric jet (dashed line) has a fairly steady decline through day 30, then gradually increases. The tropospheric jet (dot line) and the mid-latitude easterlies (dot dashed line) maintain a relatively even magnitude during the entire integration period. See Fig. 6d for jet locations.

For C2 (Fig. 15b) the intensity of PNJ increases slighty from day 14 through day 22, then de-accelerates. From day 30 to day 34, the de-acceleration rate slows during a transitory period. The C2 mesospheric jet has a much larger fluxation than the C1 jet. This is the opposite of the findings of Koermer and Kao (1980), in their analysis of the 1977 major and the 1976 minor warming. As in C1, the tropospheric and mid-latitude easterlies maintain relatively steady velocities.

The evolution of the changes of the zonal mean temperatures maxima of C1 are depicted in Fig. 16. Figure 16a for C1 shows a nearly linear increase in the stratospheric temperature maximum (solid curve) from day 10 through day 34, whereas the mesospheric temperature maximum experiences a steady decline through the simulation period. This indirectly shows that there is some law of compensation between the temperature changes in the stratosphere and those in the mesosphere.

For C2 we have a slightly different warming transition in the stratosphere, with a cooling period from day 30 to 34, and the final warming on day 38. To a large degree, we see a mirror effect of this stratospheric warming as cooling in the mesosphere.

The height of the warming maximum for C1 is fairly steady (solid line) (Fig. 16b), with some sinking during about the last half of the period. C2 (Fig. 17b), shows more oscillation in the vertical position of maximum warming (solid line) with its position rising through day 30, then sinking. The height of the maximum cooling (dashed line) changes quite dramatically (Fig. 16b), from day 14 to day 18 in C1 and then remains quasi-stationary with some shift in height simultaneously with the stratosphere warming height. C2 cooling height (dashed line) (Fig. 17b) does not have the rapid height change of C1, but rises daily

from day 14 through day 34. The sinking of the cooling maximum in the mesosphere and the downward shift of the stratospheric warming is not as simultaneous in C2 as in C1. The latitude of the stratospheric maximum warming position is closely correlated to the periods of maximum warming, especially in C2. These maximum temperature change areas are also closely related to the de-acceleration of the PNJ winds. As the area of maximum temperature change shifts north, the magnitude of the warming increases. There also seems to be some correlation between the rate of movement north and the rate of temperature change in the stratosphere. This holds true for both C1 and C2. In C2, as the area of maximum warming moves south from day 26 to day 34, it cools nearly 18°C. However, as it shifts northward, day 34 to day 38, it warms again.

The mesosphere cooling maximum shifts northward from day 10 through day 18 for C1 (Fig. 16c), and exhibits very little latitude changes thereafter. The C2 mesosphere cooling maximum has characteristics similar to C1 except it shifts northward from day 22 to day 26.

5.2 Evolution of Fluxes from Magnitude Time Charts and the Effect of Meridional Fluxes on Zonal Mean Temperature and Wind

Since the vertical flux of geopotential is the first perturbation to be formed from the orographic forcing, we will look at the evolution of the maximum values of this term first.

In C1 the vertical flux of geopotential has its maximum values in the mid-latitudes shifting northward with time (Fig. 18b). When the amplitude of $\overline{w^* \phi^*}$ reaches its peak on day 18 (Fig. 18a), the latitude

position seems to remain constant until the warming trend develops on day 22. Coinciding with the PNJ de-acceleration is the formation of an area of negative $\overline{w'\phi'}$ (shown by an N). As the warming progresses, the area maximum shifts south. C2 exhibits more and larger fluxations, but of shorter duration. As in C1, the maxima shift from the mid-latitudes to the polar regions near the beginning of the integration. As the amplitude of the maxima decrease (Fig. 19a), they seem to move south (Fig. 19b), and the amplitude of the minima increases (N). These minima seem to be related to the decrease in the meridional circulation and warming in the stratosphere.

The C1 meridional transport of mean zonal momentum maxima (Fig. 20a) has a very similar configuration to the vertical flux of geopotential maxima, except that it reaches its peaks four days earlier. The latitude center of these maxima does not reach the polar regions, but does show a northward shift (Fig. 20b) reaching its northernmost position on day 18. As with $\overline{w'\phi'}$, the divergent area of $\overline{u'v'}$ forms at the beginning of the warming.

In C2 the zonal mean meridional flux of zonal momentum maxima evolution configuration (Fig. 21a), is very similar to the maxima amplitude of $\overline{u'v'}$ increases, the latitude position (Fig. 21b), indicates convergence. As divergent areas form, the latitude position of the convergence maxima shifts south and the magnitudes decrease.

The mean zonal meridional flux of zonal momentum should have a direct effect on the mean zonal winds as shown in Eq. (63). It can be shown

$$\left(\frac{\overline{\partial u}}{\partial t}\right)_s = f_s\overline{v} - \frac{1}{a\cos^2\phi}\frac{\partial}{\partial\phi}\left(\overline{vu}\cos^2\phi\right)_s - \frac{\partial}{\partial z}\left(\overline{wu}\right)_s \qquad 636)$$

that at 68.9°N the turbulent transfer of zonal momentum and the Coriolus torque were the dominant terms of the relationship. However, these terms were of opposite sign, and thus nearly negated the effect.

The small feature which does have a direct correlation to the warming is the divergent area of $\overline{u'v'}$ in the polar mid-stratosphere. As the mean zonal meridional flux of zonal momentum changes sign, it would enhance the Coriolis effect on de-accelerating the PNJ winds.

The vertical transport of zonal momentum ($\overline{w'u'}$) has a significantly different configuration from $\overline{u'v'}$. In C1 its maximum magnitudes peak on day 18 and then gradually decline to day 26 with only a minor peak on day 30 (Fig. 22a). The C2 configuration (Fig. 22b) at $\overline{w'u'}$ has a similar time arrangement of maxima and minima to $\overline{u'v'}$ through day 30 after which there is no correlation. These configurations plus the magnitude of the term suggests that $\overline{w'u'}$ does not have a direct influence on the stratospheric warming.

The mean zonal meridional transport of sensible heat has nearly the same configurations as $\overline{u'v'}$ for each respective case (Figs. 23a and 24a). The major difference being that $\overline{v'T'}$ does not have the negative maximum in C1 or C2 that was evident in $\overline{w'\Phi'}$ and $\overline{u'v'}$. It should be noted, however, that the evolution of the amplitude (Fig. 23a), of the maxima of $\overline{v'T'}$ in C1 has a very similar configuration to the C1 $\overline{u'v'}$ maxima evolution. After day 30 the area of $\overline{v'T'}$ has dissolved to the point that no one center can be distinguished. In C2 the latitude position of $\overline{v'T'}$ does not indicate that magnitude relation that was observed in the previous flux terms. It does, however, indicate a gradual poleward movement of warm air which is consistent with the findings of Quiroz, et al. (1975).

Equation (64) relates the meridional and vertical transport of sensible heat to the changes of temperature with time, where $(\ )_s$ is the transient term.

$$\left(\frac{\partial \bar{T}}{\partial t}\right)_s = -\frac{1}{a \cos\phi}\frac{\partial}{\partial \phi}\left(\overline{v'T'}\cos\phi\right)_s - \frac{\partial}{\partial p}\left(\overline{w'T'}\right)_s + \frac{R'}{c_p p}\left(\overline{w'T'}\right)_s , \quad (64)$$

Using a simple differencing program to find gradients, it was determined that the meridional transport term is approximately an order of magnitude larger than vertical transport term and thus probably more important. This is indirectly confirmed by Figs. 16 and 17 which show the correlation between meridional shift of the temperature change maximum an the magnitude of that change.

The evolution similarity of magnitudes and frequencies of $\overline{v'T'}$ and $\overline{u'v'}$, as depicted in Figs. 20a and 22a and in Figs. 21a and 23a, suggests that a relation exists between these fluxes. Equation (58) relates $\tilde{w}$ to $\overline{v'T'}$ and Eq. (59) relates $\tilde{v}$ to $\overline{v'u'}$. In the indirect meridional circulation as shown in Fig. 10a, we know that $\tilde{w}$ and $\tilde{v}$ are related by the continuity equation. Thus an indirect relation should exist between $\overline{v'T'}$ and $\overline{u'v'}$.

CHAPTER 6

ANALYSIS OF SPECTRAL INFLUENCE ON THE CHANGE OF THE MEAN ZONAL WINDS AND MEAN ZONAL TEMPERATURE

The diagrams of this chapter are based on a Fast Fourier Transform of u, v, w, T, and Φ into their spectral components. From this spectral data base, we computed the spectral zonal mean amplitudes of the velocity components denoted as $A_{(\ )}(k)$ with (k) representing the wavenumber. The cospectral values are designated as $C_{(\ )(\ )}(k)$ and represent the zonal mean of the flux terms. When selecting the area maxima, we focused our attention on the polar region since this is the region of the stratospheric warming. The latitude-height charts were selected to maintain continuity with previous chapters and to highlight critical periods in the warming process that were indicated on the evolution charts.

The magnitude evolution graph periods are based on the time periods of maximum zonal velocity changes in the polar stratosphere. Thus for C1, we selected days 16 through 30 and for C2 days 22 through 40. Since wavenumber 1 and wavenumber 2 (hereafter referred to as wave 1 and wave 2 respectively) have the dominant wave amplitudes of this study [Koermer (1960)], we will refer to wavenumber three and wavenumber four only when they have significant magnitudes compared to wavenumbers one and two.

6.1 Amplitude and Evolution Analysis of $A_u(k)$, $A_v(k)$, and $A_w(k)$

One of the most striking features of C1 is that for $A_u(k)$ (Fig. 25), $A_v(k)$ (Fig. 26), and $A_w(k)$ (Fig. 27) wave 1 dominates the mesosphere and wave 2 dominates the stratosphere. This holds true throughout the warming period even though wave 1 does seem to propagate downward into the stratospheric polar region by the end of the warming. This implies that wave 1 has a greater vertical penetration ability than wave 2.

$A_u(1)$ (Fig. 25a) starts with three wave centers symmetrically spaced from the equator to the North Pole. $A_v(2)$ also has three centers of maximum, one of which is located in the lower stratosphere. This suggests that wave 2 may have more interaction with the troposphere than wave 1.

In contrast to $A_u(k)$ Fig. 26 shows that $A_v(k)$ only has one main center which is centered in the polar regions. Both $A_u(2)$ and $A_v(2)$ are shifted slightly south of $A_u(1)$ and $A_v(1)$ respectively. This southward shift also seems to hold true for $A_w(k)$ (Fig. 27), but is not as evident because of the multiple cells. In addition to the height difference of wave 2 as compared to wave 1, we note (Fig. 27) that wave 2 has a dominant cell near the tropopause region at about 25° to 30°N (Figs. 27c and 27d). Wave 1 also has this maximum area, but it is in the equatorial region and does not seem to be connected with the stratosphere (Figs. 27a and 27b).

From Fig. 28 we can see the evolution of the velocity amplitudes from day 16 through day 30. Even though $A_u(1)$ is the largest quantity

of the two waves (Fig. 28a), it should be remembered that $A_u(1)$ is mainly in the mesosphere and $A_u(2)$ is dominant in the stratosphere. Figure 28b indicates a slightly different picture in terms of dominant wavenumber in that after day 20 $A_v(2)$ has the largest magnitude. $A_w(k)$ shown in Fig. 28c shows C1 starting with a dominant wave 1 vertical velocity shifting to a dominant wave 2 on day 24. This is viewed with interest since it occurs during the middle of the warming, but its total significance is not understood. The relatively large vertical velocity located at about 35°N and 13 Km seems to indicate that wave 2 is the dominant force of the model. This would seem only logical since our orographic effects also have a wave 2 form (except that in C2 we see waves 1, 3, and 4 also contribute to the vertical velocity even though it also has the same forcing).

C2 is similar to C1 in that $A_u(k)$ (Fig. 29) has three maxima, $A_v(k)$ (Fig. 30) has one maximum, and these maxima are in approximately the same latitudinal location. They are also similar in that wave 1 tends to be at a higher altitude than wave 2, but as the dominant wave shifts from wave 2 to wave 1, wave 2 shifts downward. A difference between the cases is that $A_w(k)$ (Fig. 31) has two maxima showing. This may be due to the stronger vertical velocities. A second major difference between the cases is the pronounced shift of dominant wavenumber from wave 2 to wave 1 in C2.

The magnitude evolution graphs show a significant change in $A_u(k)$ (Fig. 32a) and $A_v(k)$ (Fig. 32b) from dominant wave 2 to dominant wave 1. It is interesting to note that this occurs during the period of a strong warming, but may not be significant since the second warming pulse of C2 does not have this characteristic. The decrease of wave 2

with the increase of wave 1 strongly suggests a non-linear interaction between the waves. This also occurs in $A_w(k)$ (Fig. 33a and 33b). As waves 1 and 3 decline, waves 2 and 4 increase from day 22 to day 24. Then wave 2 decreases rapidly as wave 4 continues to increase and wave 3 oscillates upward. These types of interactions continue through the warming period, forming a complex pattern of non-linear interaction. The C2 $A_w(k)$ is one of the few values that have significant wave 3 and 4 values. It is also interesting to note that the dominant vertical wave at the tropopause is wave 3 in contrast to C1 where it was wave 2.

6.2 Cross Spectral Analysis of u, v, w, T and Φ

The first quantity to be examined is the zonal mean of the meridional transport of zonal momentum $C_{uv}(k)$. From Fig. 34a and 34c it is easy to see that the momentum flux is consistent with the C1 velocities in that wave 1 is dominant in the mesosphere and wave 2 is dominant in the stratosphere. In addition, wave 2 has a significant flux of momentum in the equatorial latitudes. By day 24 of C1 there is still a strong positive flux of $C_{uv}(k)$ in the mesosphere at about 55°N, but an area of divergent momentum has developed at 75°N in the lower mesosphere. This same phenomena is also true with wave 2 only at a lower altitude such that there is a significant area of divergenct momentum in the troposphere.

C2 (Fig. 35) is very different from C1 concerning $C_{uv}(k)$. First, waves 1 and 2 are closer to the same altitude. Second, wave 1 is primarily divergent. Probably the most distinguishing difference between

the C1 $C_{uv}(k)$ and the C2 $C_{uv}(k)$ is that its magnitudes are smaller than C1 before the warming, but significantly larger after some warming. Additionally C2 has no significant convergence or divergence of $C_{uv}(k)$. By comparing Figs. 25a, 26a, and 34a, it can be seen that the maximum $C_{uv}(k)$ occurs between the maximum of $A_u(k)$ and $A_v(k)$. This implies that the location and amplitude of $C_{uv}(k)$ is a function of the phase relation between $A_u(k)$ and $A_v(k)$. This implication helps explain the pulsing of the meridional circulation. The time evolution of $C_{uv}(k)$ for C1 (Fig. 36a) shows a decline of wave 1 throughout the critical simulation period with wave 2 declining from day 16 to day 22, then increasing rapidly during the peak of the warming. But, characteristic of C1, both wave 1 and wave 2 form divergent areas of $C_{uv}(k)$ during the wind reversal period. This divergent momentum is consistant with the findings of O'Neill and Taylor (1979).

Figure 36b is the C2 maximum magnitude evolution of $C_{uv}(k)$. As is characteristic of C2, it depicts the more rapid fluxuations of momentum transport. The two peaks of divergence of wave 1 have a direct correlation to the 2 warming periods that C2 experienced. From Eq. (58) (Kao, 1980)

$$\frac{\partial \bar{u}}{\partial t} = -\sum_{k=-\infty}^{\infty} \left\{ \frac{1}{a \cos \phi} \frac{\partial}{\partial \phi} [v(k,t)u(-k,t)\cos\phi] + \frac{\partial}{\partial z} [w(k,t)u(-k,t)] \right.$$

$$\left. - \frac{\tan \phi}{a} u(k,t)v(-k,t) \right\} + f\bar{v} + \bar{G}_1(0,t) \qquad (65)$$

expect that as the divergence increases, the mean zonal velocity would increase. In Eq. (58) u(k,t), v(k,t) and w(k,t) one Fourier longitude transform of u, v and w respectively. At first glance, this seems to

be questionable for both C1 and C2. In C1 our largest divergent magnitude occurs on day 24, the time of maximum zonal velocity decline. In C2 we have maximum divergence on days 30 and 36. Day 36 is during a period of strong zonal mean decrease and day 30 is a time of changing de-acceleration, but still a period of declining velocities. However, we should note that the first term of the equation is a gradient and thus the equation does hold true at about 80°N.

The cross-spectrum of the vertical transport of geopotential [$C_{w\phi}(k)$] C1 shows (Fig. 37) most flux to be north of 60°N. Again it should be noted that even though wave 1 has over twice the magnitude as wave 2 on day 18 (Figs. 37a and 37c), it is wave 2 that is in the area of the wind reversal. By day 24, which is the middle of the major warming, these distinct maximum areas of wave 1 and wave 2 (Figs. 37b and 37d) have become much less organized, with wave 1 propagating into the stratosphere.

In C2, the $C_{w\phi}(k)$ does not have the degree of altitude separation of C1, but the wave 2 magnitude is much larger, and thus could be overshadowing the altitude differences of wave 1 and wave 2.

By day 30 of C2 (Fig. 38b) and C1 (Fig. 37b) there is an area of negative $C_{w\phi}(1)$ which has shifted downward slightly into the stratosphere. As we look at Fig. 39, these areas of negative $C_{w\phi}(1)$ take on an increased significance. This is due to their direct correlations to the PNJ decreases in both C1 and C2.

Figure 39 indicates a major difference between C1 and C2 concerning $C_{w\phi}(k)$. In C1 both wave 1 and wave 2 have a general decrease in magnitude (Fig. 39a). But C2 shows (Fig. 39b) a non-linear interaction between the two waves from day 24 to day 32.

Figure 40 shows that the areas of maximum zonal mean meridional transport of sensible heat have very similar locations to those of $C_{vu}(k)$ (Fig. 34) and $C_{w\phi}(k)$ (Fig. 37). It is also interesting to note that for C1 all three fluxes have shown a downward shift of the flux with time, particularly $C_{vu}(2)$ and $C_{vT}(2)$.

In contrast, C2 shows a slight upward shift of the fluxes (Figs. 35 and 38) with time, especially $C_{vT}(k)$ (Fig. 41).

The evolution of $C_{vT}(k)$ forms a different configuration than $C_{vu}(k)$ and $C_{w\phi}(k)$. However, in C1 there is a good correlation between the increase of $C_{vT}(2)$ (Fig. 42a) and the poleward shift of the maximum temperature changes (Fig. 16c). The $C_{vT}(k)$ of C2 (Fig. 42b) seems unique in that there were no good correlations evident, with the exception of the non-linear interaction of waves 1 and 2.

6.3 Polar Projections of Waves

The advantage of the polar projection of the v' is that we can see the horizontal distribution and the perturbation velocities at different levels in the model. By counting the number of alternating negative and positive cells of meridional perturbations, we can indirectly show the number of waves present.

We have chosen 7.5 Km, 40.5 Km, and 67.5 Km to represent the troposphere, stratosphere, and mesosphere respectively. For the troposphere, we selected three days to show the wave evolution, but since the upper atmosphere has less wave fluxation we selected only two days.

At 7.5 Km in C1, day 14 (Fig. 43a) we have wave 2 nearly symmetrical positioned around the North Pole. By day 18 (Fig. 43b), the wave amplitudes have nearly doubled with a weak wave three forming near 0°

longitude. By day 30 (Fig. 43c), the third wave has strengthened and the North Pole is under the influence of a weak ridge. In the stratosphere on day 18 (Fig. 44a), there is a clear wave 2 with the turbulant velocities nearly equal to the zoan mean velocities. By day 30 (Fig. 44c), the waves have weakened and appear to possibly be in a transition from wave 2 to wave 1. The mesosphere starts with a wave 1 (Fig. 44b) and shifts to a weak wave 2 by day 30 (Fig. 44d). The dominant wave has shifted into the Eastern Hemisphere.

C2 shows a similar wave configuration on day 14 at 7.5 Km (Fig. 45a). This pattern is still similar on day 18 though less symmetrical than C1 (Fig. 45b). By day 30, however, the troposphere has shifted to a wave 4 configuration (Fig. 45c) instead of the wave 3 pattern of C1. At 40.5 Km on day 18 (Fig. 46a), there is a symmetrical wave 2. However, by day 30 (Fig. 46c), these waves have begun to shift to a wave 1 centered at the North Pole. The mesosphere starts with essentially a wave 1 configuration on day 18 (Fig. 46b). The wave 1 continues to dominate the 67.5 Km level through the warming period even though it is distorted some by a weak wave 2 (Fig. 46d).

CHAPTER 7

CONCLUSION

Using an orographic forcing of a combination of wavenumbers 1 and 2 in the troposphere, major (case 1) and minor (case 2) stratospheric warmings were simulated with a 31-layer primitive equation, spectral model consisting of a 5-layer troposphere, 12-layer stratosphere and 14-layer mesosphere. An analysis of the data resulting from the simulations indicated several similarities and differences between the warmings. Case 1 had a weak polar vortex and case 2 had a strong polar vortex. The effect of the forcing on the zonal winds was to induce wave motion, meridional and vertical flux of momentum and sensible heat in the model atmosphere. The vertical flux of geopotential began near 45°N, then shifted northward. On about an eight to twelve day cycle, the meridional and vertical fluxes of momentum and sensible heat reach a peak in magnitude that coincided with the peak of the meridional circulation. With the first peak of the meridional circulation, the polar night jet became a distinct feature. The second peak of meridional circulation coincided with the wind reversal in case 1 and a significant decrease in the mean polar winds in case 2. The meridional circulation did not reach a third peak in case 1, but in case 2, it was associated with a further de-acceleration of the polar night jet.

The similarity of the configurations of the amplitude maxima evolution of the turbulent transfer terms is evident in both cases.

The reason for this is probably a result of the indirect relationship between the meridional flux of sensible heat and the meridional transport of zonal momentum that is shown to exist as a result of the theorems of non-interaction and the continuity equation. These relationships would also provide a possible explanation for the periodicity of the indirect meriodional cell circulation, as well as the semi-linear temperature changes in the stratosphere.

In both cases we found that wave number 1 waves were dominant in the mesosphere and wave number 2 waves were dominant in the stratosphere. However, during the warming, wave number 1 waves became significant in the stratosphere. Case 2 exhibited more evidence of nonlinear interaction than case 1.

The validity of the assumptions made in deriving the relationship between the vertical flux of geopotential and the meridional flux of sensible heat from the linearized governing equations was tested with the use of the data generated from the numerical model analyzed. We found that for the quasi-stationary state there was some correlation between the linearized theory and the zonal mean latitude-height positions of the fluxes. However, for the nonstationary condition of the warming process, the correlation become poor. This tends to raise questions about the validity of the application of the relationship between the vertical flux of geopotential and meridional flux of sensible heat derived from the linarized governing equations to nonlinear processes, and therefore, the concept of the critical level to the process in the developing stage of strong stratospheric warmings.

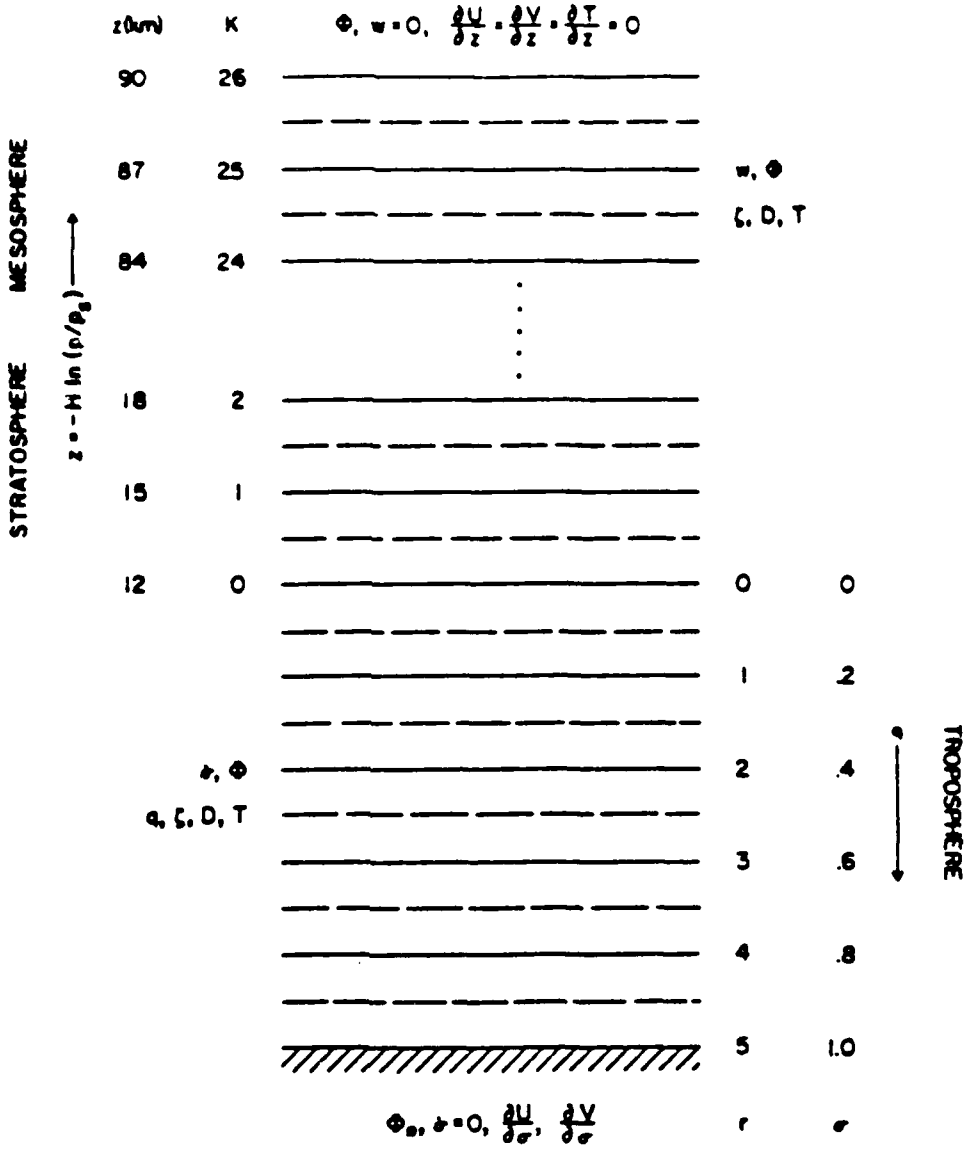

Fig. 1. Model schematic. Dashed/solid lines represent prognostic/diagnostic levels respectively. Boundary conditions are specified at top and bottom boundaries (Koermer, 1980). Used by permission.

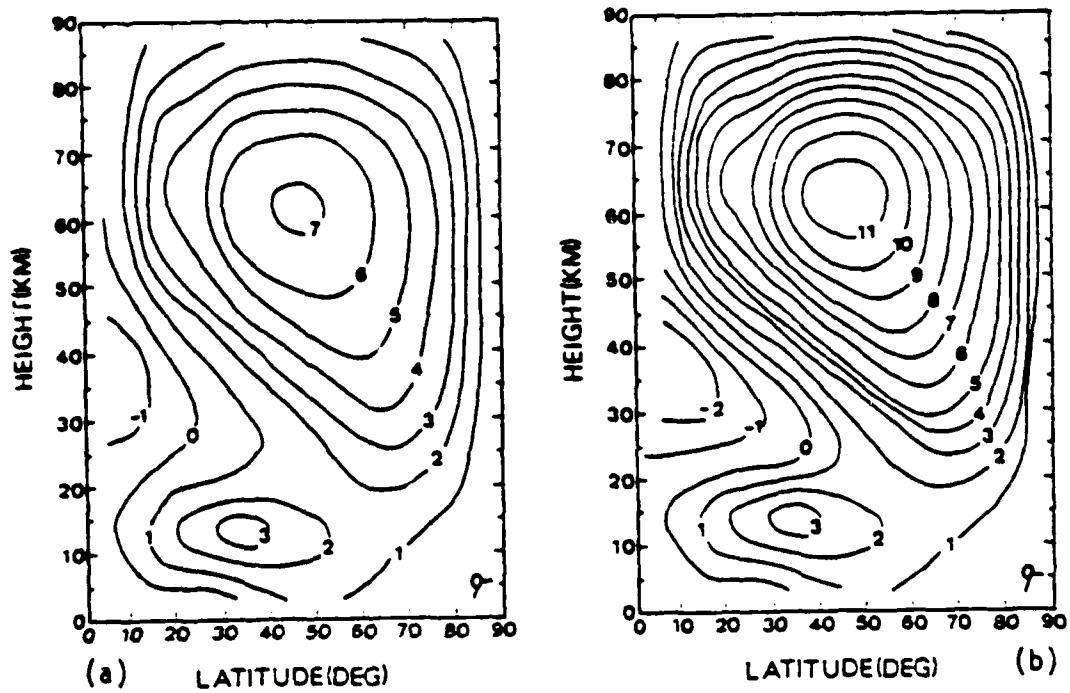

Fig. 2. Latitude-height sections of initial mean zonal wind (x 10 m s^{-1}) for (a) case 1; and (b) case 2 (Koermer, 1980). Used by permission.

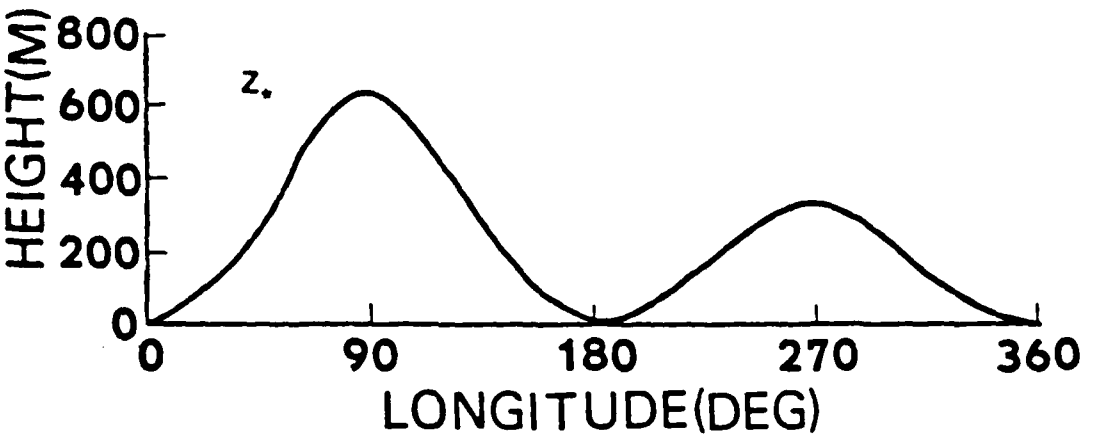

Fig. 3. Maximum longitudinal surface height distribution at 45°N (Koermer, 1980). Used by permission.

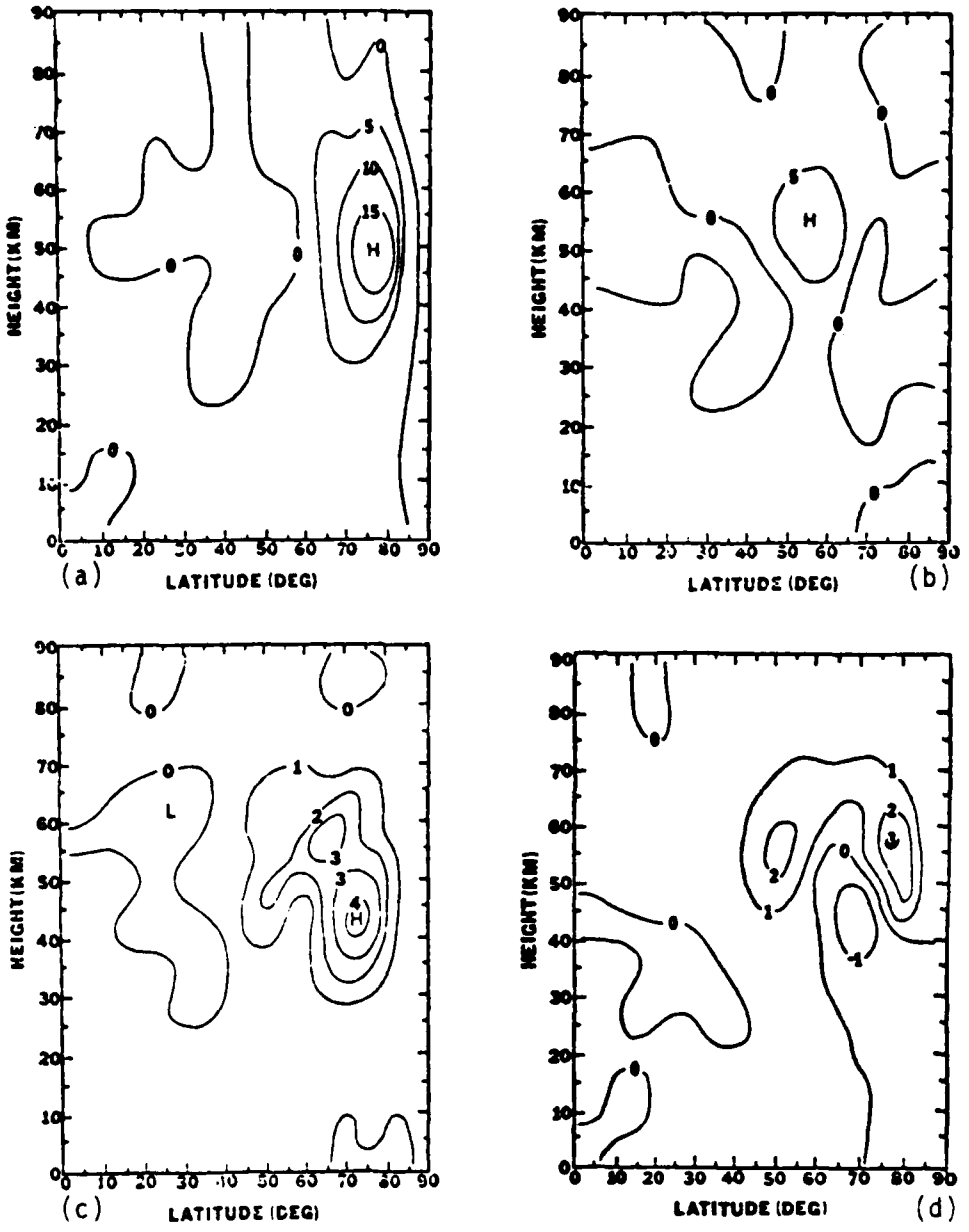

Fig. 4. Latitude-height sections of zonal mean vertical flux of geopotential for (a) case 1, day 18; (b) case 1, day 30; (c) case 2, day 26; (d) case 2, day 30. Units for (a) and (b) are (x 10 m^3 s^3). Units for (c) and (d) are (x 10^2 m^3 s^{-3}).

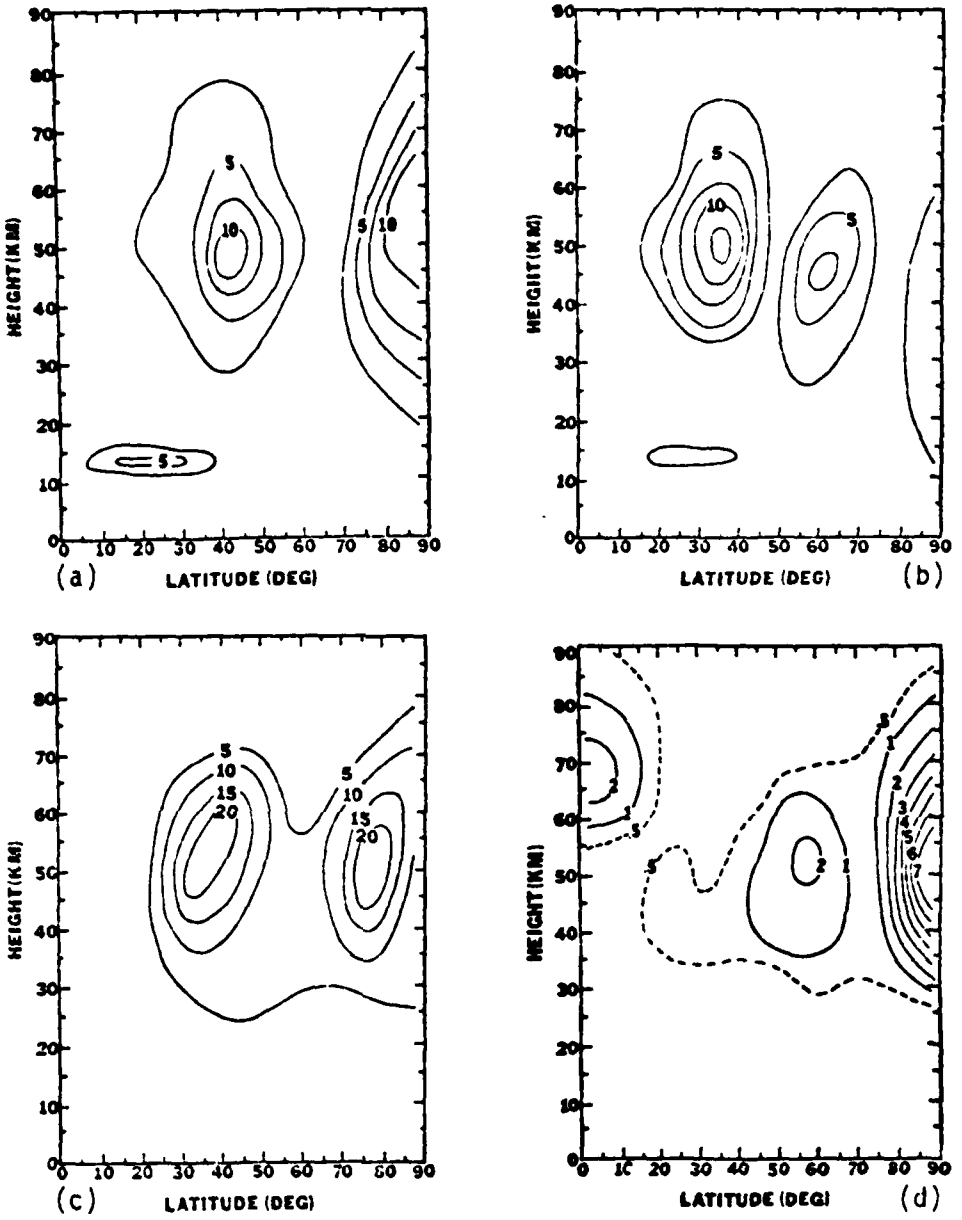

Fig. 5. Latitude-height sections of the zonal mean variance of u for (a) case 1, day 18; (b) case 1, day 30; (c) case 2, day 26; (d) case 2, day 30. Units for (a), (b), (c) are (x 10^2 m^2 s^{-2}). Units for (d) are (x 10^3 m^2 s^{-2}).

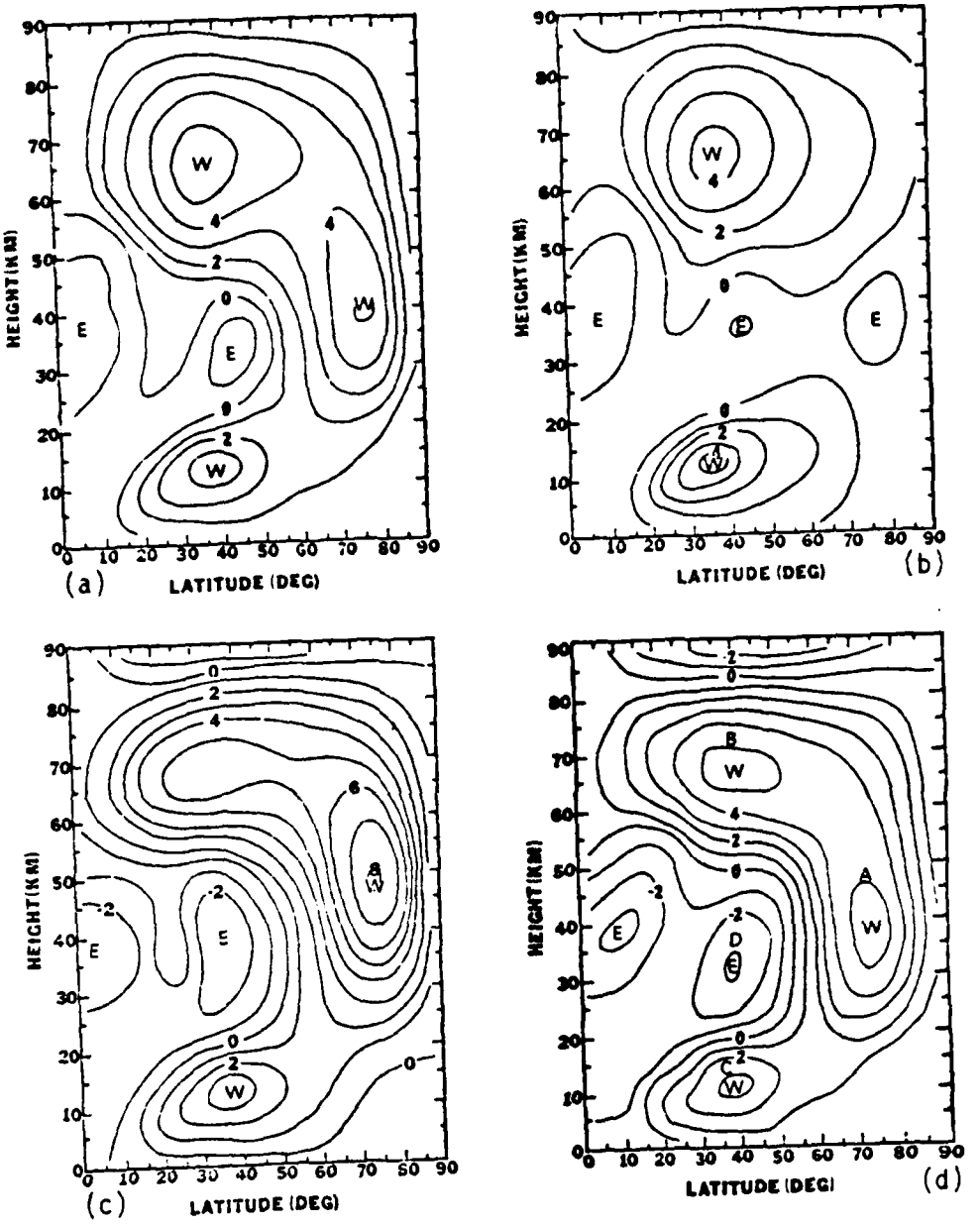

Fig. 6. Latitude-height sections of the zonal mean zonal velocity (x 10 m s^{-1}) for (a) case 1, day 18; (b) case 1, day 30; (c) case 2, day 26; (d) case 2, day 30.

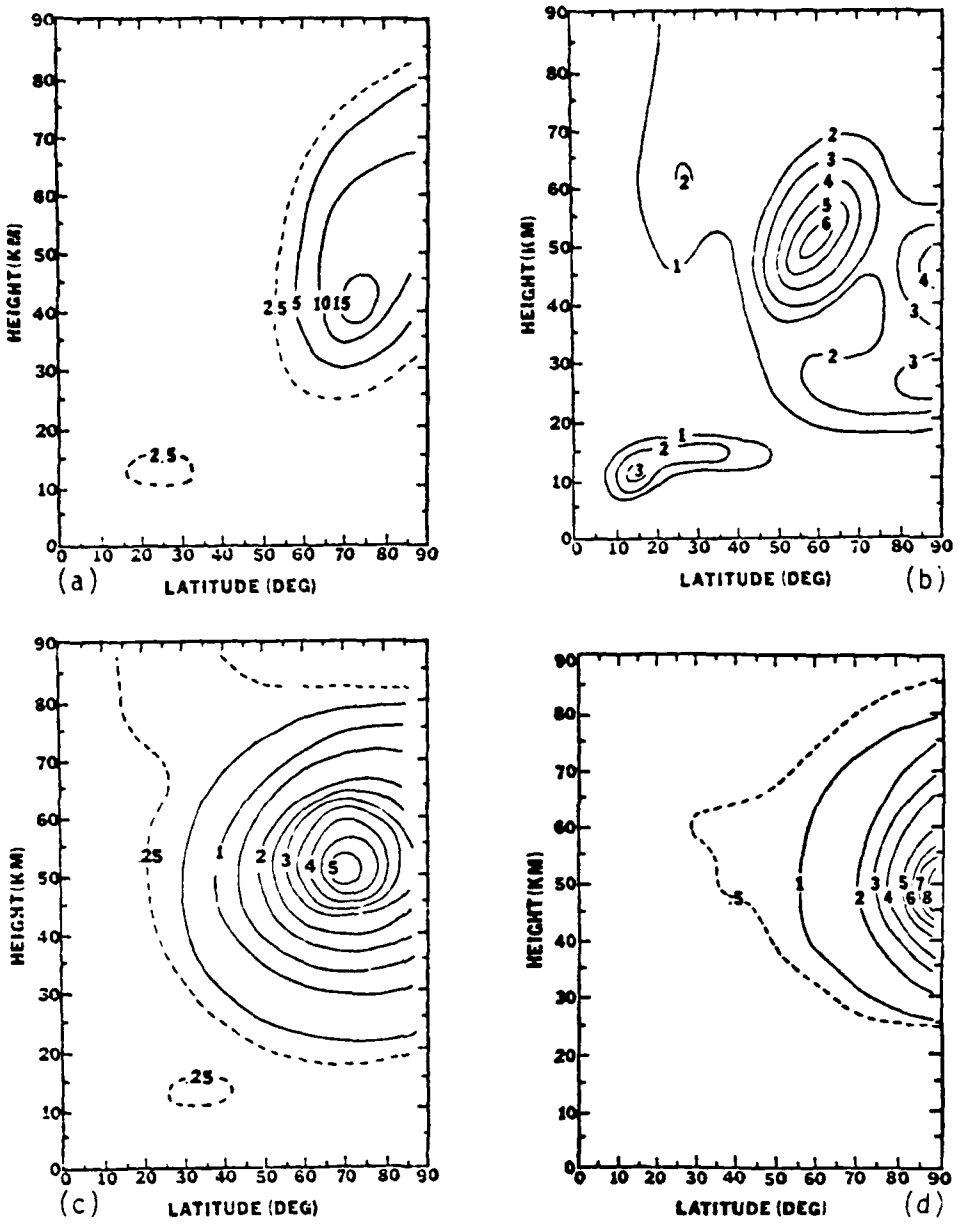

Fig. 7. Latitude-height sections of the zonal mean variance of the meridional wind for (a) case 1, day 18; (b) case 1, day 30; (c) case 2, day 26; (d) case 2, day 30. Units for (a) and (b) are (x 10^2 m^2 s^{-2}). Units for (c) and (d) are (x 10^3 m^2 s^{-2}).

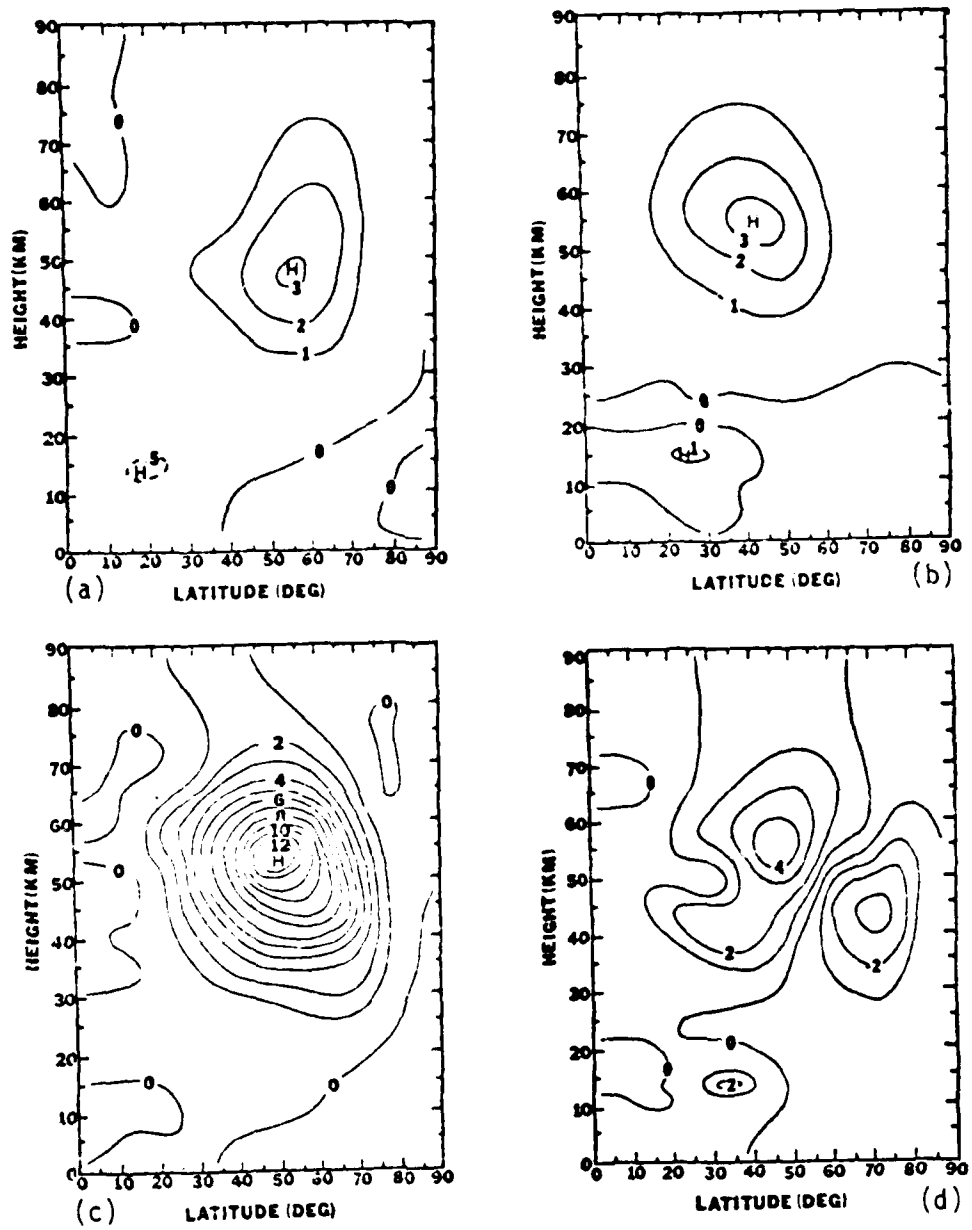

Fig. 8. Latitude-height sections of the zonal mean meridional flux of zonal momentum (x 10^2 m^2 s^{-2}) for (a) case 1, day 18; (b) case 1, day 30; (c) case 2, day 26; (d) case 2, day 30.

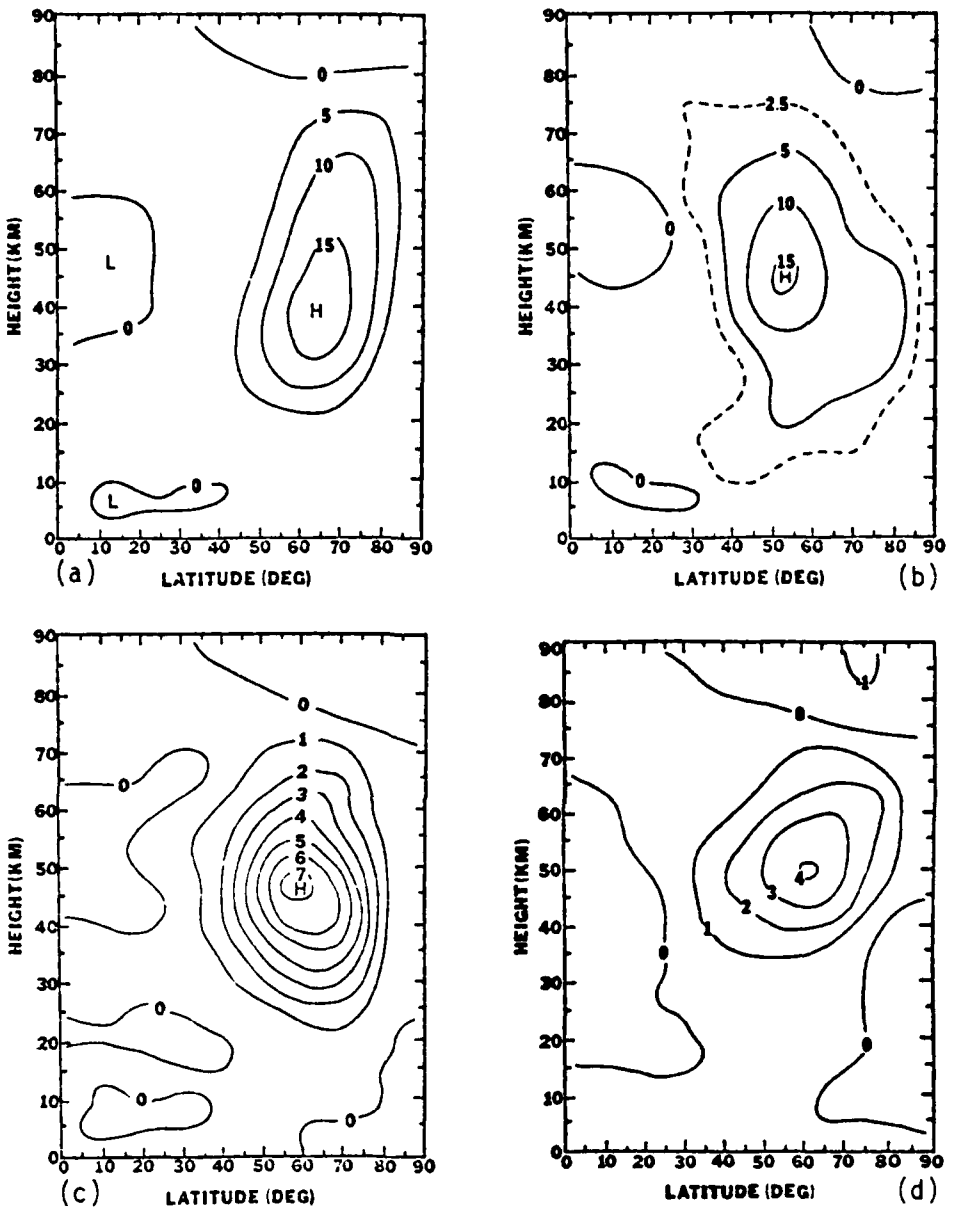

Fig. 9. Latitude-height sections of the zonal mean meridional flux of sensible heat for (a) case 1, day 18; (b) case 1, day 30; (c) case 2, day 26; (d) case 2, day 30. Units for (a) and (b) are (x 10 m s^{-1} °K). Units for (c) and (d) are (x 10^2 m s^{-1}).

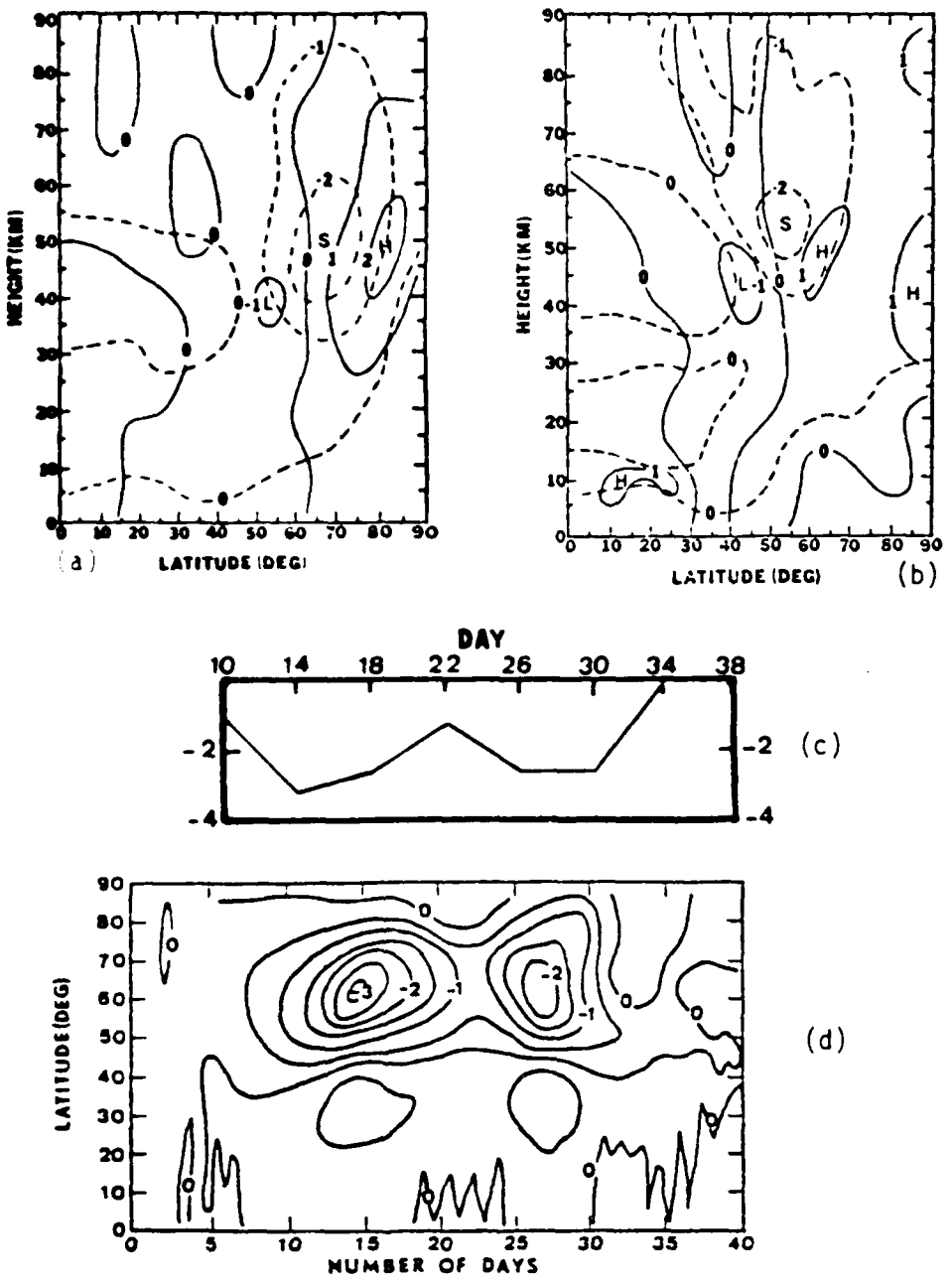

Fig. 10. (a) and (b) are latitude-height sections for case 1 with dashed/solid lines being zonal mean meridional velocity (m s^{-1}) and zonal mean vertical velocity (x 10^{-2} m s^{-1}) respectively. (c) case 1 zonal mean meridional velocity maximum evolution; (d) (Koermer, 1980) case 1 latitude-time section of the zonal mean meridional velocity at 40.5 Km. Units for (c) and (d) are (m s^{-1}). Used by permission.

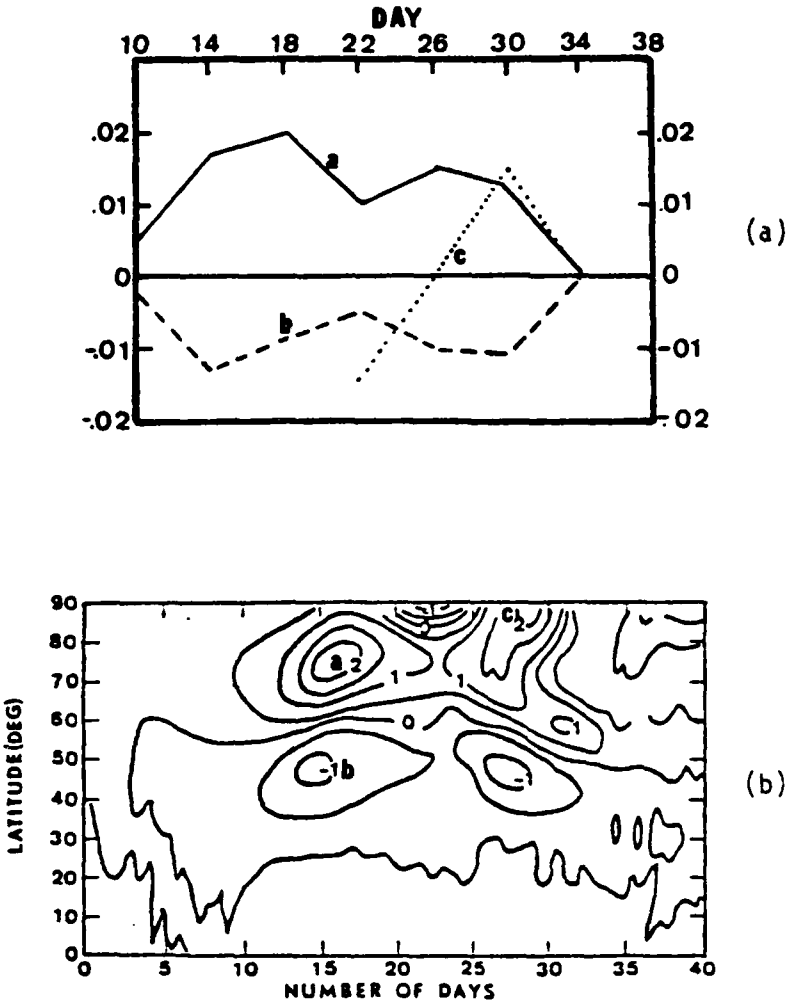

Fig. 11. Case 1 mean vertical velocities (10^{-2} m s^{-1}) (a) velocity maxima evolution; (b) (Koermer, 1980) latitude-time section at 40.5 km. Used by permission.

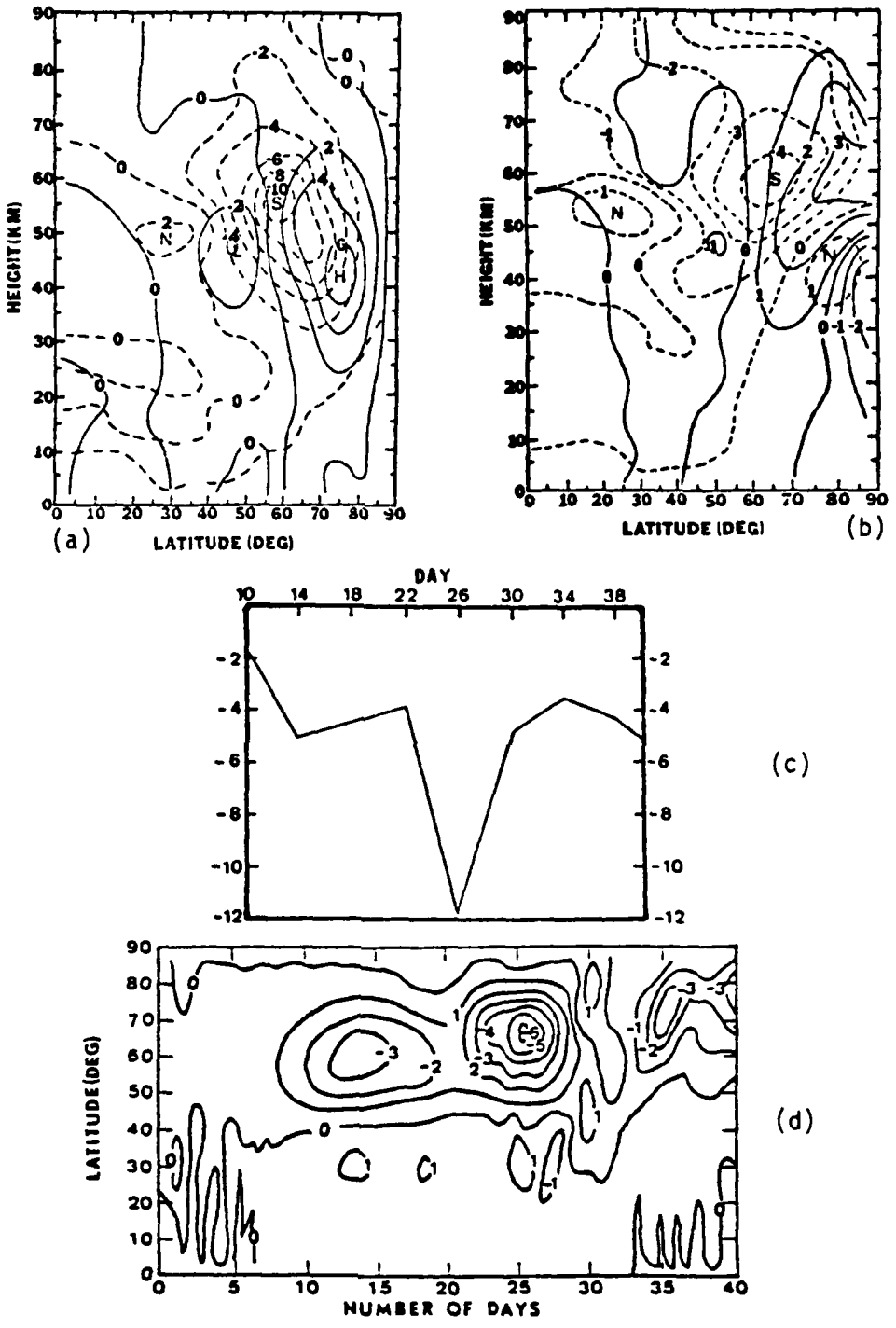

Fig. 12. Same as Fig. 10 except for case 2.

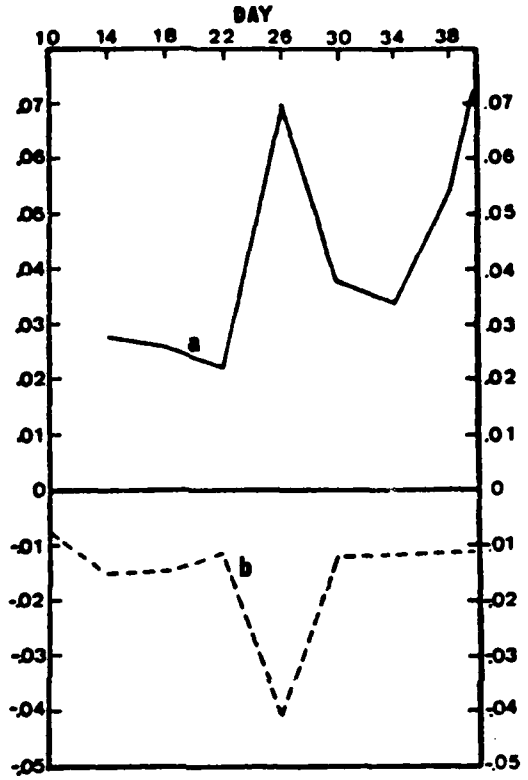

(a)

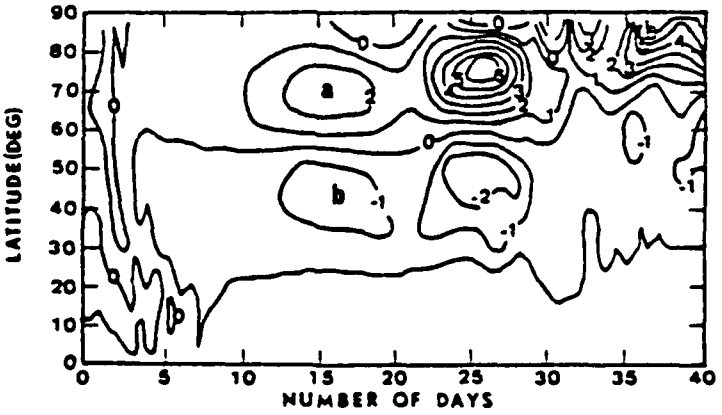

(b)

Fig. 13. Same as Fig. 11 except for case 2.

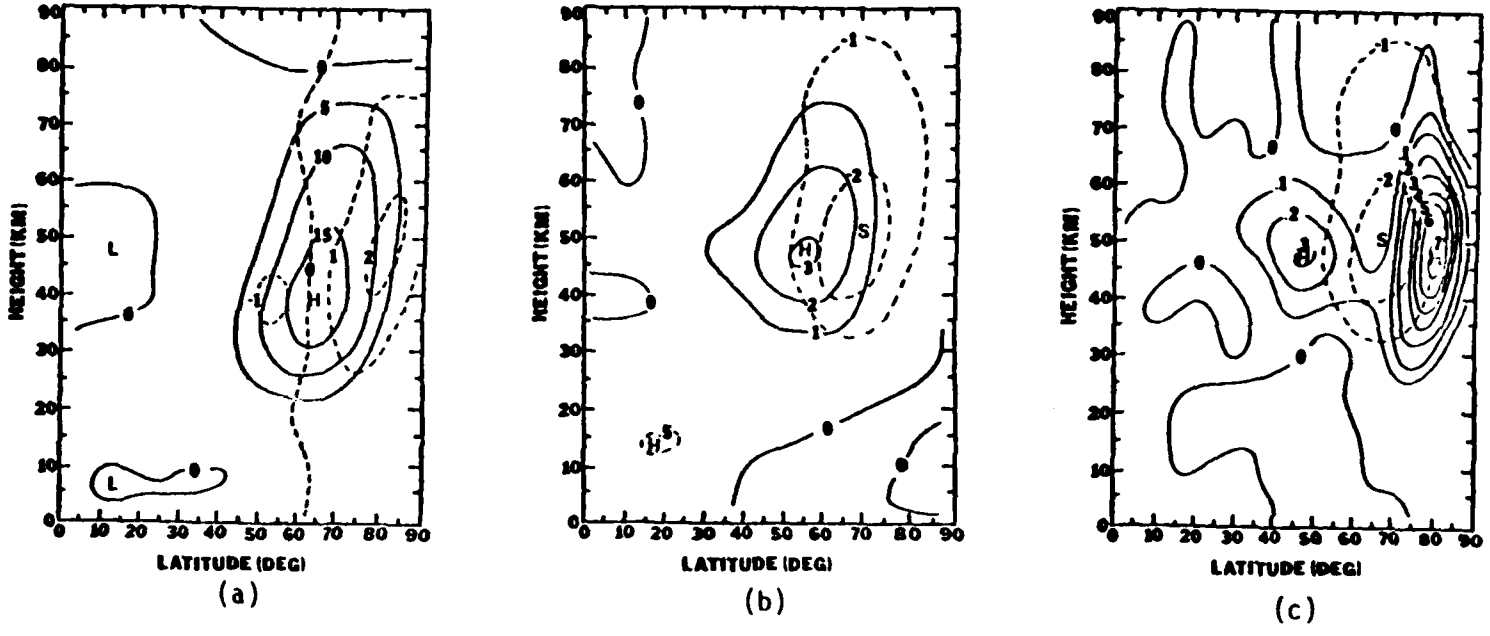

Fig. 14. Case 1, day 18 example of (a) zonal mean vertical velocity (dash line) superimposed on zonal mean meridional flux of sensible heat (solid line). Units are ($\times 10^{-2}$ m s^{-1}) and ($\times$ 10 m s^{-1} °k) respectively. (b) zonal mean meridional velocity (dashed line) superimposed on zonal mean meridional flux of zonal momentum (solid line). Units are (m s^{-1}) and (m^2 s^{-2}) respectively; (c) zonal mean meridional velocity (dashed line) superimposed on the zonal mean vertical transport of zonal momentum (solid line). Units are (m s^{-1}) and (m^2 s^{-2}) respectively.

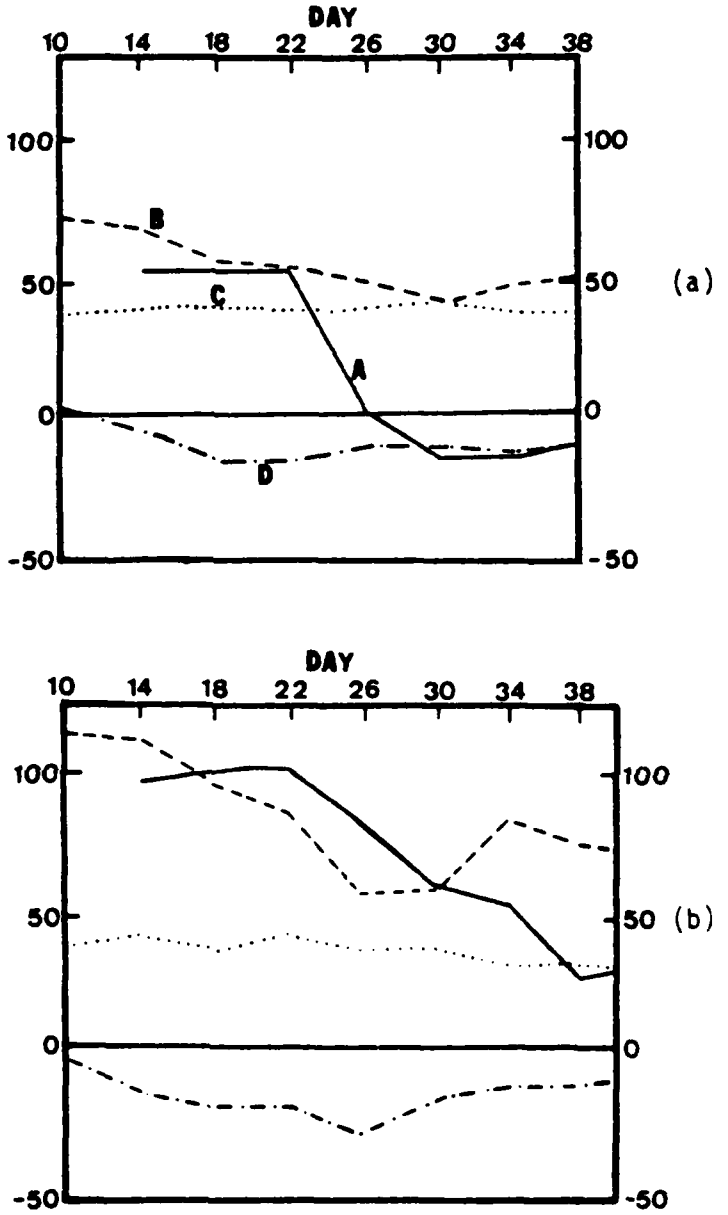

Fig. 15. Evolution of mean zonal wind maxima (m s^{-1}) with solid line being polar night jet, dash line being mesospheric jet, dotted line being tropspheric jet, and dot dashed line being mid-latitude easterlies for (a) case 1; (b) case 2.

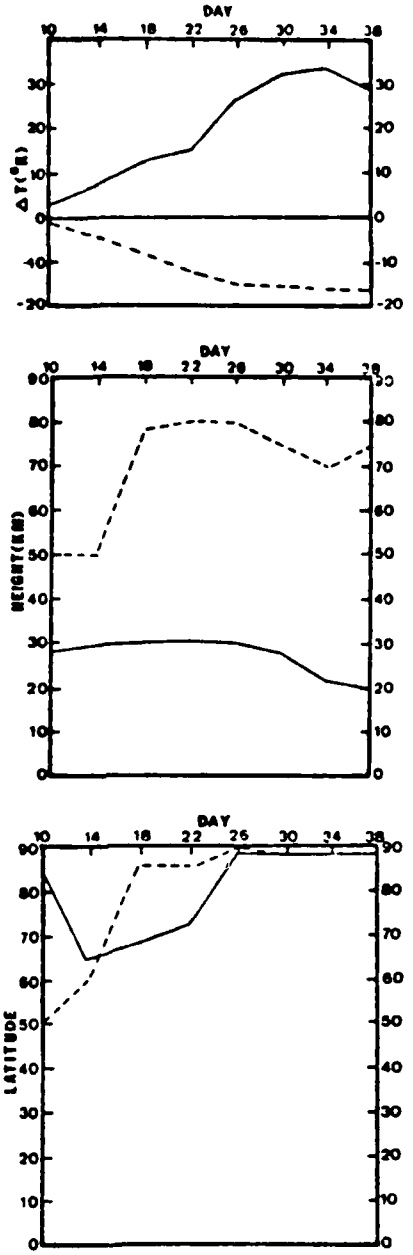

Fig. 16. Temperature evolution charts (solid line is stratosphere warming, dashed line is mesosphere cooling) for case 1 of (a) temperature maximum change with time (°C); (b) height-time evolution of temperature maximum changes; (c) latitude-time evolution of temperature maximum changes.

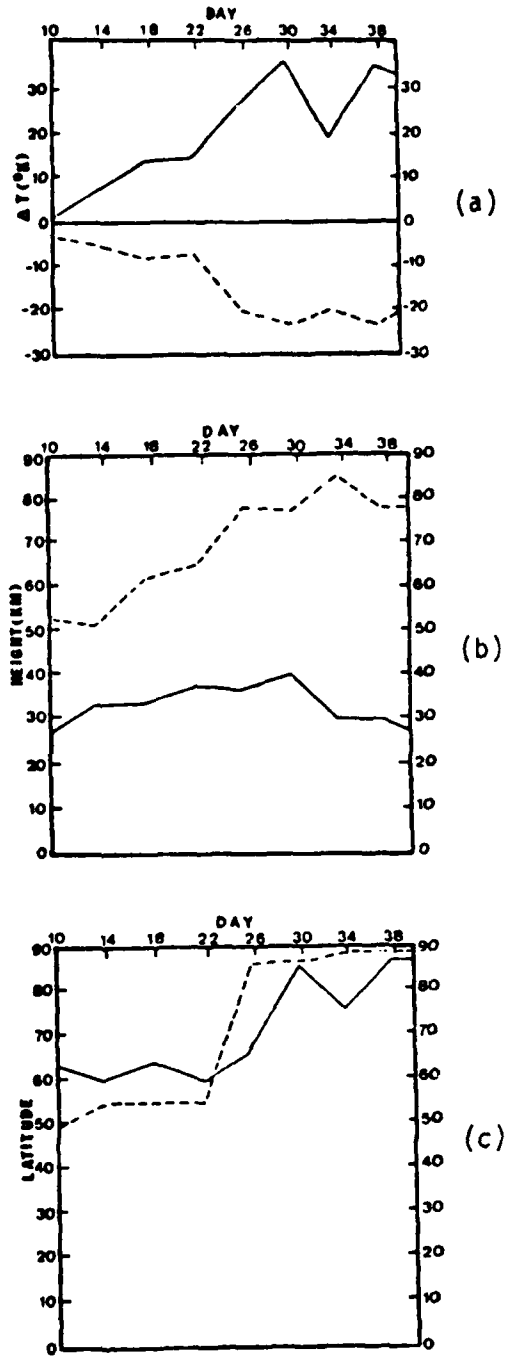

Fig. 17. Same as Fig. 16 except for case 2.

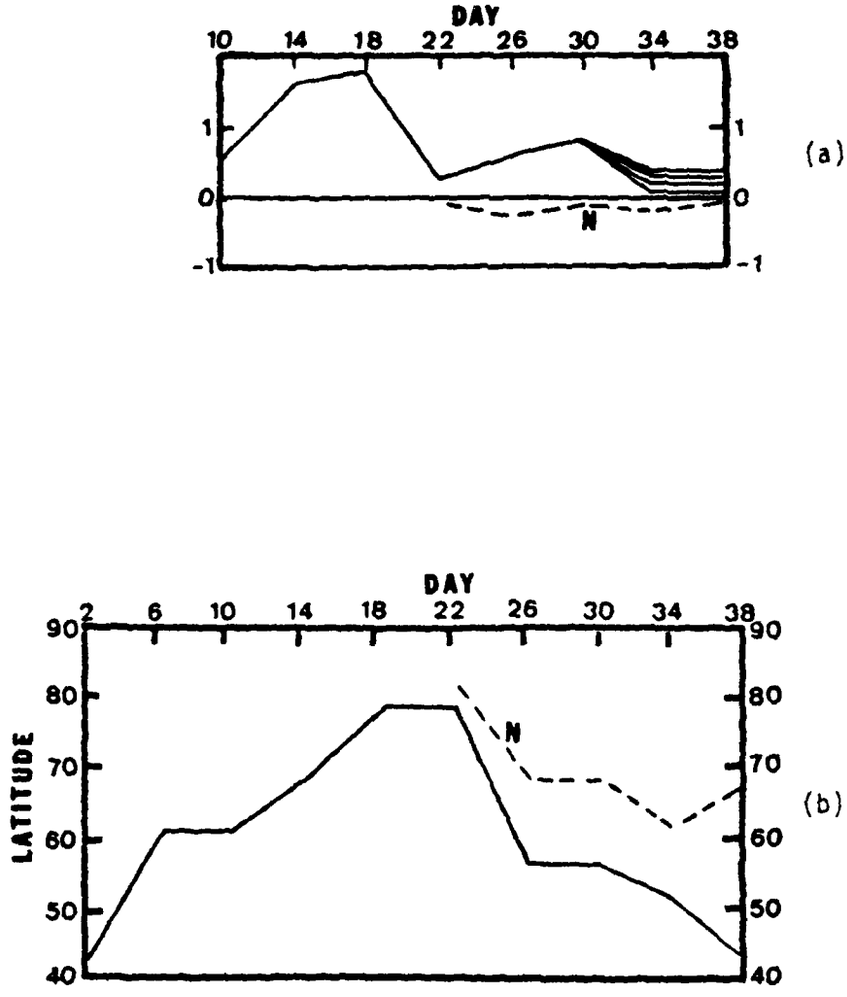

Fig. 18. Time charts of the zonal mean vertical flux of geopotential maxima for case 1 depicting (a) evolution of maxima ($\times 10^2$ m^3 s^{-3}); and (b) latitude location of the maxima.

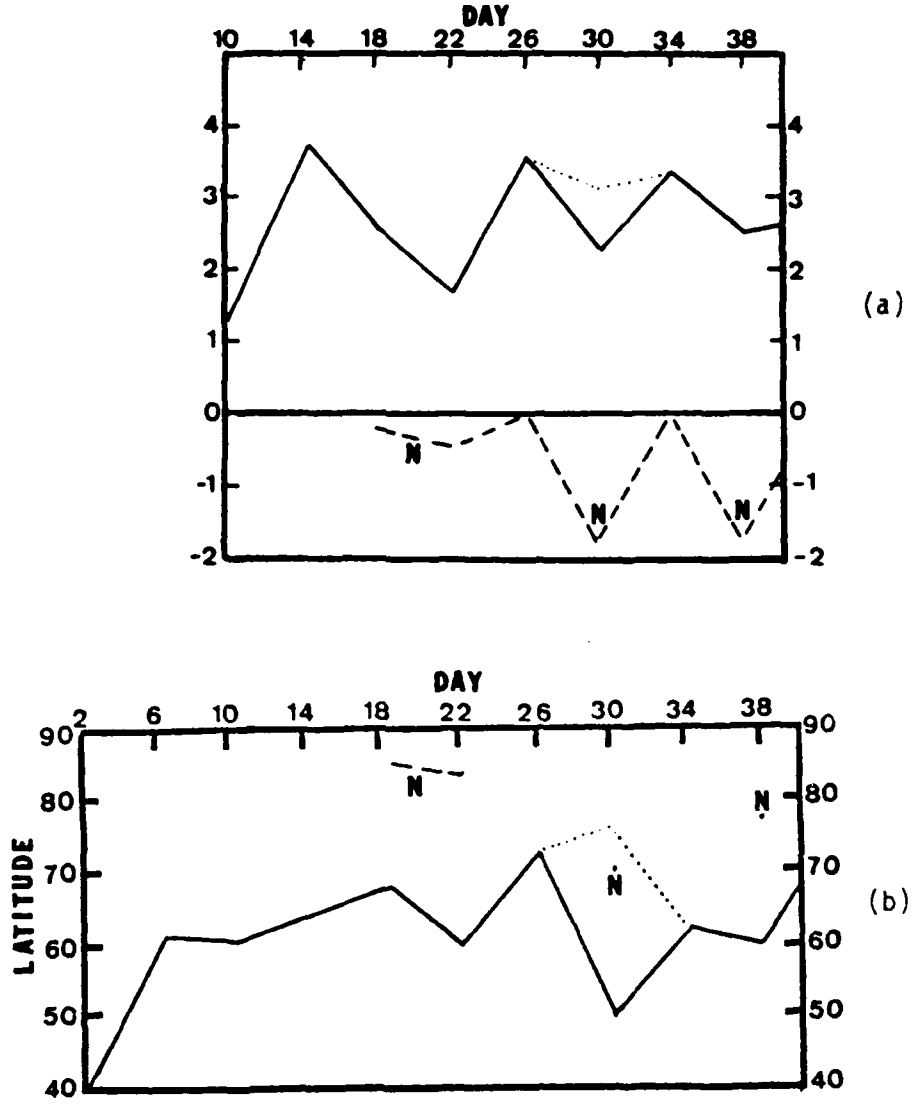

Fig. 19. Same as Fig. 18 except for case 2.

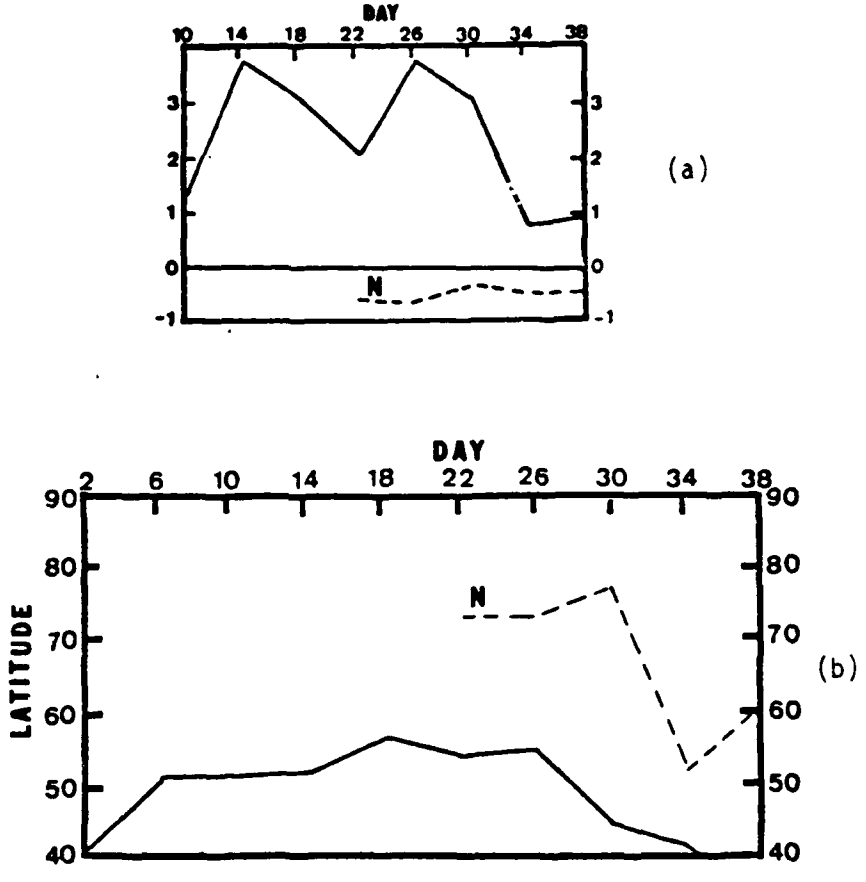

Fig. 20. Time charts of the zonal mean meridional flux of zonal momentum for case 1 depicting (a) evolution of maxima ($\times 10^2$ m^2 s^{-2}); and (b) latitude location of the maxima.

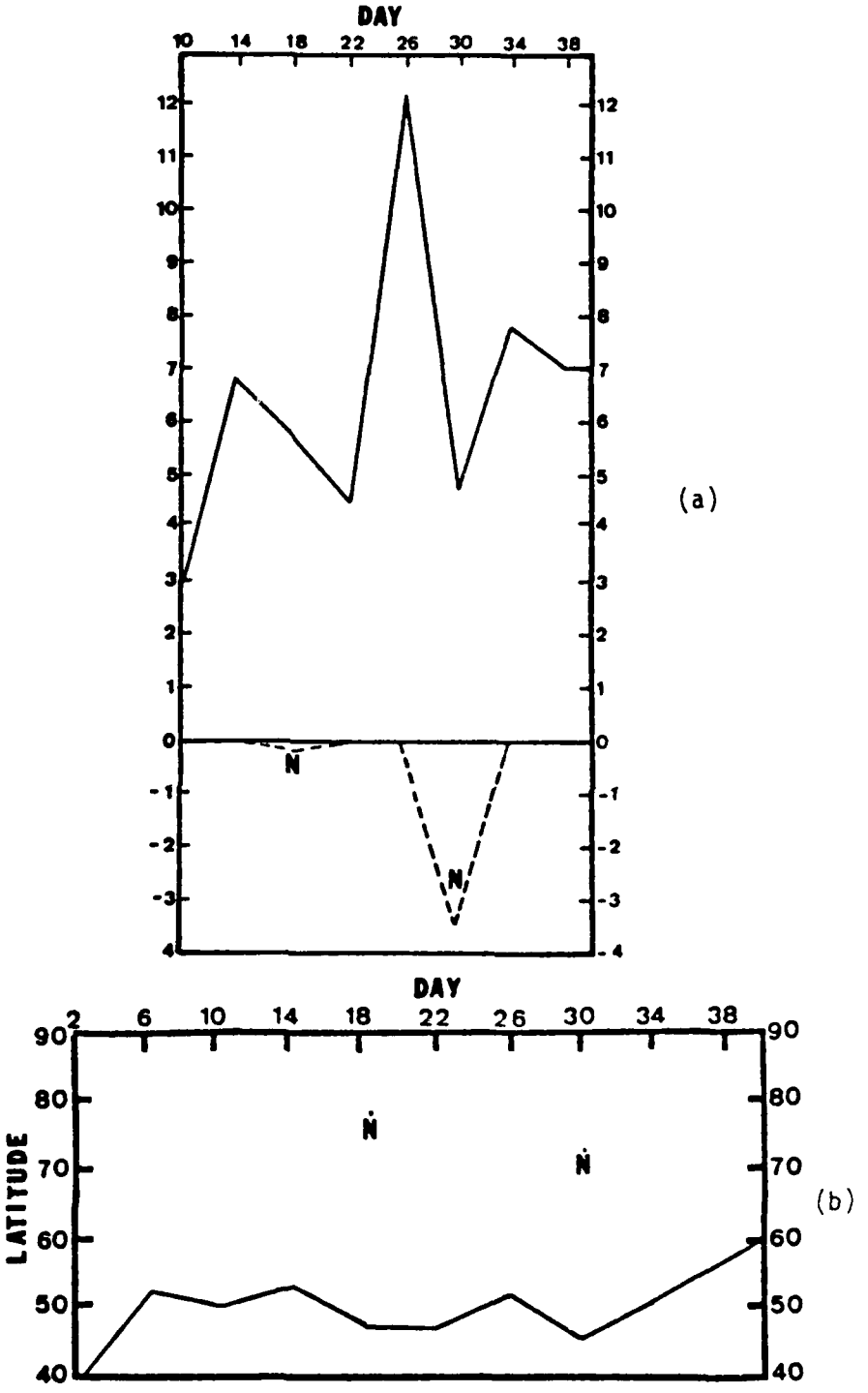

Fig. 21. Same as Fig. 20 except for case 2.

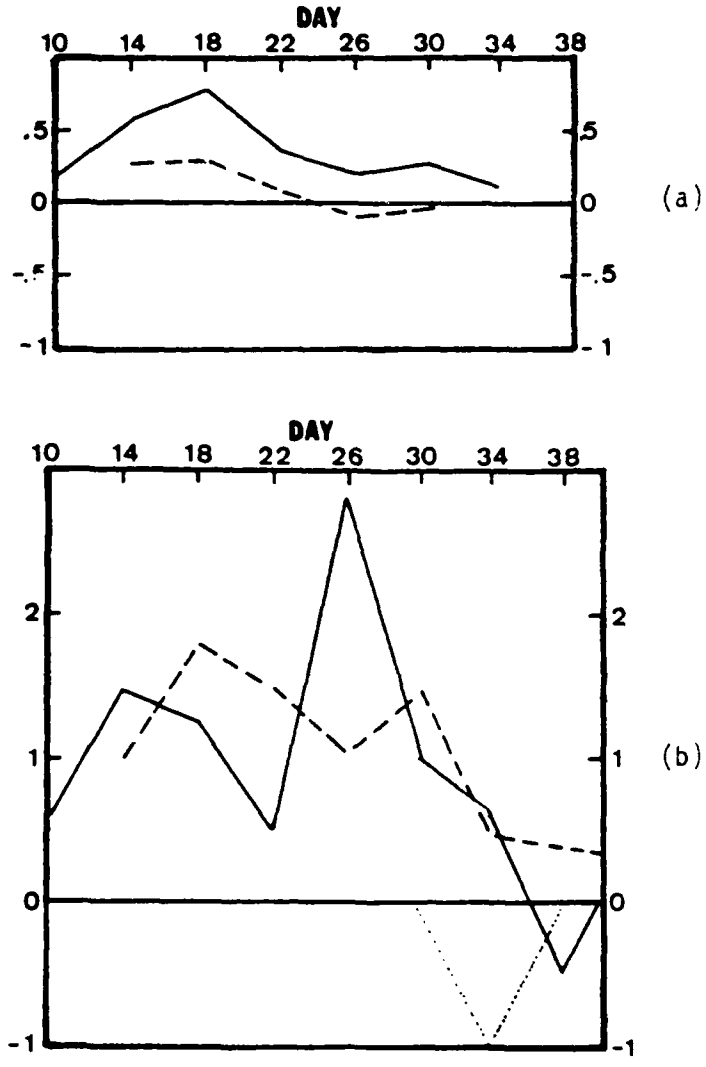

Fig. 22. Magnitude-time charts of the zonal mean of the vertical flux of zonal momentum maxima (m^2 s^{-2}) for (a) case 1 where solid line is in the upper stratosphere from 60°N - 80°N, dashed line is in low mesosphere from 37°N - 47°N; and (b) case 2 where solid line is in the upper stratopause-lower mesopause from 65°N - 83°N, dashed line is in the lower mesosphere from 44°N - 65°N dotted line is at 48°N and 70 Km.

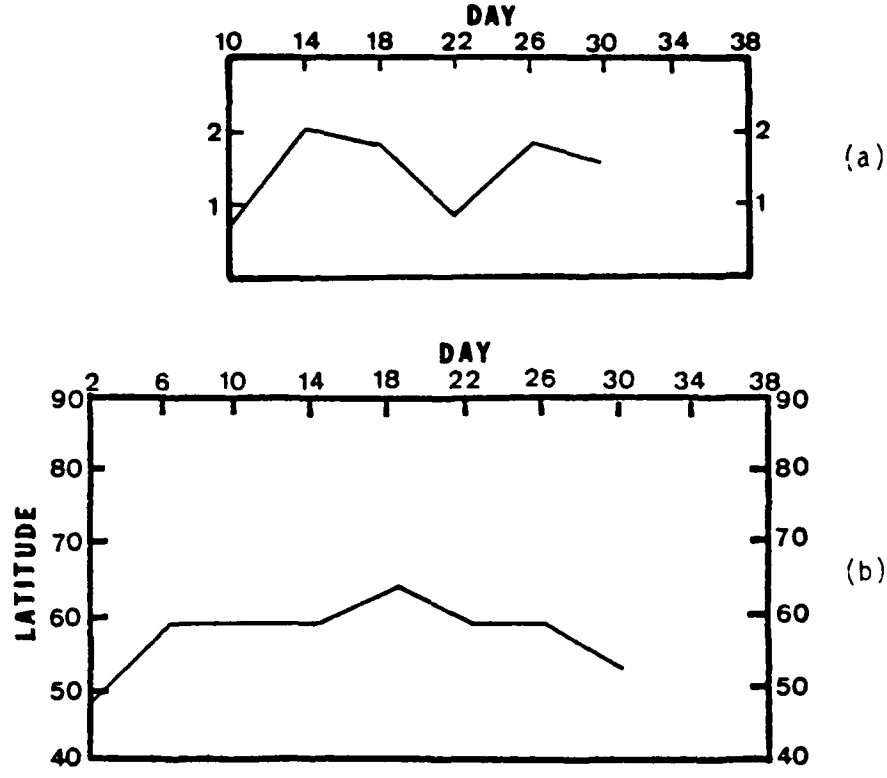

Fig. 23. Time charts of the zonal mean meridional flux of sensible heat for case 1 depicting (a) evolution of maxima (x 10^2 m s^{-1} °K); and (b) latitude location of the maxima.

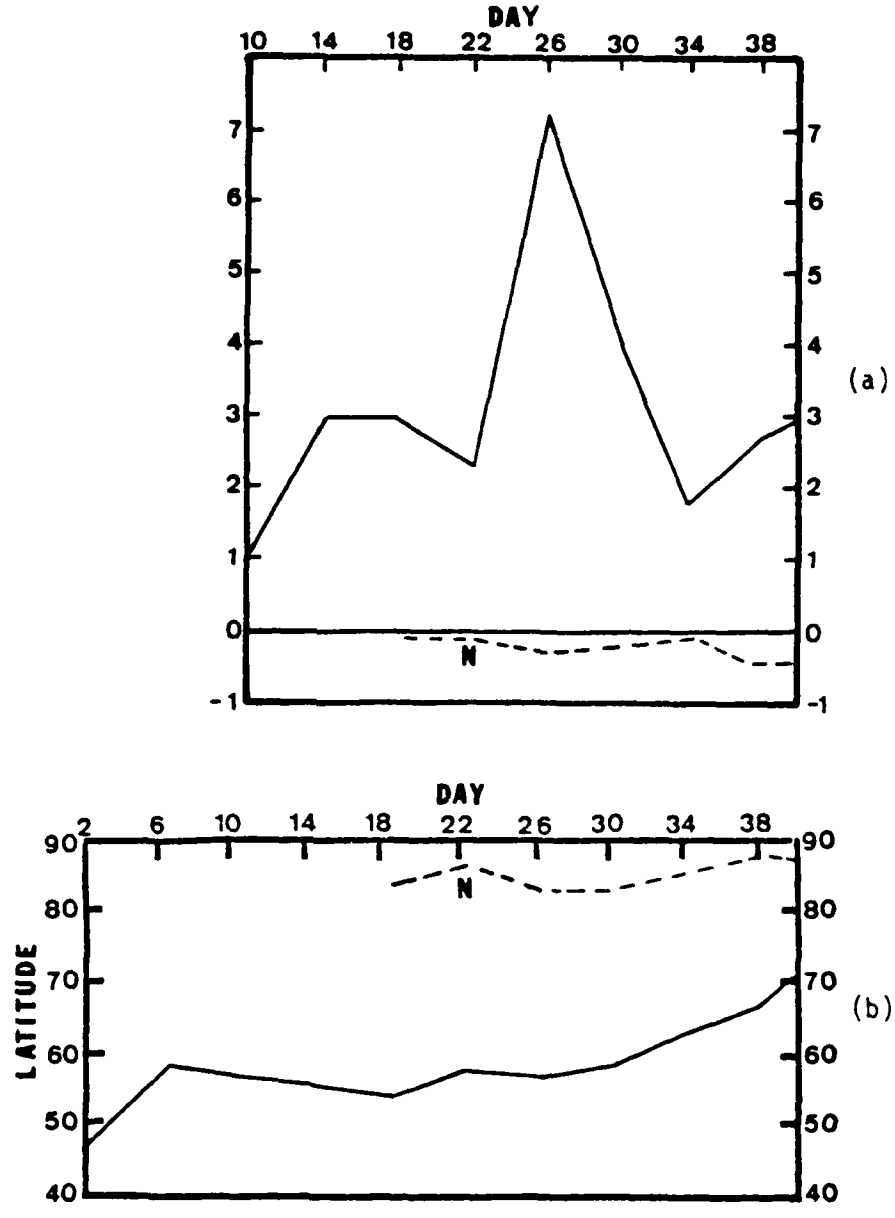

Fig. 24. Same as Fig. 23 except for case 2.

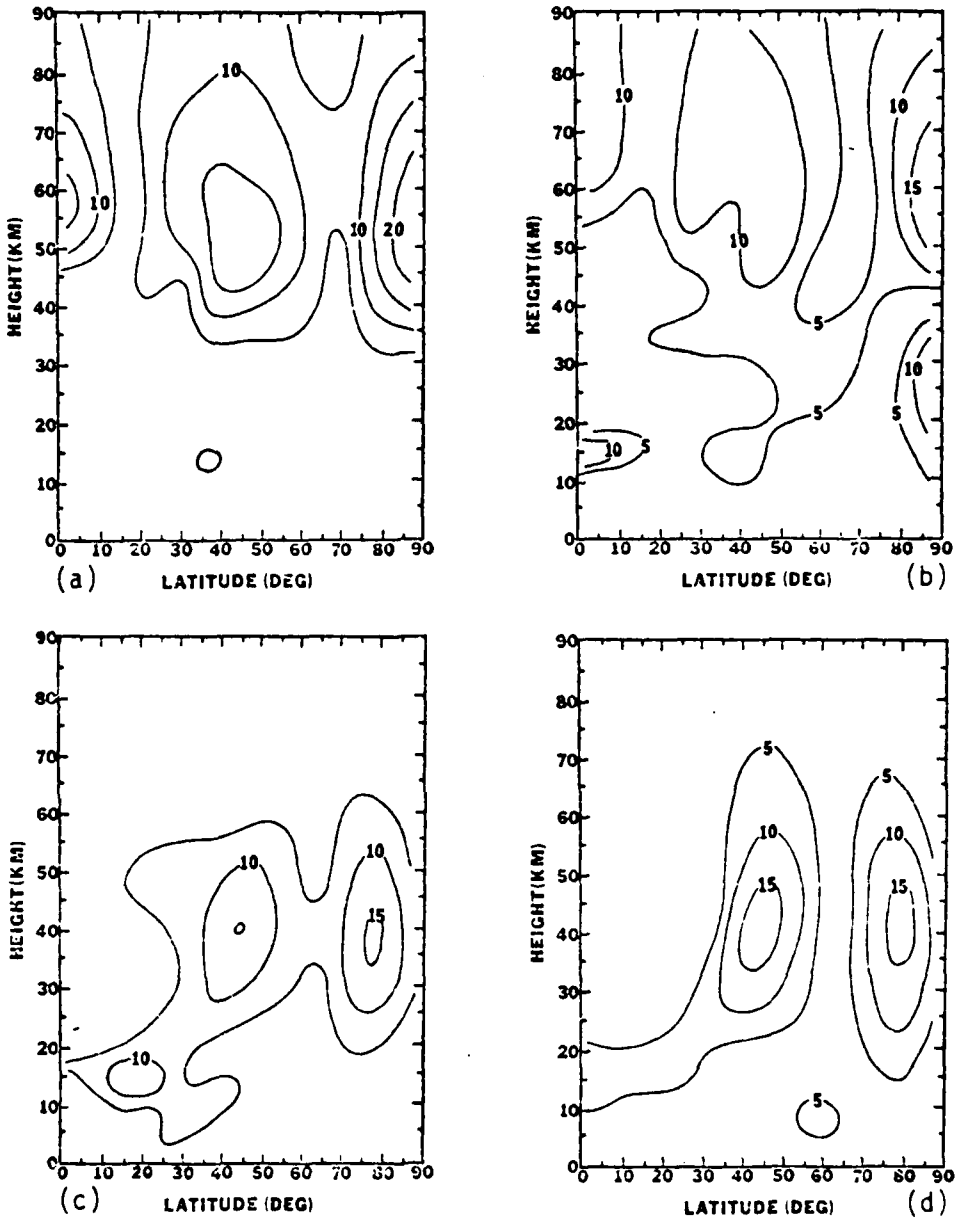

Fig. 25. Latitude-height sections of $A_u(k)$ (m s^{-1}) for case 1 (a) day 18, wave 1; (b) day 24, wave 1; (c) day 18, wave 2; and (d) day 24, wave 2.

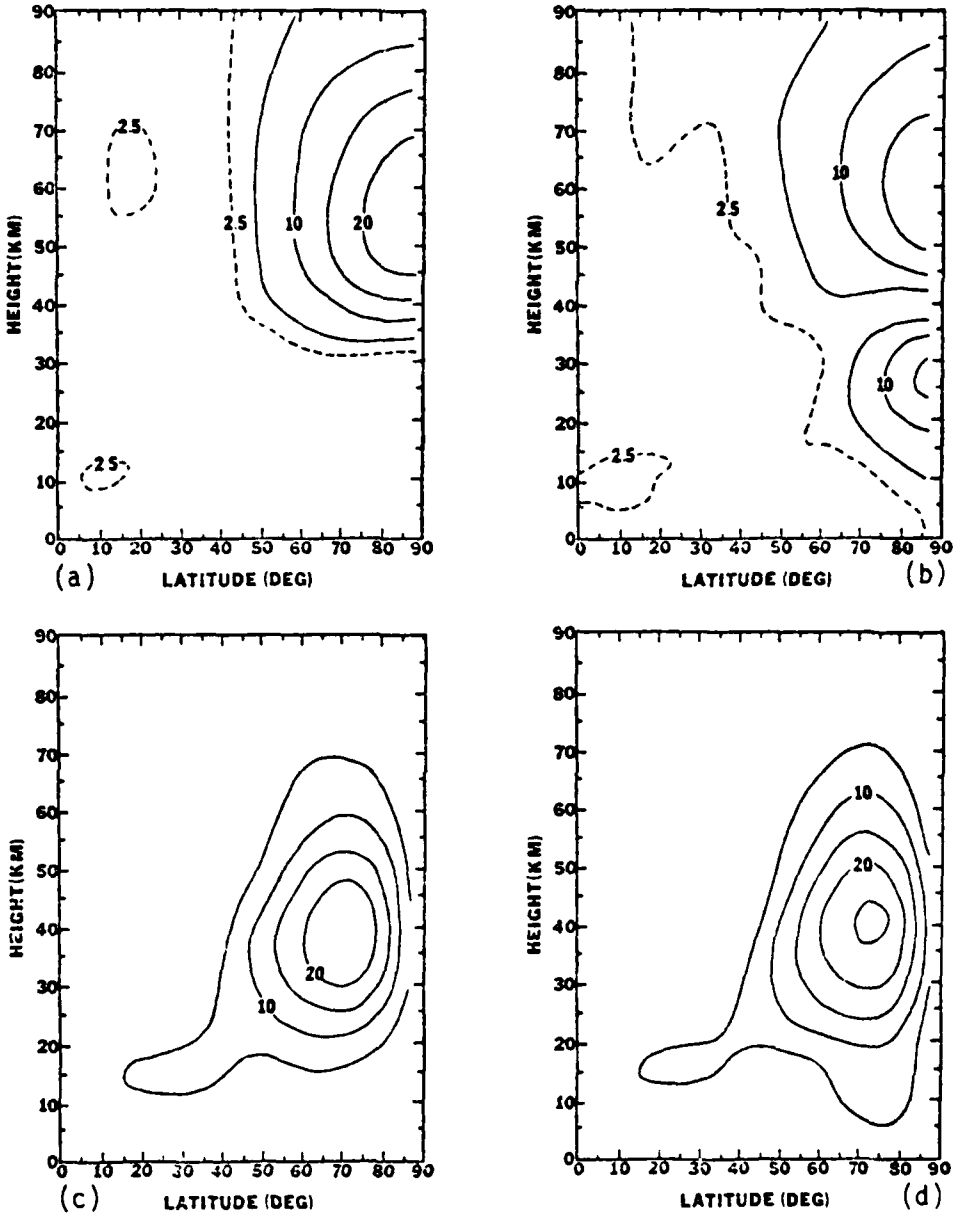

Fig. 26. Latitude-height sections of $A_v(k)$ (m s^{-1}) (a) day 18, wave 1; (b) day 24, wave 1; (c) day 18, wave 2; and (d) day 24, wave 2. Units are m s^{-1}.

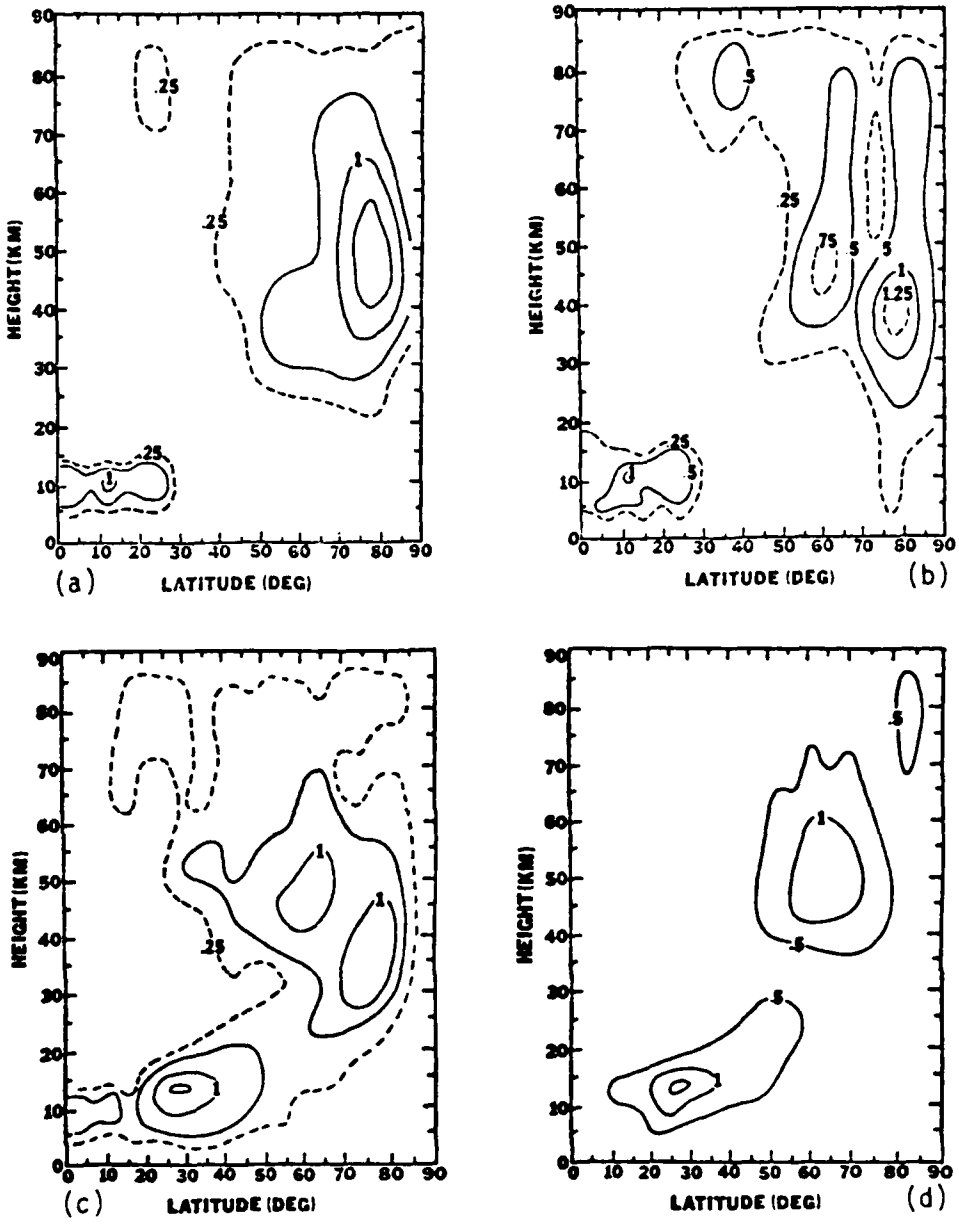

Fig. 27. Latitude-height sections of $A_w(k)$ (x 10^{-2} m s^{-1}) for case 1 (a) day 18, wave 1; (b) day 24, wave 1; (c) day 18, wave 2; and (d) day 24, wave 2.

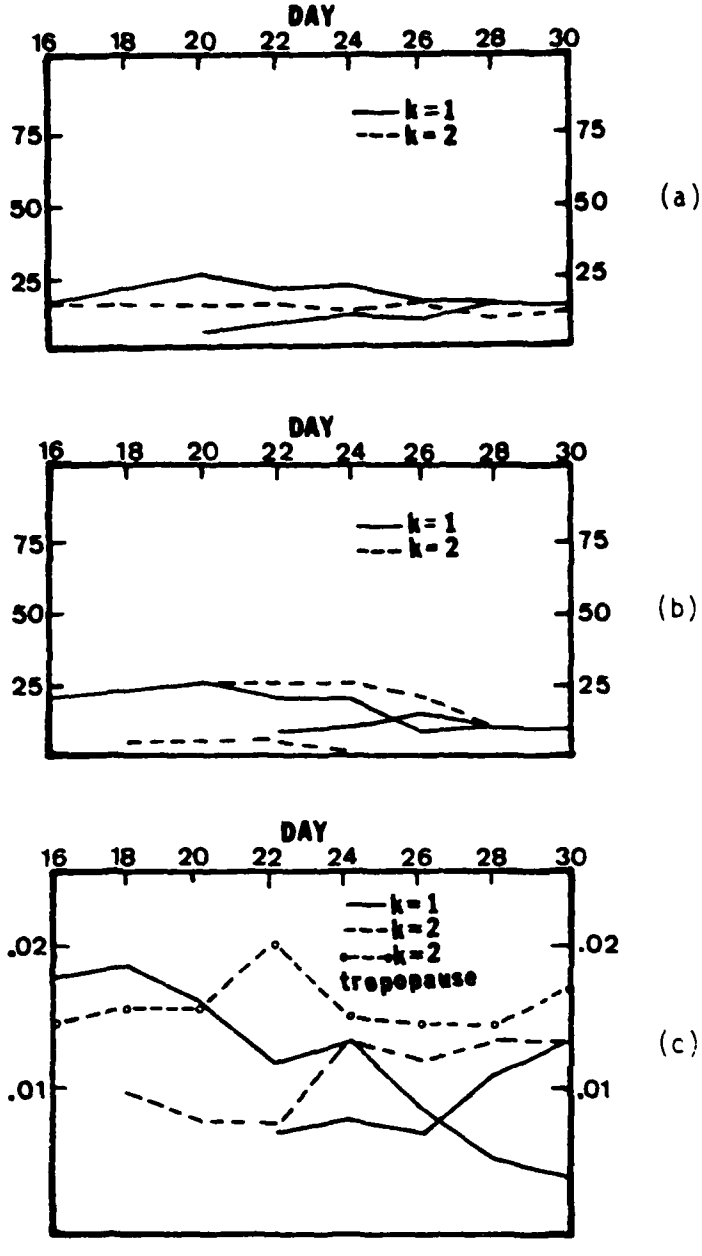

Fig. 28. Case 1 magnitude-time sections of maxima (a) $A_u(k)$; (b) $A_v(k)$; and (c) $A_w(k)$. Units are m s^{-1}.

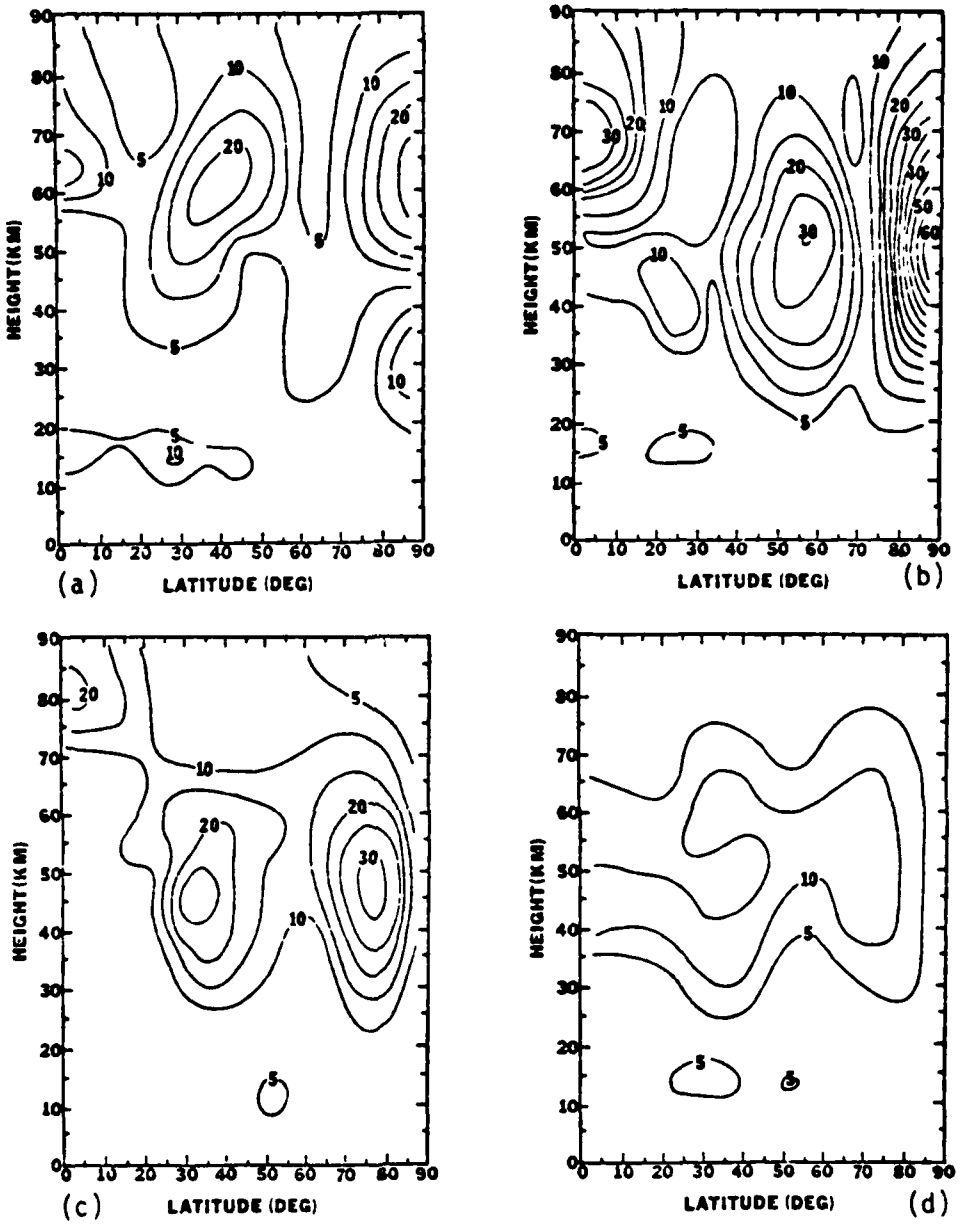

Fig. 29. Latitude-height sections of $A_u(k)$ for case 2 (a) day 26, wave 1; (b) day 30, wave 1; (c) day 26, wave 2; and (d) day 30, wave 2. Units are m s^{-1}.

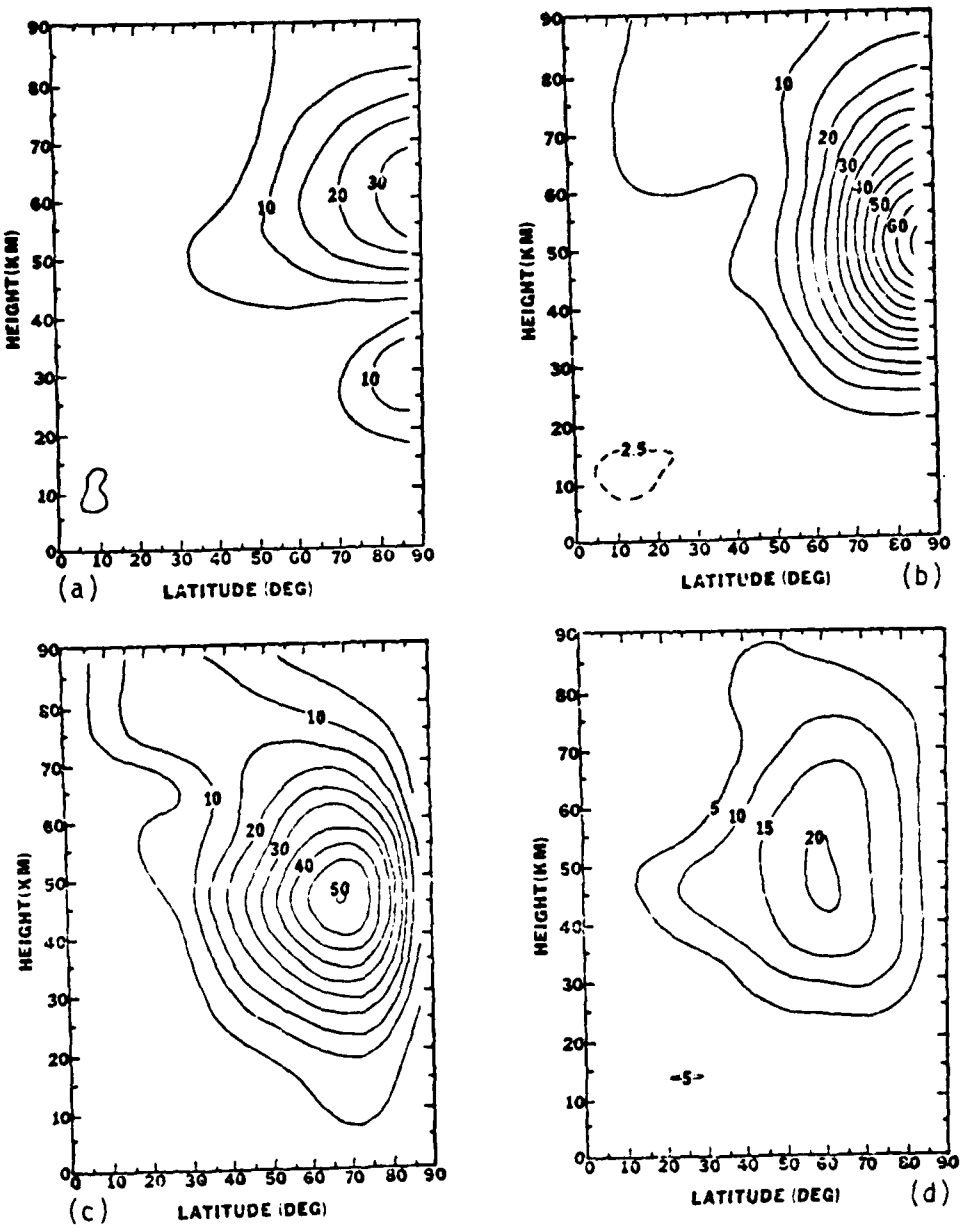

Fig. 30. Latitude-height sections of $A_v(k)$ for case 2 (a) day 26, wave 1; (b) day 30, wave 1; (c) day 26, wave 2; (d) day 30, wave 2. Units are m s^{-1}.

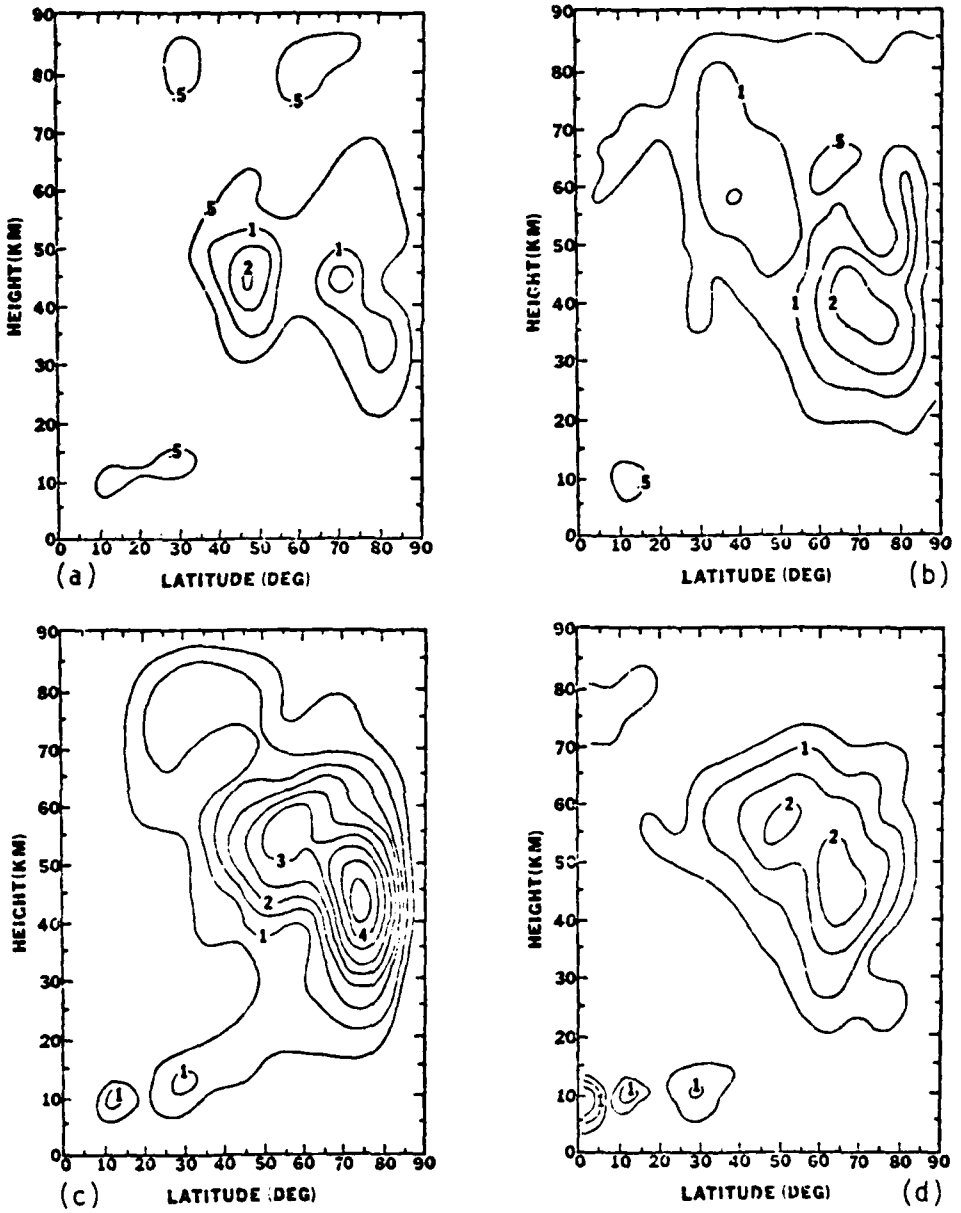

Fig. 31. Latitude-height sections of $A_w(k)$ (x 10^{-2} m s^{-1}) for case 2 (a) day 26, wave 1; (b) day 30, wave 1; (c) day 26, wave 2; and (d) day 30, wave 2.

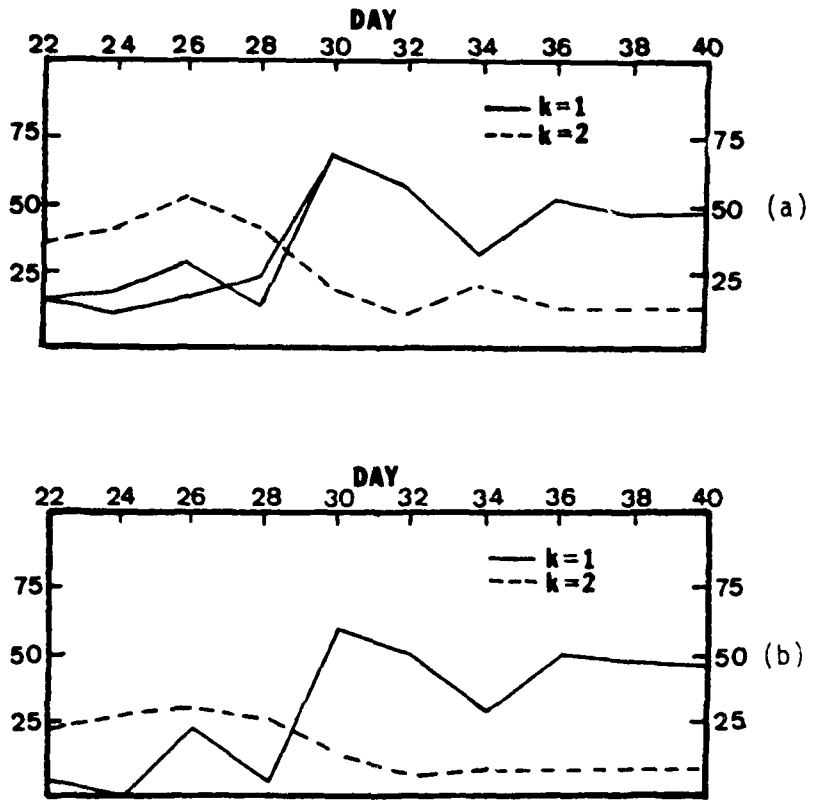

Fig. 32. Magnitude-time charts of spectral components for case 2 (m s^{-1}) for (a) $A_u(k)$; and (b) $A_v(k)$.

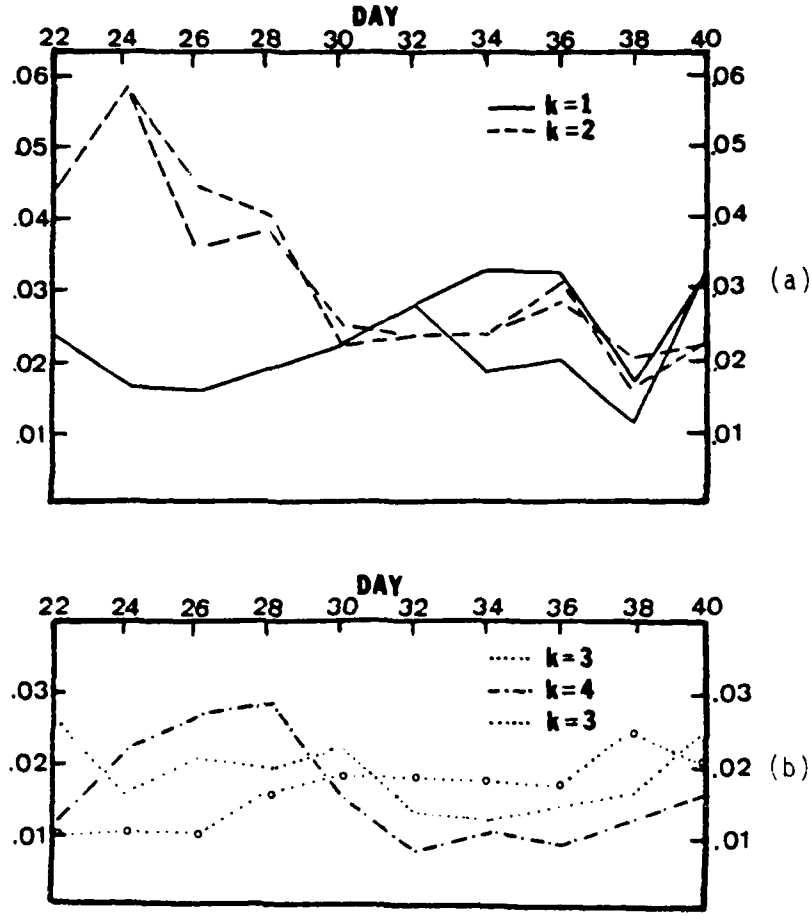

Fig. 33. Magnitude-time charts of spectral components for case 2 (m s^{-1}) for (a) A_w(1 and 2); and (b) A_w(3 and 4).

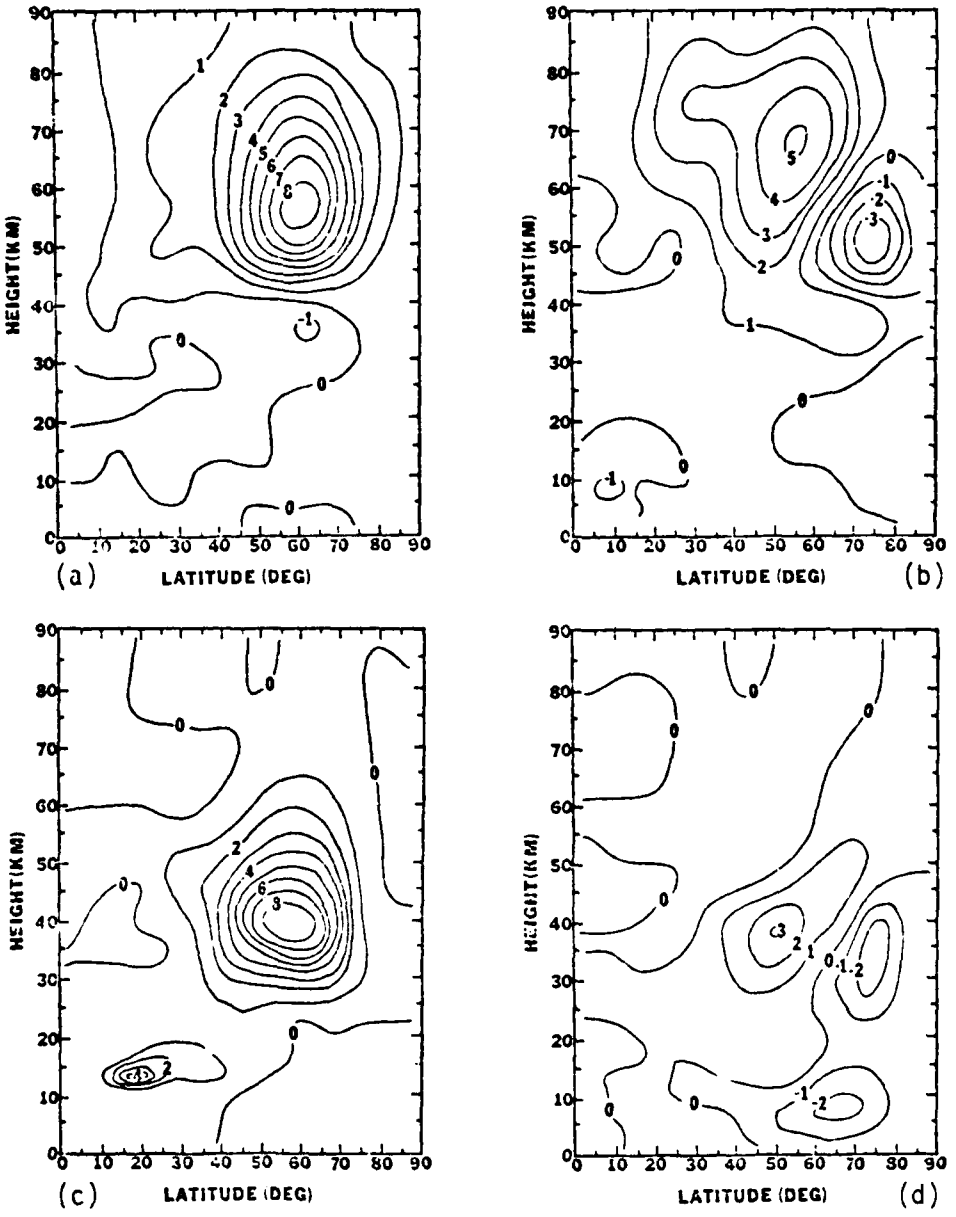

Fig. 34. Latitude-height sections of $C_{uv}(k)$ (x 10 m^2 s^{-2}) for case 1 (a) day 18, wave 1; (b) day 24, wave 1; (c) day 18, wave 2; and (d) day 24 wave 2.

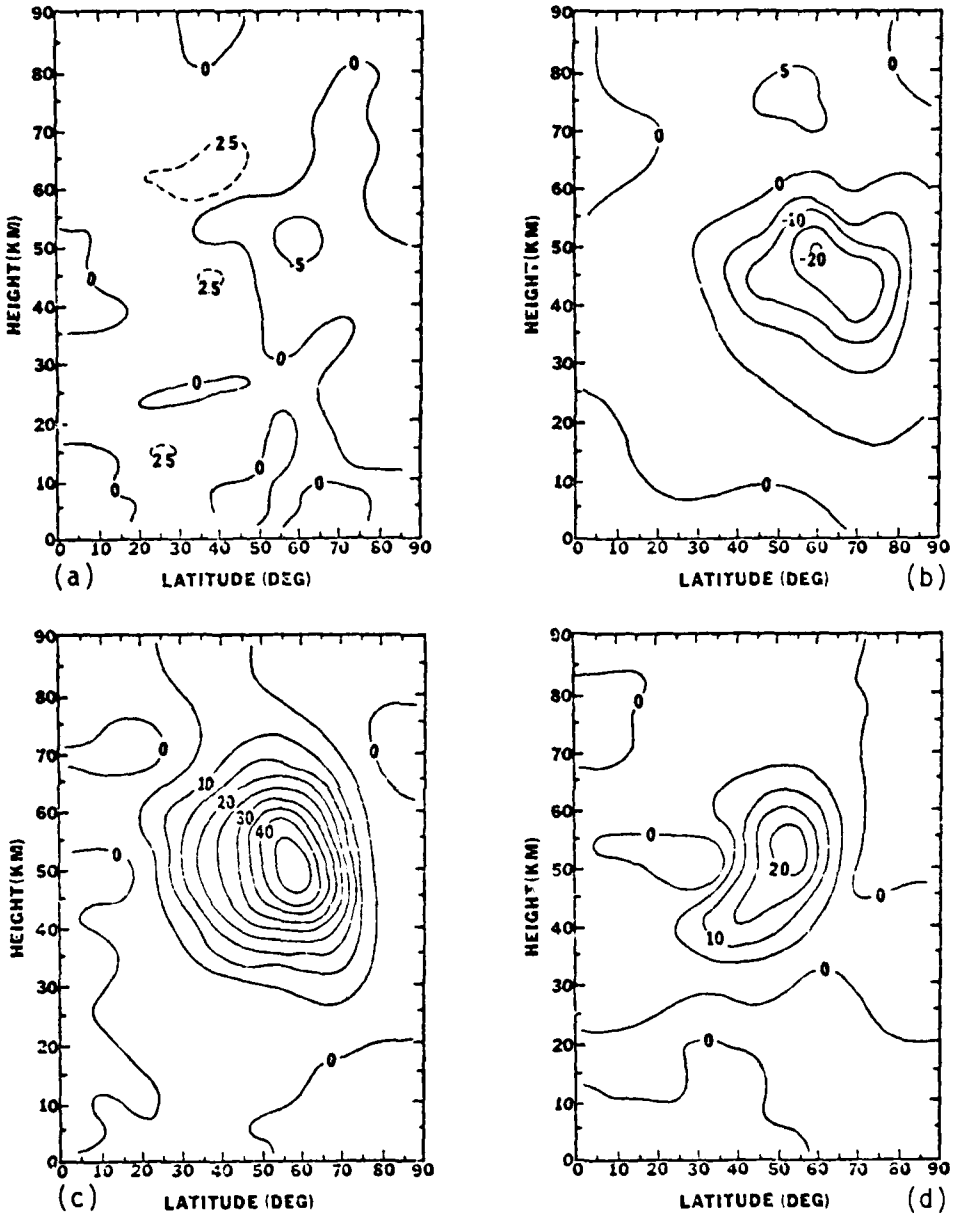

Fig. 35. Latitude-height sections of $C_{uv}(k)$ (x 10 m^2 s^{-2}) for case 2 (a) day 26, wave 1; (b) day 30, wave 1; (c) day 26, wave 2; and (d) day 30, wave 2.

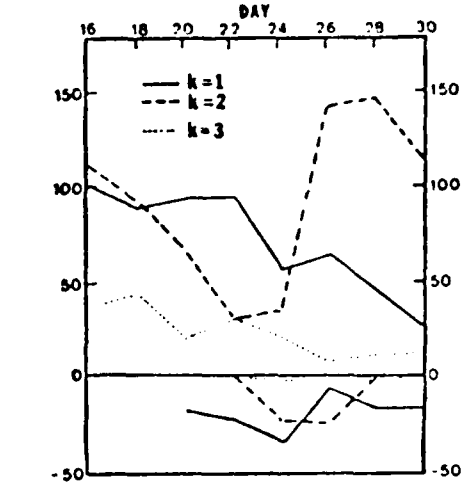

(a)

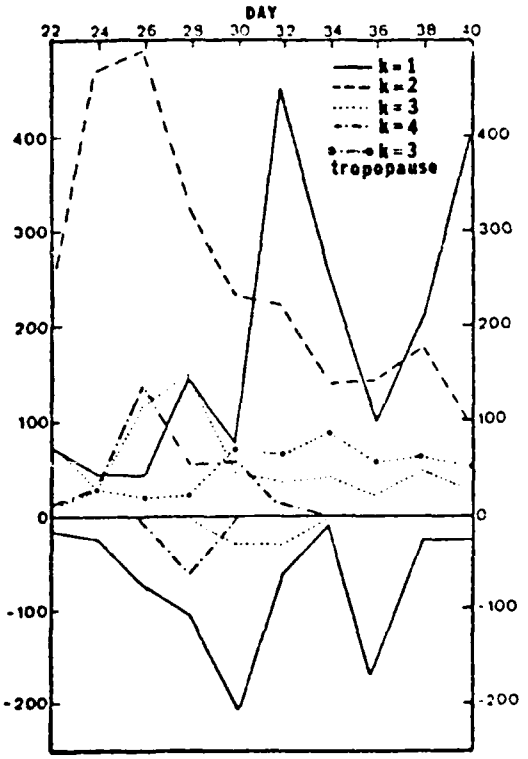

(b)

Fig. 36. Magnitude-time charts of $C_{uv}(k)$ (m^2 s^{-2} ...
(b) case 2.

AD-A106 371 AIR FORCE INST OF TECH WRIGHT-PATTERSON AFB OH F/G 4/1
COMPARISON OF THE DYNAMIC PROCESSES DURING MAJOR AND MINOR STRA--ETC(U)
JUN 81 J H DAVENPORT
UNCLASSIFIED AFIT-CI-81-29T NL

END
DATE FILMED
11-81
DTIC

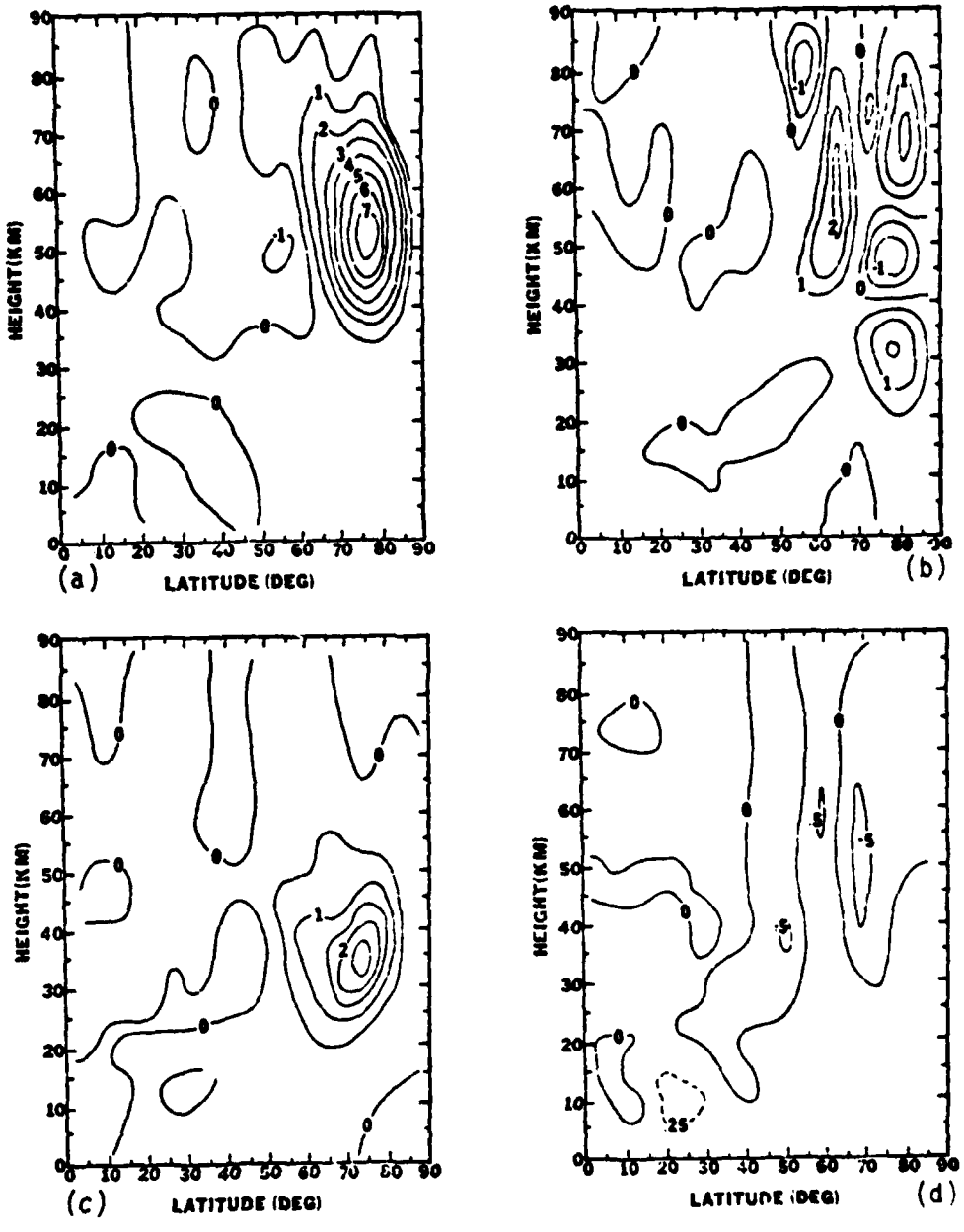

Fig. 37. Latitude-height sections of $C_{wg}(k)$ (x 10 m^3 s^{-3}) for case 1 (a) day 18, wave 1; (b) day 24, wave 1; (c) day 18, wave 2; and (d) day 24, wave 2.

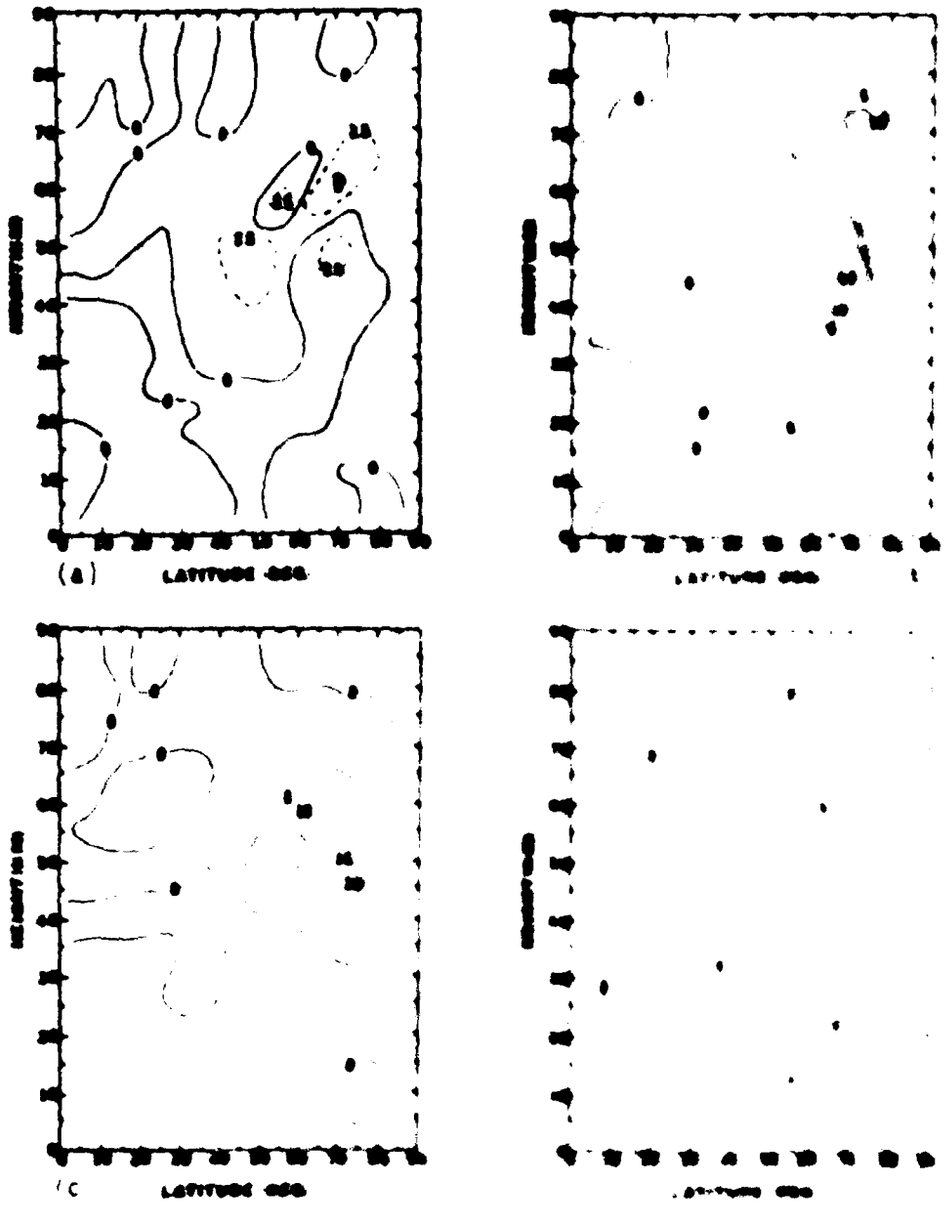

Fig. 36. Latitude-height sections of [illegible] case 2 (a) day 26, wave [illegible] day 30 wave [illegible] day 26, wave 2, and (d) day 30 wave [illegible]

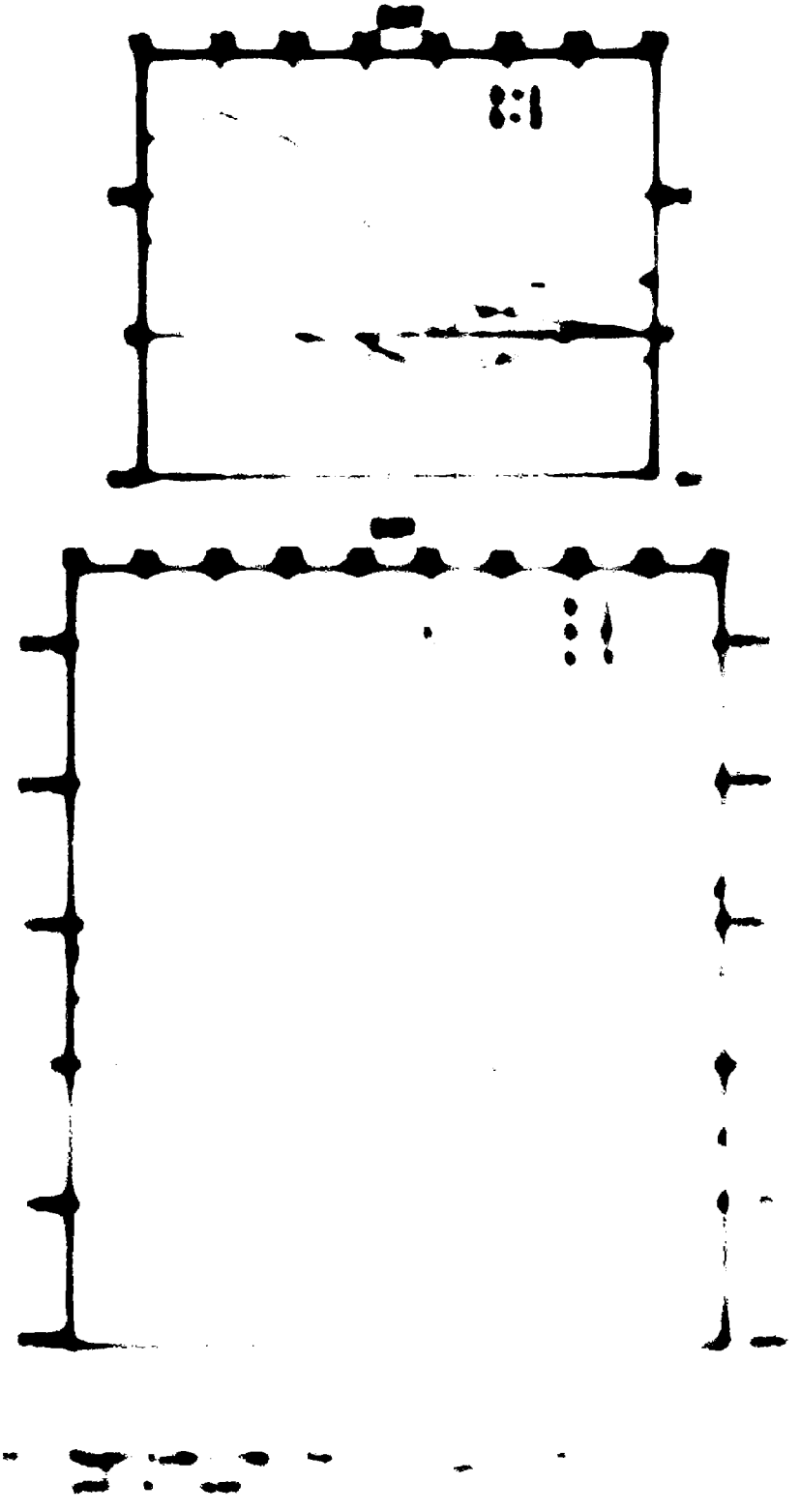

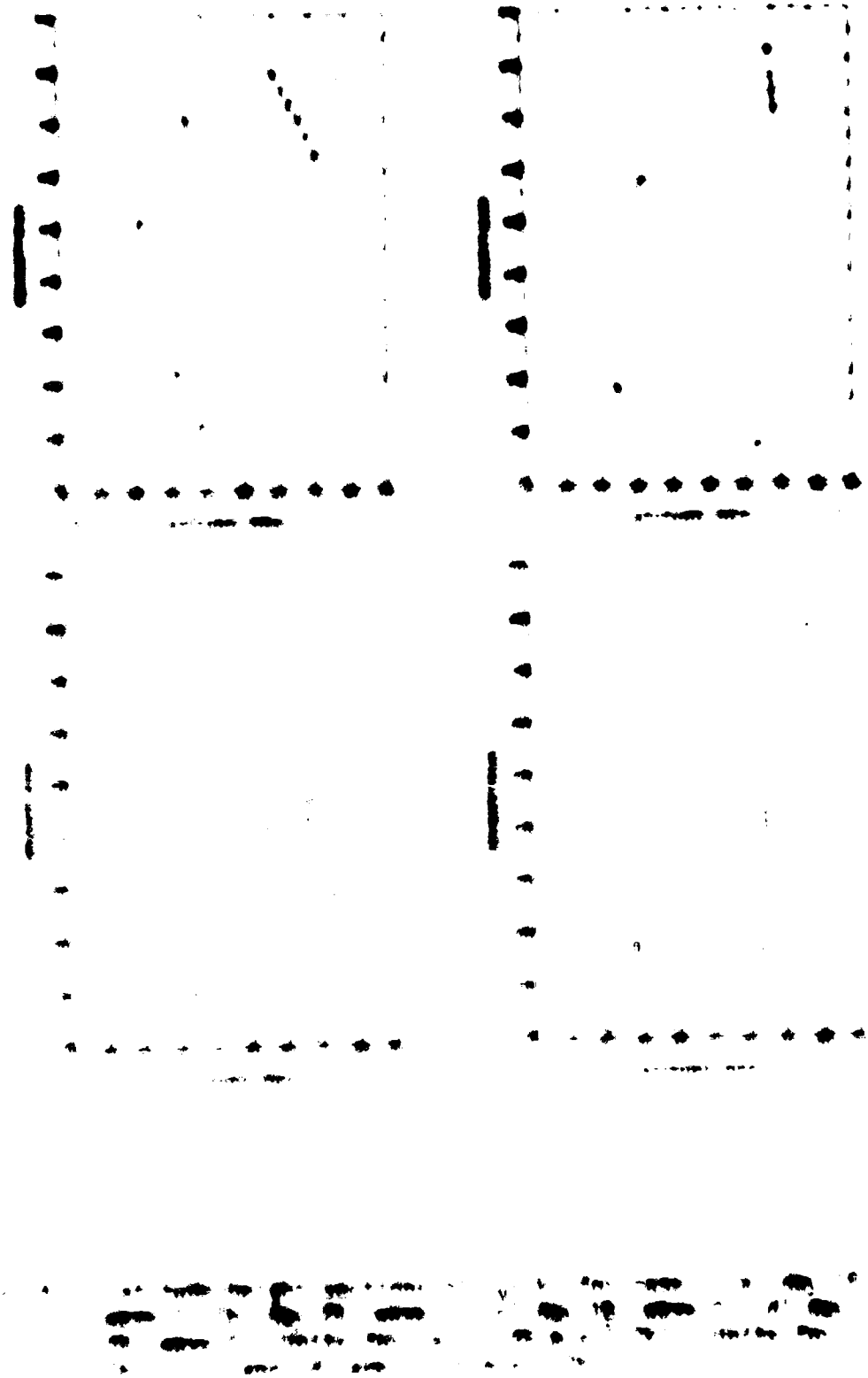

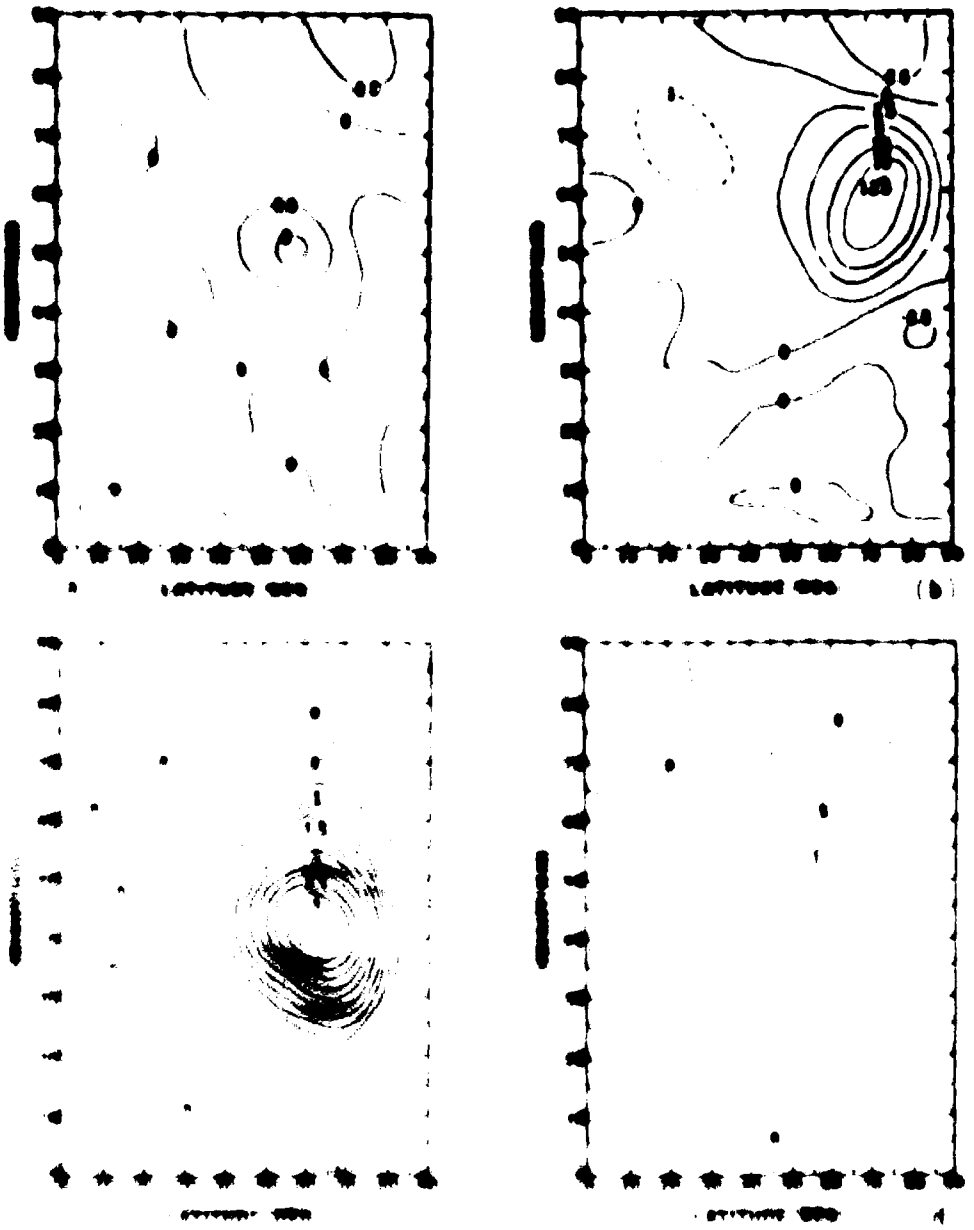

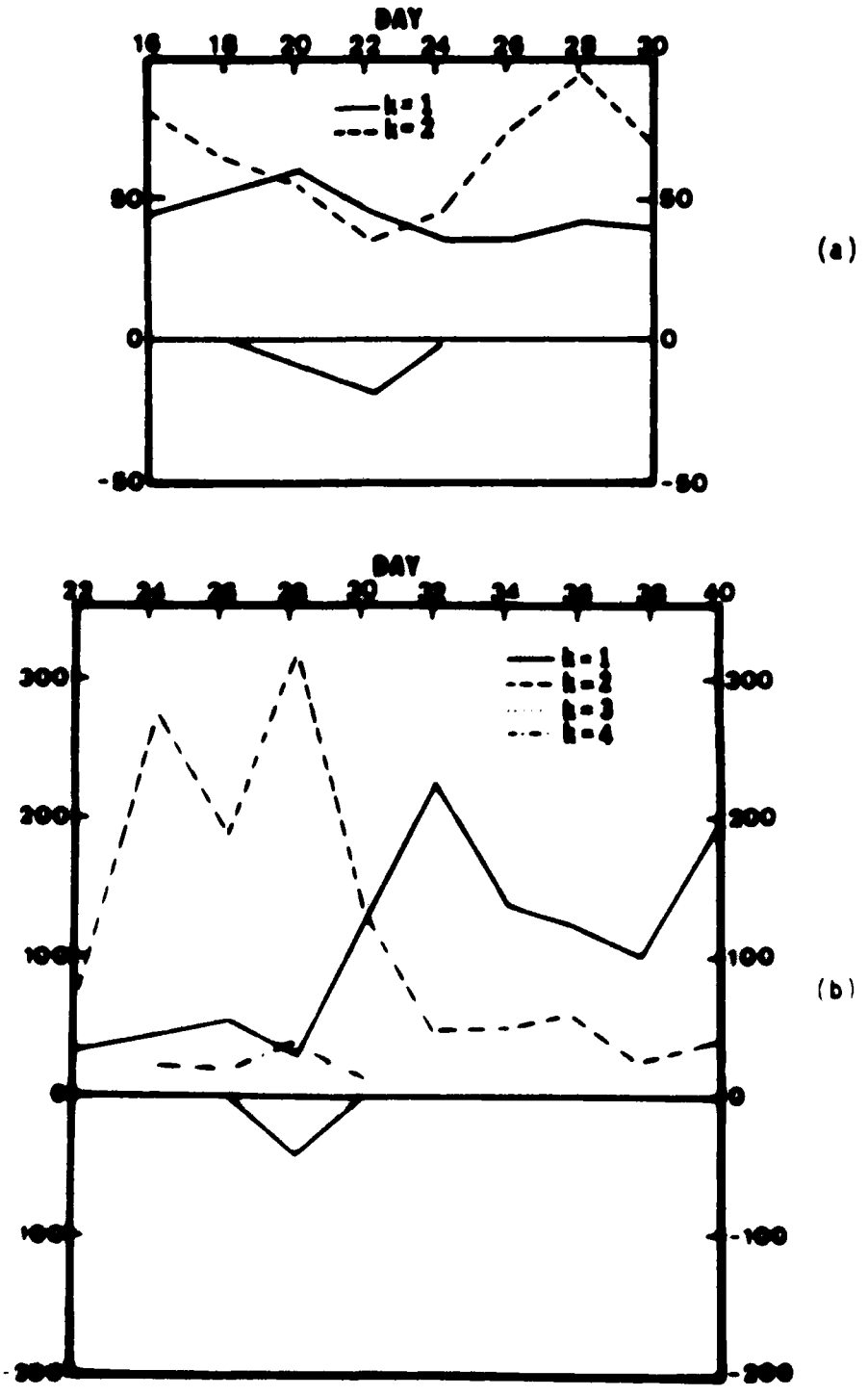

Fig. 17 Height-time charts of $\overline{v'T'}(k)$ (m s^{-1} °K) for (a) case 1 and (b) [illegible]

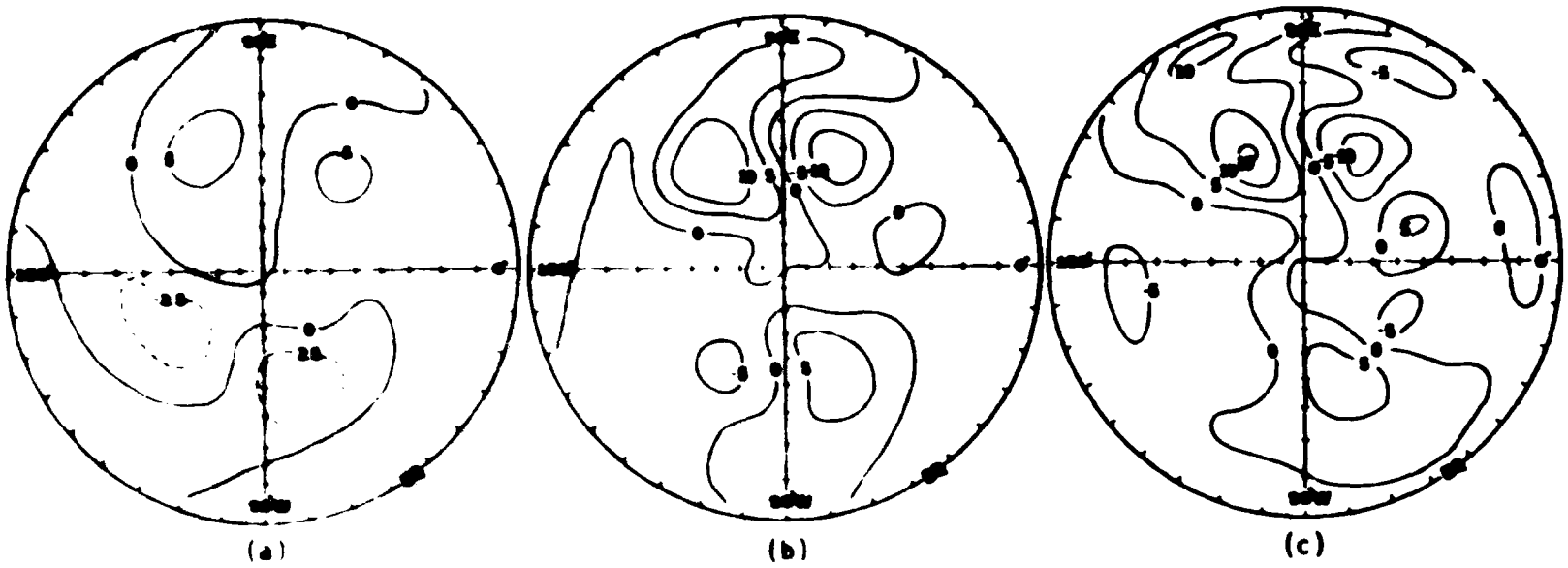

Fig. 43. Polar stereographic projections of meridional velocity deviations (m s^{-1}) for case 1 at 7.5 km on (a) day 14, (b) day 18, and (c) day 30.

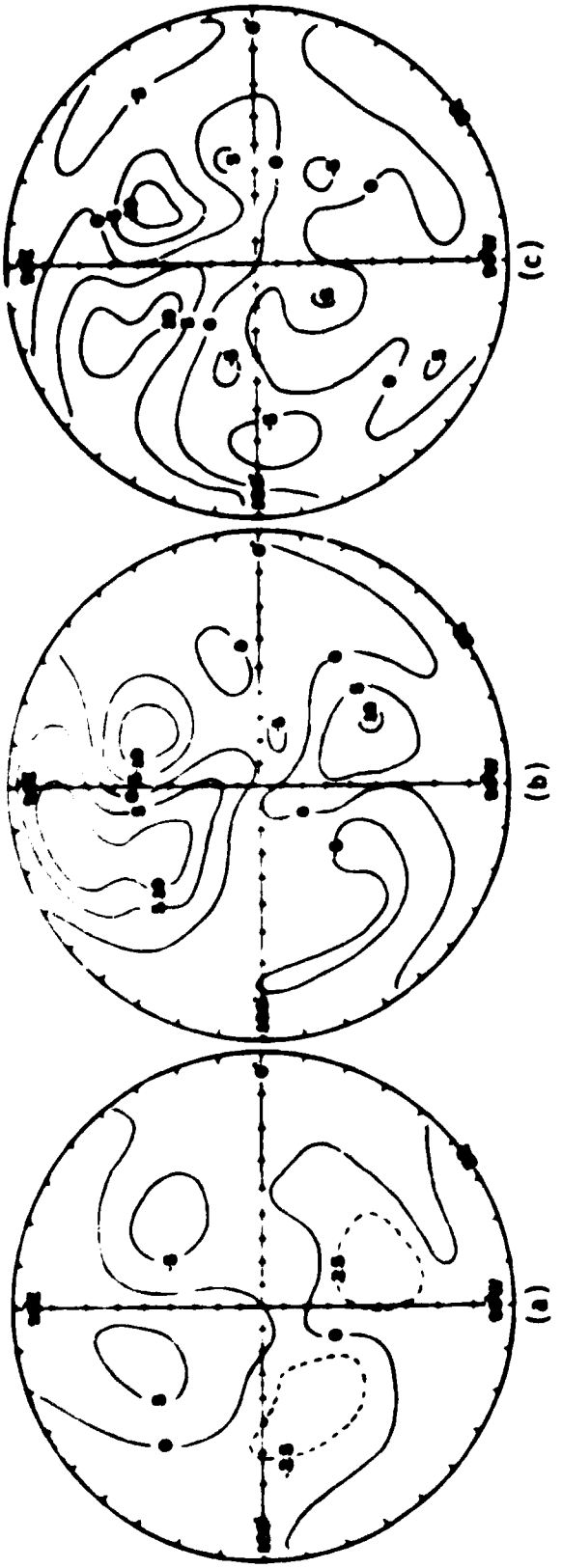

Fig. 45. Polar stereographic projections of meridional velocity deviations (m s^{-1}) for case 2 at 7.5 km on (a) day 14; (b) day 18; and (c) day 30.

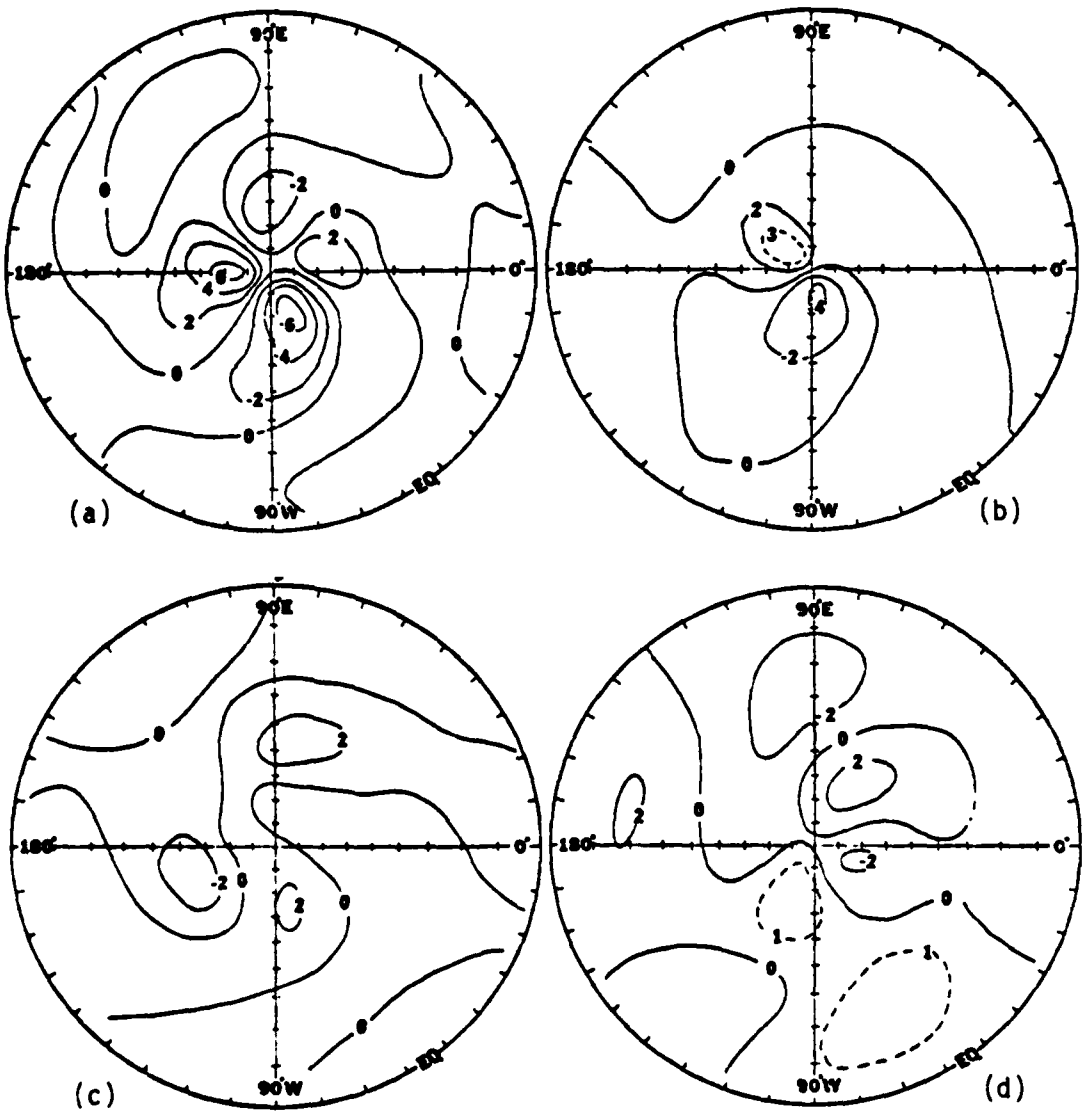

Fig. 44. Polar stereographic projections of meridional velocity deviations (x 10 m s^{-1}) for case 1 on (a) day 18, 40.5 km; (b) day 18, 67.5 km; (c) day 30, 40.5 km; and (d) day 30, 67.5 km.

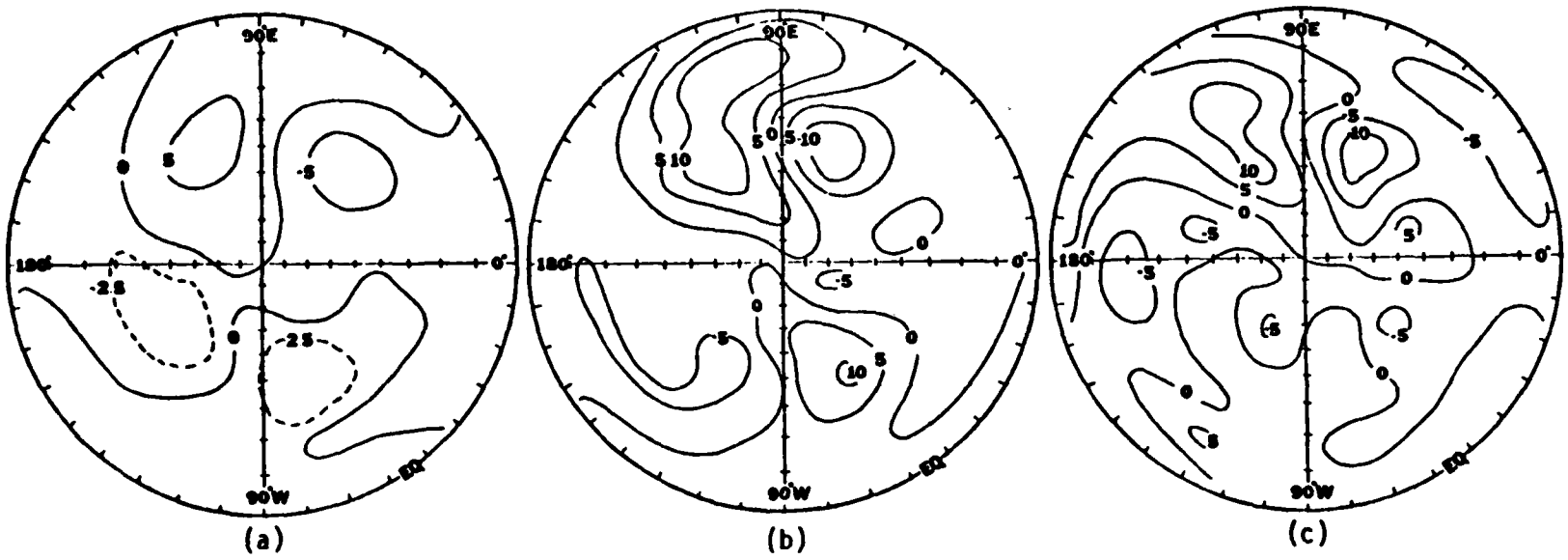

Fig. 45. Polar stereographic projections of meridional velocity deviations (m s^{-1}) for case 2 at 7.5 km on (a) day 14; (b) day 18; and (c) day 30.

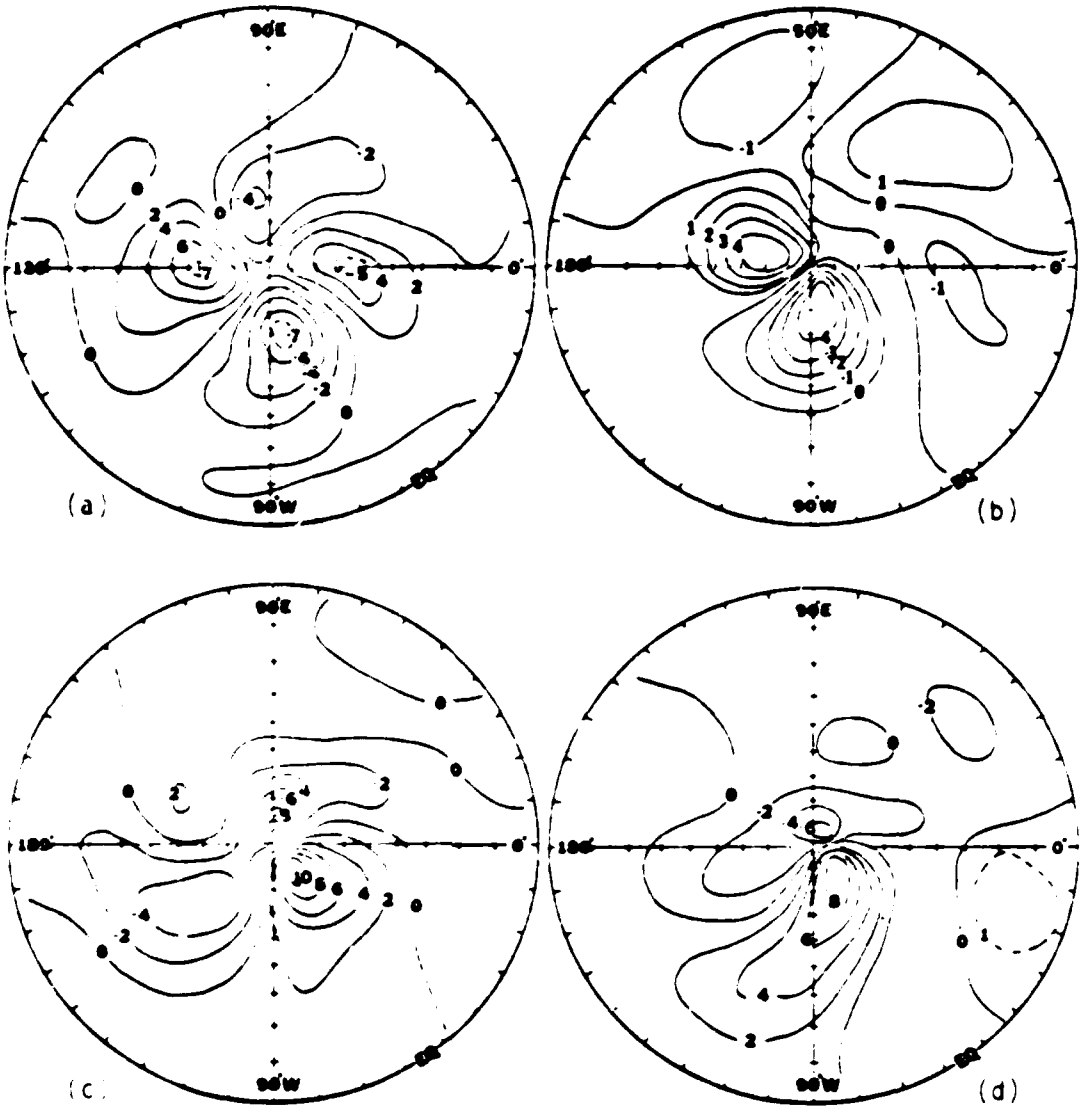

Fig. 46. Polar stereographic projections of meridional velocity deviations (x 10 m s^{-1}) for case 2 on (a) day 18, 40.5 km; (b) day 18, 67.5 km; (c) day 30, 40.5 km; and (d) day 30, 67.5 km.

REFERENCES

Bourke, W., A multi-level spectral model, 1974. I. Formulation and hemispheric integrations, Mon. Wea. Rev., 102, 687-701.

Bourke, W., B. McAvaney, K. Puri and R. Thurling, 1977. Global modeling of the atmospheric flow by spectral methods. Methods in Comp. Phys., 17, 267-334.

Charney, J.G., and P.G. Drazin, 1961: Propagation of planetary disturbances form the lower into the upper atmosphere, J. Geophys. Res., 66, 83-109.

Eliassen, A., and E. Palm, 1961: On the transfer of energy in stationary mountain waves. Geofysiskie Publikasjoner [illegible] 1-23.

Kao, S.K., 1980: Equations of kinetic and available potential energy evolution in wave number frequency space. Pure & Appl. Geophys. 118, 867-679.

_____, 1981: On the relation between the zonal mean and vertical fluxes of momentum and temperature (unpublished manuscript), University of Utah.

Koermer, J.P., 1980: Major and minor stratospheric warmings and interactions on the troposphere, Ph.D. Thesis, University of Salt Lake City, Utah.

_____ and S.K. Kao, 1980: Major and minor stratospheric warmings and their interactions on the troposphere. Pure and Appl. Geophys. 118, 428-451.

Lordi, N.J.: 1978. A primitive equation spectral model for the study of stratospheric sudden warming, Ph.D. Thesis, University of Salt Lake City, Utah.

Matsuno, T., 1971. A dynamical model of the stratospheric sudden warming, J. Atmos. Sci., 28, 1479-1494.

McInturff, R.M., 1978: Stratospheric warmings: Synoptic, dynamic and general-circulation aspects. NASA Reference Publications, 166 pp.

O'Neill, A., and B.F. Taylor, 1979: A study of the major stratospheric warming of 1976-77. Quart. J. Roy. Meteorol. Soc. 105.

Oort, A.H., and E.M. Rasmusson, 1971. Atmospheric circulation statistics. NOAA Professional Paper 5, U.S. Department of Commerce National Oceanic and Atmospheric Administration, Rockville, Maryland, 323 pp.

Puri, K., and W. Bourke, 1974. Implications of horizonal resolution in spectral model integrations, Mon. Wea. Rev., 102, 333-347.

Quizoz, R.S., 1969. The warming of the upper stratosphere in February 1966 and the associated structure of the mesosphere, Mon. Wea. Rev., 97, 541-552.

_____, et al., 1975: A comparison of observed and simulated properties of sudden stratospheric warmings, J. Atmos. Sci. 32, 1723-1736.

U.S. Standard Atmosphere, 1976. Govt. Printing Office, Washington, D.C., 227 pp.

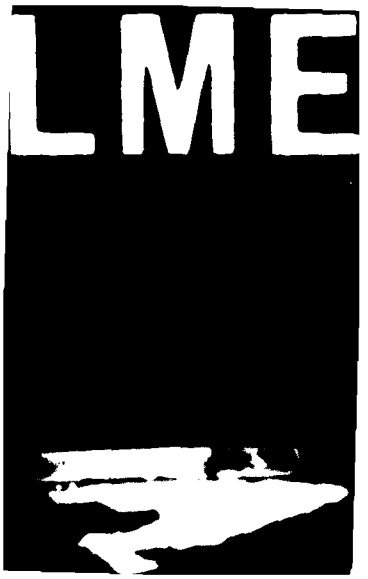
LME